NMR Characterization and Control of Noisy Quantum Systems

A thesis

Submitted in partial fulfillment of the requirements of the degree of

Doctor of Philosophy

by

Deepak Khurana

Registration ID-20132017

Department of Physics

INDIAN INSTITUTE OF SCIENCE EDUCATION AND RESEARCH

PUNE-411008, India

Certificate

Certified that the work incorporated in the thesis entitled **"NMR characterization and control of noisy quantum systems"** submitted by **Deepak Khurana** was carried out by the candidate, under my supervision. The work presented here or any part of it has not been included in any other thesis submitted previously for the award of any degree or diploma from any other university or institution.

Date: 7-Feb-2020

Dr. T.S. Mahesh
(Supervisor)

Declaration

I declare that this written submission represents my ideas in my own words and where others ideas have been included, I have adequately cited and referenced the original sources. I also declare that I have adhered to all principles of academic honesty and integrity and have not misrepresented or fabricated or falsified any idea/data/fact/source in my submission. I understand that violation of the above will be cause for disciplinary action by the Institute and can also evoke penal action from the sources which have thus not been properly cited or from whom proper permission has not been taken when needed.

Date: 7-Feb-2020

Deepak Khurana
(20132017)

Acknowledgments

Finally! Ph.D. is getting over. Of course, it's a life-changing experience because I have invested my last six years on it. Now I would like to take the opportunity to thank all the individuals whose continuous support has helped me get over the line.

Foremost, I would like to thank my supervisor, Dr. T. S. Mahesh, for his constant encouragement, guidance, and motivation throughout my Ph.D. It was a very creative and formative experience working in his group. I genuinely appreciate his thorough understanding of NMR as well as quantum information concepts, and learning from him was a lot of fun. His calmness, while explaining concepts and handling blunders of Ph.D. students, is something I would like to adopt. In a nutshell, best supervisor ever!

I thank my Research Advisory Committee (RAC) members, Dr. M. S. Santhanam, and Dr. Sourabh Dube, for yearly evaluation to keep my Ph.D. on track. Their comments and suggestions have led to many new directions explored in this thesis. Collaboration with Dr. Bijay Aggarwalla was a valuable experience. All the discussions about the theoretical side of the open quantum system and quantum thermodynamics with him were extremely delightful.

I am grateful to my senior lab members: Dr. Abhishek, Dr. Swathi, and Anjusha, for teaching me the basics of NMR experiments. Working alongside undergraduate student Govind Unnikrishnan, Gourav Bhole, Varad Pande, and Sachin Varleker was a great experience. Thanks to my current labmates Sudheer, Dr. Rupak, Soham, Krithika, Priya, and Anjali for insightful discussion (academic or non-academic), which I have benefited greatly from.

Thanks to all the members of NMR research center past and present - Nitin Dalvi, Sachin Kate, Dipali, and Chinmay. Special thanks to Nitin Dalvi for all the help regarding instrumentation over the years.

Thanks to all my 19 batchmates for making life extremely enjoyable outside the lab. I hope everyone graduates very soon. Best batch ever!

Finally, I thank my family for constant support and their persistent questions like "When is it getting over?" which has played a significant role in the timely finishing of my Ph.D.

Abstract

The basic unit of quantum information is called a *qubit*, and it can physically be realized using a two-level quantum system. The devices which manipulate qubits to process quantum information for practical applications are called *quantum technologies*. In certain cases, provided enough number of qubits, these devices can significantly outperform their traditional counterparts. However, a quantum system invariably interacts with its surrounding environment and consequently gets exposed to environmental noise, which in turn limits the efficiency of quantum technologies. Thus, ensuring fault-tolerance against environmental noise is vital in unlocking the real potential of these devices.

Currently, the quantum technologies available to us are not entirely fault-tolerant. Nevertheless, in the very near future, large enough qubits are likely to be at our disposal to show the superiority of these noisy devices over their traditional counterparts. These devices are called Noisy Intermediate-Scale Quantum (NISQ) [1] technology. Although the opportunity to experiment with NISQ technology is tempting and should be grabbed with both hands, the quantum community must be cautious not to lose sight of the essential longer-term goal to build fault-tolerant quantum devices. Keeping this caution in mind, broadly, I am interested in contributing to the robust implementation of quantum technologies. My thesis is mainly centered on the following two questions: How to efficiently characterize environmental noise acting on a quantum system? And how to design optimized control strategies for suppressing environmental noise? In my doctoral research, I have made an effort to address these questions from both fundamental as well as practical perspectives utilizing nuclear magnetic resonance (NMR) methods. Specifically, in fundamental aspects, concepts such as quantum non-Markovianity and information scrambling are explored, which involve precise characterization of information exchange between the quantum system and the surrounding environment. In practical aspects, I have worked towards investigating control protocols for estimation and suppression of environmental noise, with an emphasis on practical constraints motivated by realistic experimental scenarios. This thesis is divided into five chapters. An outline and chapter-wise abstracts are given below.

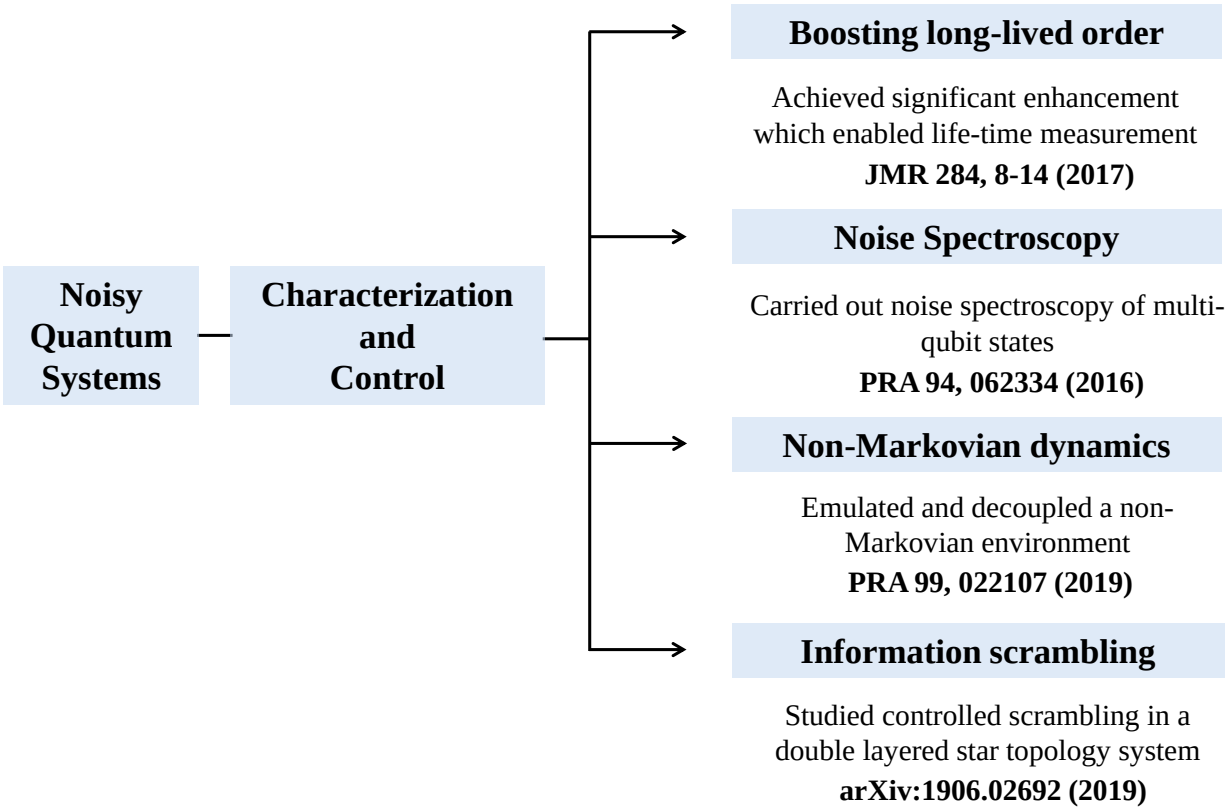

Chapter 1– Introduction

Chapter 1 introduces the concepts and terminology required for the thesis. Here I describe quantum information processing (QIP) and its physical realization using NMR methods. Also, separate sections are devoted to the discussion of the interaction between a quantum system and the surrounding environment leading to loss of information due to noise and the physical mechanisms responsible for environmental noise in NMR quantum systems.

Chapter 2– Enhancement of long-lived singlet-order using optimal control

In certain cases, it is possible to initialize the quantum system in specific subspaces of states which are immune to environmental noise. In NMR terminology, these subspaces are known as long-lived singlet order (LLS). Under favorable conditions, LLS can be sustained for a very long time, and as a result, it has a wide range of applications in NMR. However, detection of LLS in naturally rare nuclei is a challenge and may require sophisticated instrumentation along with long

experimental times. In this chapter, we experimentally demonstrate the significant enhancement of the LLS content in naturally rare nuclei via coherent manipulation of a large qubit system using optimal control techniques without requiring any additional hardware.

Chapter 3– Noise spectroscopy of multi-qubit states

To ensure maximum fault tolerance, the noise-suppression strategies must be judiciously optimized according to environmental noise. To this end, it is essential to have some a priori information about the noise itself. The method to characterize environmental noise is called noise spectroscopy. The investigation of noise affecting singlet qubit states is extensively reported in the literature. In this chapter, we report an experimental study of noise affecting some special multi-qubit states.

Chapter 4– Emulation and control of quantum non-Markovian dynamics

Often it is assumed that the surrounding environment is an infinite reservoir, and the information lost from the quantum system immediately gets dispersed into many degrees of freedom of the environment. These kinds of environments are called *memoryless* or *Markovian environments*. However, in many realistic experimental scenarios, the environments are finite, and they have memory effects associated with them, which manifests as information backflow to the system. These kinds of environments are called *non-Markovian environments*. In this chapter, we experimentally emulate these environments using NMR methods and study dynamics of information flow between the system and the environment. We also optimize protection strategies in the presence of information backflow associated with the non-Markovian environment and experimentally study their efficiencies.

Chapter 5– Unambiguous measurement of information scrambling

The loss of quantum information from the system to the environment is a non-unitary or irreversible process. However, in certain many-body quantum systems, unitary dynamics can also lead to a perceived loss of quantum information in practical timescales. This happens due to the spreading of initially localized information into non-local degrees of freedom of the system, and it is called *information scrambling*. This phenomenon is used to further our insight into many

fundamental issues not only in QIP but also in condensed matter and high energy physics.

The information loss due to scrambling is experimentally measurable, but its detection can be confused with information loss due to environmental noise. To this end, in this chapter, we propose and experimentally demonstrate a protocol to filter out contributions solely due to scrambling. Till now, the scrambling of information localized in initially uncorrelated degrees of freedom was experimentally investigated. We go one step further and study scrambling of information initially localized in multi-qubit correlations.

List of Publications

1. **Deepak Khurana**, V.R. Krithika , and T. S. Mahesh, *Unambiguous measurement of information scrambling in a hierarchical star-topology system*, arXiv:1906.02692 (2019).

2. **Deepak Khurana**, Bijay Kumar Agarwalla, and T. S. Mahesh, *Experimental emulation of quantum non-Markovian dynamics and coherence protection in the presence of information back-flow*, Phys. Rev. A 99, 022107 (2019).

3. **Deepak Khurana**, and T. S. Mahesh, *Bang-bang optimal control of large spin systems: Enhancement of* ^{13}C- ^{13}C *singlet-order at natural abundance,* Journal of Magnetic Resonance 284, 8-14 (2017).

4. Varad R. Pande, Gaurav Bhole, **Deepak Khurana**, and T. S. Mahesh, *Strong algorithmic cooling in large star-topology quantum registers,* Phys. Rev. A 96, 012330 (2017).

5. Bharat Tandon, Anur Yadav, **Deepak Khurana**, Pranavi Reddy, Pralay K. Santra, and Angshuman Nag, *Size-Induced Enhancement of Carrier Density, LSPR Quality Factor, and Carrier Mobility in Cr-Sn Doped* In_2O_3 *Nanocrystals,* Chemistry of Materials 29 (21), 9360-9368 (2017).

6. **Deepak Khurana**, Govind Unnikrishnan, T. S. Mahesh, *Spectral investigation of the noise influencing multi-qubit states,*Phys. Rev. A 94, 062334 (2016).

Contents

CHAPTER 1

Introduction

What are the ultimate physical limits of technology? Each attempt made to answer this question pushes these very limits one step further. The latest addition to these attempts is a cross-disciplinary venture from physicists, mathematicians, and computer scientists in the form of *Quantum technologies* [2]. Quantum technologies are physical devices that use fundamental laws of quantum mechanics to harness the resources available at the sub-atomic level for practical applications. Essentially these devices are efficient processors of information encoded in the state of a quantum system, called *quantum information*, according to the task at hand. These devices include quantum computers [3], that can solve hard problems which are impossible to solve on traditional supercomputers in feasible timescales; sensors [4] of physical quantities like a magnetic field, temperature, electric field, etc., with unprecedented precision. Similar to quantum computers and quantum sensors, quantum systems are actively exploited for other promising practical applications like quantum metrology, quantum communication, quantum cryptography, etc. [5, 6] and it has led to significant attention from technology giants like Google, Microsoft, and IBM to develop industry-grade quantum devices.

However, in reality, the power of quantum technologies is severely limited by noise introduced due to unwanted interaction of the quantum system with its surrounding environment. For quantum technologies to reach the market, environmental-induced noise must be appropriately understood and mitigated to an acceptable degree below a certain threshold [7]. To this end, the goal of understanding the interaction between system and environment has led to the theory of open quantum systems [8], and tremendous effort has been put to develop protocols to boost the robustness of quantum devices against the destructive effects of the environment.

In this chapter, the first section 1.1 is devoted to the following questions: (i) How to encode information in the state of a quantum system? (ii) How does the processing and readout of quantum information take place? In section 1.2, I describe how quantum information gets corrupted due to the interaction with the surrounding environment. Finally, in section 1.3 and 1.4, respectively,

I outline the physical realization of a quantum information processor using Nuclear Magnetic Resonance (NMR) methods and noise mechanisms hindering its error-free operation.

1.1 Quantum information processing (QIP)

1.1.1 Qubits

Qubit is the unit of quantum information analogous to the bit (binary digit) in traditional technologies. A bit can be represented by a two-state system such as an electrical circuit that allows two voltage levels, usually denoted by 0 and 1. Similarly, we can physically realize a qubit by a two-state quantum-mechanical system, usually represented by kets $|0\rangle$ and $|1\rangle$, such as the spin of an electron or the polarization of a photon. While a bit can only exist in one or the other of computational states, namely 0 and 1, a qubit can exist in a coherent superposition of its basis states $|0\rangle$ and $|1\rangle$. A general superposition state can be written as

$$|\psi\rangle = \alpha|0\rangle + \beta|1\rangle, \tag{1.1}$$

where α and β are the complex numbers which satisfy $|\alpha|^2 + |\beta^2| = 1$. The set of states $\{|\psi\rangle\}$ form a complex vector space with unit norm.

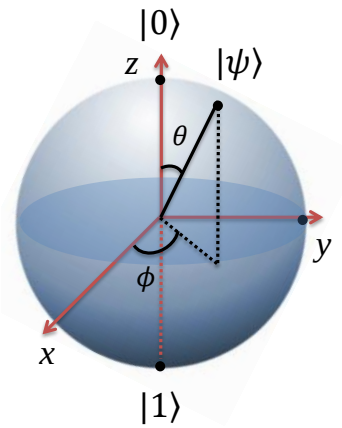

Figure 1.1: Bloch sphere representation of states of a single qubit

The state of the qubit can be geometrically represented by a unit Bloch sphere as shown in Fig 1.1. Here $\alpha = \cos(\theta/2)$ and $\beta = e^{i\phi}\sin(\theta/2)$ where $\theta \in [0, \pi]$ and $\phi \in [0, 2\pi]$. Operations on qubit can be easily visualized as rotation on the Bloch sphere.

In contrast to the classical bit whose state can be determined with certainty, the outcome of the measurement of the state of a qubit is always probabilistic. For example, when the state $|\psi\rangle$ is subjected to measurement, we get $|0\rangle$ and $|1\rangle$ with probabilities $|\alpha|^2$ and $|\beta|^2$ respectively. This probabilistic nature of the measurement outcome demands experimentalists to take either measurement of a large number of copies of the qubit or a large number of sequential measurements of a single qubit with identical state preparation, to obtain appropriate expectation values.

A system consisting of multiple qubits is called a *quantum register*. As a result of superposition, a N qubit quantum register can hold information equivalent to 2^N bits, which means that the appropriate control of dynamics of N qubits can provide exponentially faster processing of information. A general quantum state of N qubits can be written as a linear superposition of basis states formed by the direct product of basis states spanning the Hilbert space of each qubit. In other words, if $\mathcal{H}_\mathcal{A}$ and $\mathcal{H}_\mathcal{B}$ are Hilbert space of qubit A and B, then Hilbert space of the composite system will be $\mathcal{H}_\mathcal{A} \otimes \mathcal{H}_\mathcal{B}$. Hence, for a N qubit system, dimension of the Hilbert space is 2^N and accordingly these many basis states are required. For example, in case of two qubits, the computational basis constitutes four states namely $|00\rangle, |01\rangle, |10\rangle$ and $|11\rangle$ and a general two-qubit state can be written as

$$|\psi\rangle = \alpha|00\rangle + \beta|01\rangle + \gamma|10\rangle + \delta|11\rangle, \tag{1.2}$$

with $|\alpha|^2 + |\beta|^2 + |\gamma|^2 + |\delta|^2 = 1$.

Apart from the phenomenon of superposition, multiple-qubit states also exhibit important properties such as entanglement, which can be exploited to boost the performance of quantum technologies. Entangled states are the special multi-qubit quantum state which cannot be written as the direct product of the states of its constituents qubits. To be precise, if $|\psi_1\rangle$, $|\psi_2\rangle$, $|\psi_3\rangle, ..., |\psi_N\rangle$ are states of each qubit in a N qubit system then entangled states of the composite system can not be written as $|\psi_1\rangle \otimes |\psi_2\rangle \otimes |\psi_3\rangle \otimes .... \otimes |\psi_N\rangle$. The states which are not entangled are termed as separable states. For example, in case of two qubits, while the Bell states $\{(|00\rangle \pm |11\rangle)/\sqrt{2}, (|01\rangle \pm |10\rangle)/\sqrt{2}\}$ are entangled, the states such as $(|00\rangle + |01\rangle)/\sqrt{2}$ are separable. The Bell states have the following property: The qubits exhibit non-local correlations. For example, in case of $(|00\rangle + |11\rangle)/\sqrt{2}$, after measuring σ_z observable on the first qubit we get 0 or 1, each with probability 1/2, with corresponding post-measurement states being $|00\rangle$ or $|11\rangle$.

Therefore, measurement results of both the qubits are correlated since the measurement of the second qubit always gives the same result as the first qubit. Entanglement is an essential ingredient of various quantum communication protocols such as quantum cryptography, superdense coding, and quantum teleportation [9].

1.1.2 Density operator formalism

In certain experimental scenarios, a qubit is realized using an ensemble of identical quantum particles, such as in NMR. In this case, dealing with the statistical ensemble of kets is rather cumbersome and alternative way of representing the quantum state using *density operator* is often convenient. A density operator is a linear operator with its matrix representation named as density matrix, which depends upon the choice of the basis in the underlying Hilbert space. If all the member of ensembles are in same state $|\psi\rangle = \sum_j c_j|j\rangle$ with orthonormal basis $\{|j\rangle\}$, ensemble is called pure and density operator is given by

$$\rho = |\psi\rangle\langle\psi| = \sum_{j,k} c_j^* c_k |j\rangle\langle k|. \tag{1.3}$$

In this case density matrix is idempotent, i.e., $\rho^2 = \rho$.

For a *mixed* ensemble of states $|\psi_i\rangle$ each with probability p_i, the density operator can be written as

$$\rho = \sum_i p_i \rho_i = \sum_i p_i |\psi_i\rangle\langle\psi_i| = \sum_i p_i \sum_{j,k} c_j^* c_k |j\rangle\langle k| = \sum_{j,k} \overline{c_j^* c_k} |j\rangle\langle k| \tag{1.4}$$

with $\sum_i p_i = 1$ and overbar denotes the ensemble average. The above density matrix can be interpreted as mixture of the pure states ρ_i with probabilities p_i. A density operator have following important properties:

1. ρ is a positive operator, which means that all eigenvalues must be non-negative.
2. $\mathrm{Tr}[\rho] = 1$,i.e., sum of all the eigenvalues must be unity.
3. ρ is Hermitian, i.e., $\rho^\dagger = \rho$. It amounts to the fact that elements in the upper triangle of the density matrix are the complex conjugate of that in the lower triangle.

Also, note that for pure states and mixed states, respectively, $\mathrm{Tr}[\rho^2] = 1$ and $\mathrm{Tr}[\rho^2] < 1$. The

identity matrix ($\mathbb{1}/2$) represents the maximally mixed state with $\mathrm{Tr}[\rho^2] = 1/2$. Hence $\mathrm{Tr}[\rho^2]$ is often termed as the *purity* of a quantum state.

Geometrically, in terms of Bloch sphere, the most general state of a single qubit can be written as

$$\rho = \frac{\mathbb{1} + r.\sigma}{2}, \tag{1.5}$$

where $\mathbb{1}$ is identity matrix, r is a three dimensional Bloch vector such that $||r|| \leq 1$, and $\sigma = \sum_{i=x,y,z} \sigma_i$. Here

$$\sigma_x = \begin{pmatrix} 0 & 1 \\ 1 & 0 \end{pmatrix}; \quad \sigma_y = \begin{pmatrix} 0 & -i \\ i & 0 \end{pmatrix}; \quad \sigma_z = \begin{pmatrix} 1 & 0 \\ 0 & -1 \end{pmatrix}. \tag{1.6}$$

All the pure states and mixed states lie on and inside the surface of the Bloch sphere respectively. As purity decreases, states move inside the Bloch sphere with identity matrix lying at the center of it.

1.1.2.1 Populations and coherences

The physical significance of density operator can be better understood by looking at the element of the density matrix. For a pure state

$$\rho_{rs} = \langle r|\rho|s\rangle = \sum_{j,k} c_j^* c_k \langle r|j\rangle\langle k|s\rangle = c_r^* c_s, \tag{1.7}$$

and for a mixed state

$$\rho_{rs} = \langle r|\rho|s\rangle = \sum_i p_i c_r^{i*} c_s^i = \overline{c_r^* c_s}. \tag{1.8}$$

Due to Hermitian property of density operator

$$\langle r|\rho|s\rangle = \langle s|\rho|r\rangle^*. \tag{1.9}$$

In the eigenbasis of Hamiltonian, the diagonal element

$$\rho_{rr} = \overline{|c_r|^2} \tag{1.10}$$

represent *population* [10, 11] of the state $|r\rangle$. The off-diagonal element

$$\rho_{rs} = \overline{c_r^* c_s} \tag{1.11}$$

is called *coherence* [10, 11] because it indicates a coherent superposition of state $|r\rangle$ and $|s\rangle$.

1.1.2.2 Coherence order

Often, it is very useful to classify coherences based on magnetic quantum number associated with states participating in the coherence. If a magnetic field is applied in z-direction then eigenstate $|r\rangle$ and $|s\rangle$ of Hamiltonian has a well defined angular momentum in z-direction [11]

$$\begin{aligned} I_z|r\rangle &= m_r|r\rangle, \\ I_z|s\rangle &= m_s|s\rangle, \end{aligned} \tag{1.12}$$

where $I_\alpha = \sigma_\alpha/2$ with $\alpha \in x, y, z$ are called spin operators. Then order q of the coherence is defined as

$$q = m_r - m_s. \tag{1.13}$$

A coherence having coherence order q is called q-quantum coherence. For a N-qubit system, dimensions of density matrix are $2^N \times 2^N$ amounting to total of 2^{2N} elements. There are 2^N diagonal elements representing populations and rest of them are coherences. Coherence with order $q = \pm 1$ are called single quantum coherences and $q \neq \pm 1$ are called multiple-quantum coherences (MQC). Coherences can be further divided into two types. Consider a $3-$qubit system and following two particular coherences out of total 56 coherences

(i) Coherence between eigenstates $|000\rangle$ and $|001\rangle$ has coherence order $+1$. Here the first two qubits are not involved in the transition and termed as passive qubits while the third qubit is the active qubit.

(ii) Coherence between eigenstates $|001\rangle$ and $|110\rangle$ also has coherence order $+1$. Here all three qubits are active.

The later type of coherences in which the number of active spins is larger than coherence order are called *combination* coherences. In contrast, the former case where the number of active spins is equal to coherence order are called *simple* coherences [11]. In this thesis, combination

quantum coherences are utilized to estimate noise affecting various qubits participating in the coherence and to study spreading of information in multi-qubit correlations in chapter 3 and chapter 5 respectively.

1.1.2.3 Reduced density operator

The density matrix description is a handy tool for finding out the state of the sub-system, called the reduced density operator, using the state of the composite system. Suppose the composite system is in state ρ_{AB}, then reduced density operator of the sub-system A is defined as

$$\rho_A = \mathrm{Tr}_B[\rho_{AB}], \tag{1.14}$$

where Tr_B is a map from Hilbert space of composite system AB to Hilbert space of subsystem A, called the partial trace over system B and defined as following. If $\rho_{AB} = \sum_{ijkl} c_{ijkl}|a_i\rangle\langle a_j| \otimes |b_k\rangle\langle b_l|$ then partial trace

$$\rho_A = \mathrm{Tr}_B[\rho_{AB}] = \sum_{ijkl} c_{ijkl}|a_i\rangle\langle a_j|\langle b_l|b_k\rangle = \sum_{ijk} c_{ijkk}|a_i\rangle\langle a_j|. \tag{1.15}$$

The reduced density operator description is justified in the sense that it produces correct measurement statistics for measurement made on A [9].

The reduced density operator description is very helpful in deciding if the state of the composite system is entangled or not. If the state of the composite system is a pure separable state, then its reduced density operator will be a pure state. On the other hand, if the composite system is described by an entangled state, then its reduced density operator will be a mixed state.

1.1.2.4 Trace distance between two quantum states

Trace distance is a metric on the space of the density matrices. For two density matrices ρ_1 and ρ_2, the trace distance is defined as half the trace norm

$$\mathcal{D}(\rho_1, \rho_2) = ||\rho_1 - \rho_2||/2, \tag{1.16}$$

where the trace norm is defined as $||\rho|| = \sqrt{\rho^\dagger \rho}$. Since the density matrices ρ_1 and ρ_2 are hermitian operators, the trace distance is simplified to

$$\mathcal{D}(\rho_1, \rho_2) = \mathrm{Tr}\left[\sqrt{\rho_1 - \rho_2}\right]/2 = \sum_i \lambda_i, \tag{1.17}$$

where λ_i are eigenvalues of the hermitian matrix $(\rho_1 - \rho_2)$. For Bloch sphere representation (Eq. 1.5) of density matrices ρ_1 and ρ_2 with Bloch vector r and s, the trace distance is half the Euclidean distace

$$\mathcal{D}(\rho_1, \rho_2) = ||\rho_1 - \rho_2||/2 \tag{1.18}$$

$$= ||(r - s).\sigma||/4 \tag{1.19}$$

$$= |r - s|/2. \tag{1.20}$$

The trace distance has the following properties

1. $0 \leq \mathcal{D}(\rho_1, \rho_2)$ with equality when $\rho_1 = \rho_2$.
2. $\mathcal{D}(\rho_1, \rho_2) \leq 1$ with equality when ρ_1 and ρ_2 are orthogonal.
3. It is symmetric in its inputs: $\mathcal{D}(\rho_1, \rho_2) = \mathcal{D}(\rho_2, \rho_1)$.
4. It satisfies triangular identity: $\mathcal{D}(\rho_1, \rho_2) \leq \mathcal{D}(\rho_1, \rho_0) + \mathcal{D}(\rho_0, \rho_2)$.
5. It is preserved under Unitary transformations: $\mathcal{D}(U\rho_1 U^\dagger, U\rho_2 U^\dagger) = \mathcal{D}(\rho_1, \rho_2)$.
6. It is subadditive under tensor product: $\mathcal{D}(\rho_1 \otimes \rho_1', \rho_2 \otimes \rho_2') \leq \mathcal{D}(\rho_1, \rho_2) + \mathcal{D}(\rho_1', \rho_2')$
7. It is convex in each of its inputs: $\mathcal{D}(\sum_i p_i \rho_1^i, \rho_2) \leq \sum_i p_i \mathcal{D}(\rho_1^i, \rho_2)$

1.1.2.5 Distinguishability of quantum states

The concept of trace distance is intimately connected to the concept of distinguishability of two quantum states. To elaborate, consider two parties Alice and Bob. Suppose Alice prepares two states ρ_1 and ρ_2 with probability $1/2$ each and send it to Bob. Bob's task is to find out the state of the system with a single measurement. The maximum probability of success in this task with an optimal strategy is related to trace distance by $\frac{1+\mathcal{D}(\rho_1,\rho_2)}{2}$. Due to this relation, trace distance can be interpreted as distinguishability. For example, suppose that ρ_1 and ρ_2 are orthogonal. In this case,

$\mathcal{D}(\rho_1, \rho_2) = 1$, and the probability of success is 1, which is a well-known fact that orthogonal states can be distinguished with certainty. Similarly if $\rho_1 = \rho_2$, $\mathcal{D}(\rho_1, \rho_2) = 0$, probability of success is $1/2$ and in this case the two states ρ_1 and ρ_2 can not be distinguished at all with any optimal strategy.

1.1.2.6 Von-Neumann entropy

For a quantum states ρ, the von-Neumann entropy is given by

$$\mathcal{S}(\rho) = -\mathrm{Tr}[\rho \log_2 \rho] \tag{1.21}$$

and it can be simplified using eigendecomposition of $\rho = \sum_i \lambda_i |i\rangle\langle i|$ in the following way

$$\mathcal{S}(\rho) = -\sum_i \lambda_i \log_2 \lambda_i. \tag{1.22}$$

For pure states $\mathcal{S}(\rho) = 0$ since density matrix is idempotent $\rho^2 = \rho$ and for a maximally mixed states $\mathcal{S}(\rho) = \log_2 N$, where N is the dimenssion of the system. Von-Neumann entropy has following properties

1. $\mathcal{S}(\rho)$ is invariant under a unitary transformation, $\mathcal{S}(\rho) = U\mathcal{S}(\rho)U^\dagger$.
2. $\mathcal{S}(\rho)$ is a concave function: $\mathcal{S}\left(\sum_i \lambda_i \rho_i\right) \geq \sum_i \lambda_i \mathcal{S}(\rho_i)$.
3. $\mathcal{S}(\rho)$ is additive under tensor product, i.e., for two independent systems given by ρ_A and ρ_B: $\mathcal{S}(\rho_A \otimes \rho_B) = \mathcal{S}(\rho_A) + \mathcal{S}(\rho_B)$.
4. $\mathcal{S}(\rho)$ is subadditive in the sense: $\mathcal{S}(\rho_{AB}) \leq \mathcal{S}(\rho_A) + \mathcal{S}(\rho_B)$.

1.1.3 Quantum gates

In traditional technologies, processing of information takes place using physical tools known as logic gates such as NOT, OR, NOR, etc. Similarly, the processing of information in quantum technologies is done via quantum gates. Quantum gates are nothing but unitary operators acting on qubits such that an initial state is transformed into the final desired state. If a qubit starts in an initial state $|\psi(0)\rangle$, then application of unitary operator U transforms it to

$$|\psi(t)\rangle = U|\psi(0)\rangle. \tag{1.23}$$

Since $UU^\dagger = \mathbb{1}$, quantum gates are reversible in nature. In terms of density operator formalism, it can be readily shown that

$$\rho(t) = U\rho(0)U^\dagger. \tag{1.24}$$

For a quantum quantum system described by Hamiltonian $H(t)$, the dynamics is governed by Schrödinger equation (assuming $\hbar = 1$)

$$\frac{\partial|\psi(t)\rangle}{\partial t} = -iH(t)|\psi(t)\rangle, \tag{1.25}$$

where $|\psi(t)\rangle$ is time evolved state. Similarly in density matrix picture dynamics is governed by von Neumann equation

$$\frac{\partial\rho(t)}{\partial t} = -i[H(t), \rho(t)]. \tag{1.26}$$

The solution of above equations leads to unitary time evolution of the form

$$U = \mathcal{T}\exp\left(-i\int_0^t H(t')dt'\right), \tag{1.27}$$

where $\mathcal{T}$ is Dyson time ordering operator. For single qubit, unitary operator U can be visualized as rotations on the Bloch sphere,

$$U = e^{i\alpha}R_{\hat{n}}(\theta), \tag{1.28}$$

for some α and rotation $R_{\hat{n}}(\theta) = \exp(-i\theta\hat{n}.\sigma/2)$ with $\sigma = \sum_{i=x,y,z}\sigma_i$ which represents a rotation of angle θ about axis $\hat{n}$.

In the following, we give some examples of widely used single and two-qubit quantum gates. To construct multi-qubit gates, it was shown in Ref. [12] that set of gates consisting of one qubit quantum gates (local gates) and two-qubit controlled gates (for example CNOT gate described below) is universal, i.e., unitary operations on arbitrarily many qubits can be expressed as a combination of single-qubit and two-qubit controlled quantum unitary gates.

X (NOT), Y and Z gate

Matrix representation of X, Y, and Z gate is that of $\sigma_x, -i\sigma_y$ and σ_z operator shown in Eq. 1.6. Similar to classical NOT gate, X gate inverts the basis state of the qubit from $|0\rangle$ to $|1\rangle$ and vice-versa. The Z gate introduces a relative phase of π to the state $|1\rangle$, i.e., $\alpha|0\rangle + \beta|1\rangle \rightarrow \alpha|0\rangle - \beta|1\rangle$. The Y gate inverts the basis states along with putting a relative phase to the state $|1\rangle$, i.e.,

$\alpha|0\rangle + \beta|1\rangle \rightarrow -\alpha|1\rangle + \beta|0\rangle$.

Hadamard gate

Application of Hadamard gate on a basis state produces equal superposition of the basis states and vice versa. Its Matrix representation is

$$H = \frac{1}{\sqrt{2}} \begin{bmatrix} 1 & 1 \\ 1 & -1 \end{bmatrix} \tag{1.29}$$

and its action on $|0\rangle$ and $|1\rangle$ basis states transforms them to $|+\rangle = \frac{|0\rangle+|1\rangle}{\sqrt{2}}$ and $|-\rangle = \frac{|0\rangle-|1\rangle}{\sqrt{2}}$ respectively. Note that $H^2 = \mathbb{1}$, hence two consecutive applications of Hadamard gate does not change the state.

Controlled-Not (CNOT) gate

CNOT gate is a two qubit gate where one qubit works as control and other one act as target. Action of this gate is to perform a NOT operation on the target qubit depending upon the state of the control qubit. To be precise, it performs a selective inversion of the state of the target qubit if control qubit is in $|1\rangle$ state. It has the following matrix representation

$$\text{CNOT} = \begin{bmatrix} 1 & 0 & 0 & 0 \\ 0 & 1 & 0 & 0 \\ 0 & 0 & 0 & 1 \\ 0 & 0 & 1 & 0 \end{bmatrix}. \tag{1.30}$$

1.1.4 Measurement of the state of quantum register

When an experimentalist measures a quantum state, it collapses arbitrarily to one of the eigenstates of the measured observable. An observable is a Hermitian operator corresponding to physical quantities such as position, energy, or spin that can be measured. During the measurements, the system interacts with an external physical system (the measuring apparatus), which forces the dynamics to occur in non-unitary fashion. In quantum theory, measurements are postulated [9] using a collection of operator $\{M_m\}$, called the measurement operators. If the state before the measurement is given by $|\psi\rangle$ the probability of obtaining the measurement outcome m is given

by

$$p(m) = \langle\psi|M_m^\dagger M_m|\psi\rangle \tag{1.31}$$

and the state after the measurement can be written as

$$\frac{M_m|\psi\rangle}{\sqrt{p(m)}}. \tag{1.32}$$

The measurement operators satisfy completeness relation $\sum_m M_m^\dagger M_m = \mathbb{1}$ which translates to $\sum_m p(m) = 1$.

1.1.4.1 Projective measurement

A special case of the above-mentioned measurement postulate is the projective measurement when M_m are orthogonal operators. It is described by an observable $M = \sum_m mP_m$, where $P_m = |m\rangle\langle m|$ is projector onto eigenspace of M corresponding to eigenvalue m. In this case, the probability of obtaining the measurement outcome m is given by

$$p(m) = \langle\psi|P_m|\psi\rangle \tag{1.33}$$

and the state after the measurement can be written as

$$\frac{P_m|\psi\rangle}{\sqrt{p(m)}}. \tag{1.34}$$

1.1.4.2 Expectation value of an observable

In experiments, it is often required to calculate the average of the observable after several measurements, called the expectation value. In terms of projective measurement, it can be written as

$$\langle M\rangle = \sum_m mp(m) \tag{1.35}$$

$$= \langle\psi|M|\psi\rangle. \tag{1.36}$$

In case of a mixed state $\rho = \sum_i p_i |\psi_i\rangle\langle\psi_i|$, the expectation value can be written as

$$\begin{aligned}\langle M \rangle &= \sum_i p_i \langle\psi_i|M|\psi_i\rangle \\ &= \sum_i p_i \mathrm{Tr}[|\psi_i\rangle\langle\psi_i|M] \\ &= \mathrm{Tr}\left(\sum_i p_i (|\psi_i\rangle\langle\psi_i|M)\right) \\ &= \mathrm{Tr}[\rho M]. \end{aligned} \tag{1.37}$$

1.2 Why does a quantum system get noisy?

1.2.1 Open quantum systems

Until now, I have described the dynamics of a *closed quantum system* in the sense that it does not have unwanted interaction with the surroundings. However, in realistic laboratory conditions, a quantum system is never isolated but open to unavoidable interactions with the surrounding environment, called an *open quantum system* (OQS). The unwanted interaction with the surrounding environment introduces noise in the dynamics of the quantum system and makes superposition and entangled states very fragile to handle. As a result of this noise, despite being aware of the overwhelming capacity of quantum technologies to outperform their existing counterparts for the last two decades, we are still struggling to operate them in a fault-tolerant manner. Therefore understanding and controlling these processes is of utmost importance to ensure error-free operation of quantum devices. In the following, I describe some essential features of open quantum dynamics.

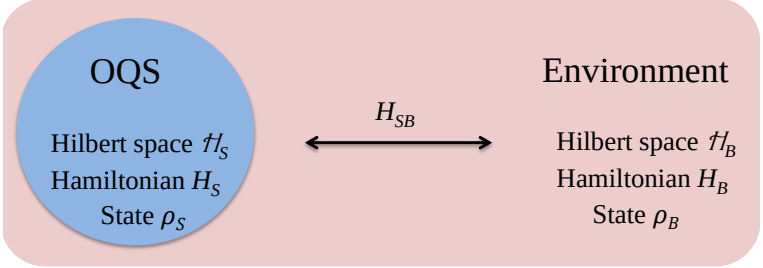

Figure 1.2: An open quantum system (OQS)

Consider a quantum system S interacting with the surrounding environment B. Let $\mathcal{H}_S$ and

$\mathcal{H}_B$ denote the Hilbert space corresponding to the system and environment, respectively, then Hilbert space of the composite system is $\mathcal{H}_{SB} = \mathcal{H}_S \otimes \mathcal{H}_B$. The system and environment are governed individually by Hamiltonian H_S and H_B, respectively, and interacting via Hamiltonian H_{SB} (see Fig. 1.2). The total Hamiltonian of the full $S + B$ system is given by

$$H = H_S + H_B + H_{SB}. \tag{1.38}$$

The dynamics of the composite system is governed by von Neumann equation

$$\frac{\partial \rho_{SB}(t)}{\partial t} = -i[H, \rho_{SB}(t)] \tag{1.39}$$

which yields the formal solution

$$\rho_{SB}(t) = U \rho_{SB}(0) U^\dagger, \tag{1.40}$$

where

$$U = \mathcal{T} \exp(-i \int_0^t H(t')dt'). \tag{1.41}$$

The overall state of the composite system $\rho_{SB}(t)$ evolves unitarily, as shown in Eq. 1.40 but measuring the state $\rho_{SB}(t)$ is very challenging since the surrounding environment is not under the experimentalist's control. Hence one can only determine time evolution of reduced state of the system $\rho_S(t) = \mathrm{Tr}_B[\rho_{SB}(t)]$. The equation of motion, called the *master equation*, for the time evolution of $\rho_S(t)$ derived from the integration of Eq. 1.39 is complicated and depends upon coupling between OQS and the environment.

1.2.2 Dynamical map

IIn the following, we describe an equivalent approach to describe the reduced dynamics of OQS. First, we assume the initial state of the composite system is separable, i.e.,

$$\rho_{SB}(0) = \rho_S(0) \otimes \rho_B(0), \tag{1.42}$$

which leads to following expression for time evolution for the reduced state of the system

$$\rho_S(t) = \mathrm{Tr}_B[U(t)\rho_S(0) \otimes \rho_B(0)U^\dagger(t)]. \tag{1.43}$$

For a fixed environment initial state $\rho_B(0)$, above equation defines a linear map Φ_t [8, 9, 13] on the state space of the OQS which maps the initial reduced system state $\rho_S(0)$ to final reduced system state $\rho_S(t)$ according to

$$\rho_S(0) \to \rho_S(t) = \Phi_t \rho_S(0). \tag{1.44}$$

Here Φ_t is called the *dynamical map*. In contrast to closed system dynamics, the states of OQS evolving according to the dynamical map experience decoherence, describing the transformation from pure states (coherent superposition) to mixed states (incoherent superposition or statistical mixture) [14]. The dynamical map satisfies the following properties to map physical states into physical states

1. Φ_t preserves trace and Hermiticity of the operators.

2. Φ_t is a *convex linear map*, i.e., for the probabilities p_i

$$\Phi_t \left(\sum_i p_i \rho_i \right) = \sum_i p_i (\Phi_t \rho_i) \tag{1.45}$$

3. Φ_t is a *completely positive* map [15–17].

Complete positivity of dynamical map plays an essential role in fault-tolerant quantum error correction [18] and can be defined in the following two equivalent ways [9]

(i) A linear operator Φ_t is completely positive if it admits a *Kraus* representation [19], i.e.,

$$\Phi_t \rho = \sum_i E_i^\dagger \rho E_i \tag{1.46}$$

with a set of operator E_i on the underlying Hilbert space $\mathcal{H}_S$ such that $\sum_i E_i^\dagger E_i = \mathbb{1}_S$.

(ii) Consider a Hilbert space $\mathcal{H}_S \otimes \mathbb{C}^n$ corresponding to a Hilbert space of system $\mathcal{H}_S$ combined with an n-level system R and a map $\Phi_t \otimes \mathbb{1}_n$ acting on this combined system. We can then define that a map Φ_t to be completely positive if $\Phi_t \otimes \mathbb{1}_n$ is positive for all n.

Hence, complete positivity is a stronger condition than positivity. The requirement of only positivity ensures that evolved states of the reduced system $\Phi_t \rho_S(0)$ are valid density operators. However, when the system S is a part of a larger system $S + R$, it might happen that the evolved

state of the composite system ρ_{SR} may not be a valid density operator. This is because of the development of entanglement between S and R, which does not occur in classical dynamics and is a genuine quantum feature [20]. Therefore, similar to reduced states of the system, the requirement of complete positivity ensures that all physical states of the composite system are also mapped to physical states of the composite system.

1.2.3 Markovian description

In the Markovian regime, the following approximations are made to derive a master equation for the dynamics of the reduced OQS

(i) *Weak coupling or Born approximation* - Under this assumption, there is no significant development of system-environment correlations. Consequently the environment is effectively unchanged, i.e, it has no memory of past states of the OQS.

(ii) *Separation of timescales or Markov approximation* - If τ_E represents timescales corresponding to decay of environmental correlations and τ_R denotes the relaxation timescales over which state of OQS varies appreciably because of interaction with environment, this assumption amounts to relation $\tau_R >> \tau_E$.

(iii) *Rotating wave approximation* - Terms which oscillate faster compared to system dynamics can be neglected.

With these approximations, equation of motion for reduced state of OQS can be written in the Lindblad master equation form [21, 22]

$$\frac{\partial \rho_S(t)}{\partial t} = \mathcal{L}\rho_S(t) = -i[H_S, \rho_S(t)] + \sum_i \gamma_i \left(A_i \rho_S(t) A_i^\dagger - \frac{1}{2}\{A_i^\dagger A_i, \rho_S(t)\} \right), \tag{1.47}$$

where A_i are Lindblad operators, γ_i are positive constants called the decay rates, and $\mathcal{L}$ is operator corresponding to dynamical map $\Phi_t = e^{\mathcal{L}t}$. Here the first term describes the unitary evolution due to H_S and the second term describes the non-unitary effect of the environment. In this case the dynamical map obeys the *semi-group* property

$$\Phi_{t+t'} = \Phi_t \Phi_{t'}. \tag{1.48}$$

While the above Markovian description of the OQS dynamics is easy to handle, and certain

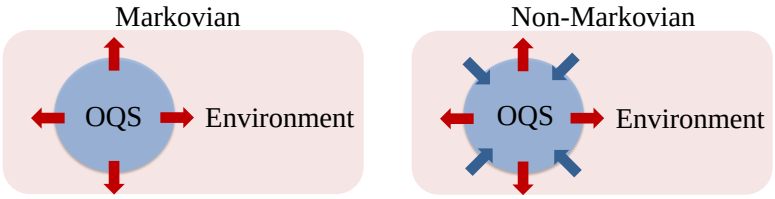

Figure 1.3: Difference between Markovian and non-Markovian OQS. Arrows indicate the flow of information. In the Markovian case, the quantum system always loses information to the environment, whereas, in the case of the non-Markovian environment, information backflow can take place.

physical systems satisfy the associated assumptions with it, in general, OQS are intrinsically non-Markovian. In many practical situations such as in the presence of strong system-environment coupling, low temperature, and structured environment, the above approximations are not justified. In these cases, the environment has memory effects, and they are manifested as information backflow from the environment to OQS [20, 23](see Fig. 1.3). From the perspective of the master equation, there exist time-local equations of the form Eq. 1.47 with time-dependent coefficients $\gamma_i(t)$ to describe these memory effects [24, 25]. In this case, the dynamical map can be written as

$$\Phi_t = \mathcal{T} \exp\left(\int_0^t \mathcal{L}_{t'} dt'\right) \tag{1.49}$$

and one can speak of time-dependent Markovian master equation when $\gamma_i \geq 0$, which leads to a dynamical map satisfying the divisibility property [26] analogous to semi-group property. Therefore, the departure of dynamics from divisibility property corresponding to $\gamma_i < 0$ signifies the presence of memory effects. More detailed discussion on definition and measures of non-Markovianity is given in chapter 4 in context to dephasing dynamics of a qubit governed by single Lindblad operator σ_z.

1.3 Quantum information processing using NMR

To act as an efficient processor of quantum information, any physical device has to satisfy the DiVincenzo criteria [27]. Though all the requirements are not satisfied by any one of the devices, various architectures are being explored in the literature. Some of these are

1. Nuclear magnetic resonance (NMR) [28, 29]

2. Nitrogen vacancy centers [30]

3. Superconducting qubits [31]

4. Quantum dots [32, 33]

5. Trapped ion quantum simulators [34].

In this thesis, we use NMR as our physical testbed for quantum information processing.

NMR is a physical phenomenon that involves placing the atomic nuclei in a strong static magnetic field and perturbing it by an external electromagnetic field at resonance, such that energy absorption can occur. In this thesis, we deal with *liquid state* NMR, where a solute containing nuclei of interest is dissolved in a liquid solvent to prepare an isotropic solution. In the following, I describe how qubits and quantum gates can be realized using the NMR methodology.

1.3.1 NMR qubits

1.3.1.1 A nuclear spin in a static external magnetic field

Along with mass and charge, atomic nuclei possess a physical property called *spin* [35]. A spin has associated angular momentum $\mathbf{I}$, which is quantized, and for a spin-I particle, it can take values of the form $\hbar\sqrt{I(I+1)}$, where I is called the spin quantum number. In addition to spin, the nuclei also possess magnetic moment μ which is proportional to spin angular momentum

$$\mu = \gamma\hbar\mathbf{I}, \tag{1.50}$$

where γ is called the gyromagnetic ratio, characteristic of the nucleus. Now we apply a strong static magnetic field B_0 along z-direction which can be described by *Zeeman* Hamiltonian of the form

$$H = -\gamma\hbar B_0 I_z = \hbar\omega_0 I_z, \tag{1.51}$$

where $I_z = \sigma_z/2$ is z-component of the spin angular momentum $\mathbf{I}$ and $\omega_0 = -\gamma B_0$ is called *Larmor frequency*. Intuitively, due to interaction with the magnetic field, nuclear spins feel a torque, and their magnetic moments start precessing about the field with frequency ω_0, which usually is in hundreds of MHz at the high magnetic field employed in NMR. The energy eigenvalues of the Hamiltonian H are $-m\gamma\hbar B_0$, where m is called the magnetic quantum number, which is quantized and takes values in the range $-I, -I+1, ..., 0, ..., I-1, I$. Therefore, the energy spectrum consists of $2I+1$ equally spaced energy levels with a gap of $\hbar\omega_0$.

In a molecule, the local magnetic field at the sight of the nucleus is different from the applied static field because the local field depends upon the shielding introduced due to electron clouds of the surrounding chemical environment. This lead to a slight modification in the Zeeman Hamiltonian

$$H = -\gamma(1-\sigma)B_0\hbar I_z, \tag{1.52}$$

where σ is known as *chemical shift tensor* [36]. Though this local field is tiny compared to B_0, it gives rise to a noticeable shift in Larmor frequency, called *chemical shift*, which plays a vital part in structural analysis.

1.3.1.2 Thermal equilibrium state

A qubit can be realized in NMR using an ensemble of spin-1/2 nuclei such as ^{1}H, ^{13}C, ^{19}F, etc. In the case of a single spin-1/2 nuclei, when the strong static magnetic field B_0 is applied, the degeneracy between energy eigenstates is lifted, forming a two-level system with spacing equal to $\hbar\omega_0$. In this thesis, we use magnetic fields of strength 9.4 T, 11.2 T, and 13.1 T, which corresponds to ^{1}H Larmor frequency of 400, 500, and 600 MHz, respectively. The ground and the excited state corresponding to $m = 1/2$ and $m = -1/2$ serves as basis states for the qubit, denoted as $|0\rangle$ and $|1\rangle$ with energy eigenvalues $\hbar\omega_0/2$ and $-\hbar\omega_0/2$. At thermal equilibrium under ordinary NMR conditions, the spin ensemble follows a Boltzmann distribution at temperature T, which leads to a slight excess of population in the ground state than the excited state, which amounts to a net bulk magnetization in the direction of the applied static field. Therefore the density matrix corresponding to the thermal equilibrium has no coherence (off-diagonal) elements, and population (diagonal) elements are given as follows [11]

$$\rho_{rr}^{eq} = \frac{e^{-E_r/k_BT}}{\sum_s e^{-E_s/k_BT}}, \tag{1.53}$$

where k_B is the Boltzmann constant and sum is over all the eigenstates of the Hamiltonian. In the high temperature limit $\hbar\omega_0 << k_BT$, ρ_{rr}^{eq} can be simplified using the following approximations

$$\begin{aligned} e^{-\hbar\omega_0/2k_BT} &\approxeq 1 - \frac{\hbar\omega_0}{2k_BT} \\ \sum_s e^{-\hbar\omega_s/k_BT} &= e^{-\hbar\omega_0/2k_BT} + e^{\hbar\omega_0/2k_BT} \approxeq 2. \end{aligned} \tag{1.54}$$

Therefore

$$\rho_{00}^{eq} \approxeq \frac{1}{2} + \frac{\hbar\gamma B_0}{4k_BT}$$
$$\rho_{11}^{eq} \approxeq \frac{1}{2} - \frac{\hbar\gamma B_0}{4k_BT}, \tag{1.55}$$

and the thermal equilibrium density matrix

$$\rho^{eq} = \begin{bmatrix} \frac{1}{2} + \frac{\epsilon}{2} & 0 \\ 0 & \frac{1}{2} - \frac{\epsilon}{2} \end{bmatrix}, \tag{1.56}$$

where $\epsilon = \hbar\gamma B_0/2k_BT$. In terms of Pauli-operators it can be written as

$$\rho^{eq} = \frac{1}{2}\mathbb{1} + \frac{\epsilon}{2}\sigma_z. \tag{1.57}$$

Intuitively, the above state contains a uniform background represented by $\mathbb{1}$ and tiny deviation part ($\epsilon \approx 10^{-5}$ under usual NMR conditions) in the state σ_z indicating highly mixed thermal equilibrium state since $\mathrm{Tr}[(\rho^{eq})^2] << 1$. Achieving pure states is not practical in NMR since it involves applying very high magnetic fields or extremely low temperatures. However, one can achieve *pseudo pure states* (PPS) which mimics the pure state behavior and can be written as follows

$$\rho_{PPS} = \left(\frac{1-\epsilon}{2}\right)\mathbb{1} + \epsilon|0\rangle\langle 0|. \tag{1.58}$$

A single qubit thermal state is naturally in a pseudo pure state. For multi-qubit systems, PPS can be prepared in many ways in NMR such as temporal averaging [37], spatial averaging [38], logical labeling [39], state initialization utilizing long-lived singlet states [40] and NMR line-selective pulses [41].

The net magnetization is proportional to the ratio of populations which can be written as follows

$$\rho_{00}^{eq}/\rho_{11}^{eq} = \exp(\hbar\omega_0/k_BT) \simeq 1 + \frac{\hbar\omega_0}{k_BT} \tag{1.59}$$

with the high temperature approximation. The ratio is almost close unity as $\hbar\omega_0/k_BT \sim 10^{-5}$ which makes the ensemble weakly paramagnetic as only 1 magnetic moment in 10^5 is aligned in the direction of external field. Nevertheless this slight population imbalance is detectable and

gives observable magnetization in z-direction given by [11, 42]

$$M_z = \frac{\mu_0 \gamma^2 \hbar^2 B_0}{4 k_B T}, \tag{1.60}$$

where μ_0 is magnetic susceptibility.

1.3.1.3 Internal Interactions among nuclei: multiple qubits

In order to make a quantum register, one needs multiple spins that interact with each other. A pair of nuclei can exhibit interactions governed by Hamiltonian containing bilinear terms [10, 11]. These interactions can be of two types

(i) Electron mediated indirect interactions

(ii) Direct dipole-dipole interactions

For the case dealt in this thesis, namely, *isotropic liquid*, the direct dipole-dipole interactions average out to zero due to the fast tumbling motion of the spins [11]. However, indirect coupling also known as J- coupling survives and corresponds to Hamiltonian given by (assuming $\hbar = 1$)

$$H_{\text{int}} = \sum_i \omega_{0i} I_{zi} + 2\pi \sum_{i<j} J_{ij} I_i \cdot I_j, \tag{1.61}$$

with indirect spin-spin J-coupling J_{ij}. Here $I_{\alpha i} = \sigma_{\alpha i}/2$ are spin operators for the i^{th} spin, where $\alpha \in x, y, z$ and $I_i \cdot I_j = \sum_\alpha I_{\alpha i} I_{\alpha j}$. In the weak coupling limit $|J_{ij}| << |\omega_{0i} - \omega_{0j}|$, the Hamiltonian can be further simplified to

$$H_{\text{int}} = \sum_i \omega_{0i} I_{zi} + 2\pi \sum_{i<j} J_{ij} I_{zi}\, I_{zj}. \tag{1.62}$$

Note that, in the case of heteronuclear spins, this approximation is always satisfied since the Larmor frequency difference typically falls in the MHz range, and J-coupling constants are in Hz. For a two-qubit system the above Hamiltonian has four eigenstates which form the basis $\{|00\rangle, |01\rangle, |10\rangle, |11\rangle\}$. The eigenvalues corresponding to basis states are:

$$
\begin{aligned}
|00\rangle &\rightarrow (\omega_{01} + \omega_{02} + \pi J)/2 \\
|01\rangle &\rightarrow (\omega_{01} - \omega_{02} - \pi J)/2 \\
|00\rangle &\rightarrow (-\omega_{01} + \omega_{02} - \pi J)/2 \\
|00\rangle &\rightarrow (-\omega_{01} - \omega_{02} + \pi J)/2.
\end{aligned} \tag{1.63}
$$

1.3.2 NMR quantum gates

1.3.2.1 External Interactions with radio frequency (RF) fields

As pointed out earlier, Larmor frequency in NMR is the order of hundreds of MHz; hence, the suitable electromagnetic field required to manipulate the state of the qubit fall in RF range. Consider a linearly polarized RF field $2B_1 \cos(\omega_{\mathrm{RF}} t + \phi)\hat{x}$ with frequency ω_{RF} and phase ϕ. The Hamiltonian can be written as (assume $\hbar = 1$)

$$
H_{\mathrm{RF}}(t) = -\gamma I_x \{2B_1 \cos(\omega_{\mathrm{RF}} t + \phi)\} = 2\omega_1 I_x \cos(\omega_{\mathrm{RF}} t + \phi), \tag{1.64}
$$

where $\omega_1 = -\gamma B_1$ is effective RF amplitude. The resonance condition is achieved when $\omega_{\mathrm{RF}} = \omega_0$. Otherwise the difference between the two is called *offset*. The linear polarized RF field can be decomposed into left (B_l) and right (B_r) circularly polarized RF fields

$$
\begin{aligned}
B_l(t) &= B_1[\cos(\omega_{\mathrm{RF}} t + \phi)\hat{x} - \sin(\omega_{\mathrm{RF}} t + \phi)\hat{y}] \\
B_r(t) &= B_1[\cos(\omega_{\mathrm{RF}} t + \phi)\hat{x} + \sin(\omega_{\mathrm{RF}} t + \phi)\hat{y}].
\end{aligned} \tag{1.65}
$$

At resonance ($\omega_{\mathrm{RF}} = \omega_0$), $B_r(t)$ and $B_l(t)$, respectively, represent field rotating in the same and opposite direction w.r.t precession of the nuclei. In the frame rotating with nuclear Larmor frequency, the field $B_r(t)$ is stationary and $B_l(t)$ rotates with twice the Larmor frequency. Hence, in the high field approximation, only $B_r(t)$ has effect on the dynamics of the nuclei.

Now in the rotating frame of ω_{RF},

$$
B_r' = B_1[\cos\phi\hat{x} + \sin\phi\hat{y}]. \tag{1.66}
$$

In the off resonant case with offset $\omega_0 - \omega_{\rm RF} = \Omega$, an effective field can be defined

$$B_{\rm eff} = \frac{\Omega}{\gamma}\hat{z} + \frac{\omega_1}{\gamma}[\cos\phi\hat{x} + \sin\phi\hat{y}] \tag{1.67}$$

and accordingly

$$H_{\rm eff} = \Omega I_z + \omega_1[\cos\phi I_x + \sin\phi I_y]. \tag{1.68}$$

Therefore, using propagator $U = \exp(-iH_{\rm eff}t)$, the desired evolution of the state of the nuclear spin ensemble can be achieved by careful tuning of RF amplitude and exposure time. Often RF fields are applied in short bursts with high power ($\sim$kHz), called RF pulse. An RF pulse achieving an angle $\theta = \omega t_p$ can be applied using RF amplitude ω_1 for time t_p. For example, a $\pi/2$ rotation, which equilibrates the populations and creates coherences starting from the thermal equilibrium state, can be achieved using 25 kHz RF amplitude for a 10 μs duration. We will denote a pulse of angle θ about ϕ axis by $(\theta)_\phi$.

1.3.2.2 Quantum gates using RF fields

Single qubit gates are simply rotation on the Bloch sphere, and any rotation can be applied using a combination of RF pulses.

X or NOT gate

The X gate which flips the state $|0\rangle \leftrightarrow |1\rangle$ can be realized by a $(\pi)_x$ pulse

$$\pi_x = e^{-i\pi\sigma_x/2} = -i\begin{bmatrix} 0 & 1 \\ 1 & 0 \end{bmatrix}, \tag{1.69}$$

where $-i$ factor can be ignored as it introduces an unobservable global phase.

Hadamard gate

The Hadamard gate which creates equal superposition $\frac{|0\rangle+|1\rangle}{\sqrt{2}}$ starting from $|0\rangle$ can be realized by combination of $(\pi)_x$ and $(\pi/2)_y$ pulse

$$[(\pi/2)_y - (\pi)_x] = e^{-i\pi\sigma_y/4}e^{-i\pi\sigma_x/2} = -\frac{i}{\sqrt{2}}\begin{bmatrix} 1 & 1 \\ 1 & -1 \end{bmatrix}, \tag{1.70}$$

where the factor $-i$ can be ignored. Often a pseudo Hadamard gate is used instead of Hadamard gate

$$[(\pi/2)_{-y}] = e^{i\pi\sigma_y/4} = \frac{1}{\sqrt{2}}\begin{bmatrix} 1 & 1 \\ -1 & 1 \end{bmatrix}. \tag{1.71}$$

Controlled-NOT (CNOT) gate

Multi-qubit gates can be realized using a combination of RF pulses and evolution under indirect coupling Hamiltonian given in Eq. 1.62. An NMR pulse sequence to realize a CNOT gate with the first qubit as control and second qubit as the target can be following

$$\left[\left(\frac{\pi}{2}\right)^{2}_{-y} - \left(\frac{\pi}{2}\right)^{1,2}_{-z} - \tau - (\pi)^{1,2}_{y} - \tau - (\pi)^{1}_{y} - \left(\frac{\pi}{2}\right)^{2}_{-y}\right] = -(1+i)\begin{bmatrix} 1 & 0 & 0 & 0 \\ 0 & 1 & 0 & 0 \\ 0 & 0 & 0 & 1 \\ 0 & 0 & 1 & 0 \end{bmatrix}, \tag{1.72}$$

where $\tau = 1/(4J)$ is the duration of evolution under coupling Hamiltonian given in Eq. 1.62.

1.3.2.3 Numerically optimized pulses

Sometimes it is very non-trivial to find an appropriate combination of RF pulses and coupling evolutions to realize a generic unitary operator. In these scenarios, one resort to numerically designed RF modulations. For an on-resonant RF field, we can write total Hamiltonian

$$H_{\text{tot}} = \omega_1(t)[\cos\phi(t)I_x + \sin\phi(t)I_y] + H_{\text{int}}, \tag{1.73}$$

where $\omega_1(t)$ and $\phi(t)$ are amplitude and phase of the RF field, respectively. So the goal boils down to find modulation profiles of $\omega_1(t)$ and $\phi(t)$ in such a manner that we achieve a target unitary operator U_{targ} by maximizing a cost function called fidelity [43]

$$F = |\text{Tr}[U^{\dagger}_{\text{targ}}U_{\text{opt}}]/N|^2, \tag{1.74}$$

where U_{opt} is the numerically optimized unitary operator. The optimization tries to maximize F and stops when an acceptable value is achieved. In some instances, the unitary operator required to attain final state ρ_{targ} is not known. In these cases, the definition of fidelity can be changed

accordingly [43]

$$F = \frac{\mathrm{Tr}[\rho_{\mathrm{targ}}\ \rho_{\mathrm{opt}}]}{\sqrt{\mathrm{Tr}[\rho_{\mathrm{targ}}^2]\ \mathrm{Tr}[\rho_{\mathrm{opt}}^2]}}, \tag{1.75}$$

where ρ_{opt} is optimized state. Various algorithms have been developed to numerically optimize the pulse sequence, e.g, stochastic search methods [43], GRadient Ascend Pulse Engineering (GRAPE) [44] and bang-bang (BB) optimal control [45, 46] to name a few. Also, these algorithms can be appropriately equipped for robust optimization, i.e., to achieve high fidelity even in the presence of radio-frequency inhomogeneity (RFI). In the next chapter, we utilize BB control to control an 11 spin system.

1.3.3 Measurement in NMR

As pointed out earlier, NMR qubits are ensembles of spin-1/2 isotopes. A typical NMR liquid state ensemble with volume $\sim\ 500\mu$l consists of $\sim\ 10^{18}$ spins. At thermal equilibrium, the ensemble follows Boltzmann distribution giving rise to net magnetization along the direction of the static magnetic field applied in z-direction. This net magnetization is rotated to the transverse plane via a $(\pi/2)$ RF pulse. Now the net transverse magnetization starts precessing around the static magnetic field, giving rise to a measurable electromagnetic flux called *Free induction decay* (FID). FID is an oscillating function with a decay envelope due to various relaxation processes in NMR (described in the next section), and one can obtain frequency domain profiles via discrete Fourier transform. In NMR, the FID is measured in a rotating frame with rotation frequency termed as *reciever frequency*. The offset between receiver frequency and Larmor frequency can be both positive and negative. Now to distinguish the positive and negative offsets, FID along both x and y axis is measured, which is called *quadrature detection*.

In the case of an ensemble, the measurement of a quantity corresponding to observable D is its expectation value, as described in section 1.1.4.2.

$$\langle D\rangle_t = \mathrm{Tr}[D\ \rho(t)], \tag{1.76}$$

where $\rho(t)$ is the density matrix of the ensemble at time t. In NMR, due to quadrature detection, the effective observable D is of the form $\sigma_x + i\sigma_y$ which corresponds to the sum of measurement of net magnetization along both x and y directions.

In general, for a non-equilibrium state, only single quantum coherence elements of density

matrix can be observed using the above detection operator [10, 11]. To measure all the elements of a density matrix, one has to resort to a technique called *quantum state tomography* [47, 48].

1.4 Noise in NMR quantum systems: Relaxations

As described in the section 1.2 that a quantum system is never isolated but invariably interacts with the surrounding environment, NMR spin ensemble also interacts with the surroundings which lead to decay of population and coherence elements, called relaxation [10, 11, 36]. Using semiclassical approximation, the environment can be modeled as a stochastic field at the site of the nuclei. For spin-1/2 nuclei in isotropic liquid, the local stochastic fields can be due to various processes. Two major processes are following [11]

(i) *Dipole-dipole relaxation*- Magnitude and direction of the local magnetic field exerted by one spin on another spin due to direct dipole-dipole interaction become random as the molecule tumbles.

(ii) *Chemical shift anisotropy* (CSA): Magnitude and the direction of the local magnetic field caused by molecular electron currents becomes random as the molecule tumbles.

CSA is much weaker than Dipole-dipole relaxation but becomes comparable at higher magnetic fields. We can model the stochastic local field with a Gaussian random variable $\beta(t)$ with zero mean and autocorrelation function

$$g(\tau) = \langle \beta(t)\beta(t+\tau) \rangle, \tag{1.77}$$

where $\langle \ \ \rangle$ denotes the average over many realization of stochastic variable $\beta(t)$. The Fourier transform of $g(\tau)$ is called *noise spectrum* $S(\omega)$ which records the amount of noise present at various frequencies. Depending upon the frequency component, the following two types of relaxation processes can take place.

1.4.1 Longitudinal relaxation

The transverse frequency components around Larmor frequency are responsible for longitudinal relaxation. They introduce random transitions as well as relative phases between energy levels, which leads to the destruction of coherences and redistribution of populations towards thermal

equilibrium on a timescale often termed as T_1 [10, 11, 36]. It is essentially the recovery of net longitudinal magnetization given by the expectation value of $\sigma_z/2$ operator denoted as M_z. This relaxation mechanism can be described by the phenomenological differential equation given by Bloch [49]

$$\frac{dM_z(t)}{dt} = \frac{M_{z,eq} - M_z(t)}{T_1}, \tag{1.78}$$

where $M_{z,eq}$ is equilibrium longitudinal magnetization. It leads to following solution

$$M_z(t) = M_z(0)e^{-t/T_1} + M_{z,eq}(1 - e^{-t/T_1}). \tag{1.79}$$

1.4.2 Transverse relaxation

This type of relaxation occurs due to longitudinal low-frequency components compared to Larmor frequency. Though these components can not induce transition, they introduce random relative phases between energy levels. Consequently, this is an energy-conserving process and only leads to decay of coherences while populations remain unaltered on a timescale often termed as T_2 [10]. Similar to longitudinal magnetization, this relaxation mechanism can be described by the phenomenological differential equation given by Bloch [49]

$$\frac{dM_{xy}(t)}{dt} = -\frac{M_{xy}(t)}{T_2}, \tag{1.80}$$

where $M_{xy}(0)$ is initial longitudinal magnetization. It leads to the following solution

$$M_{xy}(t) = M_{xy}(0)e^{-t/T_2}. \tag{1.81}$$

The exact value of T_1 and T_2 depends upon the state of matter (solid or liquid or liquid crystals), solvent, temperature, concentration, external magnetic field, etc. [11]. In general $T_2 \leq T_1$. Note that in many cases, a simple semiclassical approximation may not be valid, and one has to resort to the more elaborate mechanisms [42].

CHAPTER 2

Enhancement of long-lived singlet-order using optimal control

Abstract

Using a bang-bang optimal control technique, we transfer polarization from a set of abundant high-γ nuclei directly to singlet order of a low-γ spin-pair. This approach is analogous to algorithmic cooling (AC) procedure used in quantum state purification. Specifically, we apply this method for enhancing the singlet order in a natural abundant ^{13}C- ^{13}C spin pair by exploiting nine equivalent protons of an 11-spin system. Compared to the standard method not involving polarization transfer, we find an enhancement of singlet order by about 3.4 times. In addition, since the singlet magnetization is contributed by the faster relaxing protons, the recycle delay is halved. Thus effectively we observe a reduction in the overall experimental time by a factor of 23. We also discuss a possible extension of AC, known as heat-bath algorithmic cooling (HBAC).

Reported in

Deepak Khurana, and T. S. Mahesh, *Bang-bang optimal control of large spin systems: Enhancement of ^{13}C- ^{13}C singlet-order at natural abundance,* Journal of Magnetic Resonance 284, 8-14 (2017).

2.1 Introduction

Not many experimental architectures allow as elaborate control of quantum dynamics as that of NMR. Several powerful RF control techniques such as composite pulses [50], adiabatic pulses [51], band-selective/broadband pulses [52–55] are being routinely used in NMR spectroscopy. Numerical methods such as strongly modulating pulses [43], GRadient Ascent Pulse Engineering (GRAPE) [44, 56], and Krotov [57–61] have also been used for specific purposes in spectroscopy as well as quantum information. Here we describe an application of bang-bang (BB) optimal control that utilizes a sequence of full power radio frequency (RF) pulses with variable phases

separated by variable delays [45, 46, 62]. Generally, the numerical complexity of optimal control techniques scales rapidly with the size of the spin system, thus limiting their applications. In this regard improvements in optimal control techniques such as restricted state space approximation [63, 64] and matrix recycling [65] have been suggested to control large spin systems. Adding to this toolkit, BB relies on one-time matrix exponentiation to build basic unitaries and hence it's complexity scales much slower, and therefore is applicable also for fairly larger spin systems [45]. In this work, we utilize the BB control to directly transfer polarization from a set of ancillary spins to the long-lived singlet-order in a spin-pair.

2.2 Long-lived singlet order (LLS)

Right after its conception in NMR, LLS has gained significant theoretical and experimental interest [66–84] due to its wide range of applications such as study of slow molecular processes [85], characterizing molecular diffusion [86, 87], precision measurement of scalar couplings [88], obtaining molecular structure information [89], and storage of hyper polarization [90–95].

In a pair of two-level quantum particles with individual basis states $\{|\uparrow\rangle, |\downarrow\rangle\}$, antisymmetric singlet state is

$$|S_0\rangle = \frac{|\uparrow\downarrow\rangle - |\downarrow\uparrow\rangle}{\sqrt{2}} \tag{2.1}$$

and symmetric triplet states are

$$\begin{aligned} |T_0\rangle &= \frac{|\uparrow\downarrow\rangle + |\downarrow\uparrow\rangle}{\sqrt{2}} \\ |T_+\rangle &= |\uparrow\uparrow\rangle \text{ and,} \\ |T_-\rangle &= |\downarrow\downarrow\rangle. \end{aligned} \tag{2.2}$$

For a single spin system (with gyromagnetic ratio γ and spin operators $I_\alpha = \sigma_\alpha/2$, where $\alpha \in x, y, z$), the density operator corresponding to thermal equilibrium state under high magnetic-field (B_0) and high-temperature (T) approximation is given by $\rho = \mathbb{1}/2 + \epsilon I_z$, where $\epsilon = \hbar\gamma B_0/(2k_B T)$, with $\hbar$ being the reduced Planck's constant and k_B being the Boltzmann constant. Typically in NMR, the polarization factor $\epsilon \sim 10^{-5}$ and it represents the excess population in the ground state over the excited state. Similarly, in the case of a two-spin system, an excess

population of singlet state is represented by the density operator

$$\rho_S = (1 - \epsilon_S)\mathbb{1}_4/4 + \epsilon_S |S_0\rangle\langle S_0|, \tag{2.3}$$

where $\mathbb{1}_4$ is the four-dimensional identity operator and the scalar quantity ϵ_S quantifies the singlet-order [71]. Since the dominant intra-pair dipolar relaxation process does not connect subspaces of different symmetries, the singlet-order often lives much longer than other non-equilibrium states whose lifetimes are limited by the spin-lattice relaxation time constant T_1 [69, 70, 96]. In favorable cases, singlet life-times as long as over 50 times T_1 have also been observed [80, 97].

One way to access singlet-order is to utilize the chemical shift separation (along with J-coupling) between two spins to prepare a mixture $|S_0\rangle\langle S_0| - |T_0\rangle\langle T_0|$ of singlet and triplet states. This preparation is followed by suppression of chemical shift to impose symmetry, achieved either with low-field switching by shuttling the sample out of the magnet [66], or with a strong RF spin-lock while retaining the high-field [68]. After the desired storage period, the chemical shift separation is restored, and the singlet-order is converted back into observable single quantum coherence.

Later, a method was discovered to access singlet-order in systems with chemical equivalence, but magnetic inequivalence w.r.t. a chemically equivalent ancillary spin-pair [75]. In this case, each of the chemically equivalent spin-pairs exists in singlet states at high magnetic fields without requiring external spin-lock to impose symmetry. It was also shown that by exploiting the higher sensitivity of ancillary ^{1}H-^{1}H spin-pair, one can prepare, store, and detect ^{13}C-^{13}C singlet order either with isotopic labeling [98] or even at natural abundance [99].

In this chapter, it is shown that using the BB optimal control techniques; we can directly transfer polarization from ancillary protons to enhance naturally abundant ^{13}C-^{13}C singlet order. This method is widely applicable in a variety of systems where a pair of spins with or without chemical equivalence are coupled to a few ancillary spins.

Although the concept of polarization transfer has long been a part of NMR spectroscopy [100–102], it has been revisited in quantum information while attempting to achieve a small set of highly pure quantum bits (system qubits) at the expense of purity of a large number of ancillary quantum bits (reset qubits). This process is known as algorithmic cooling (AC), and it systematically transfers entropy from system qubits to reset qubits [103, 104]. Motivated by

these concepts, we refer to the single iteration polarization transfer as AC. Heat bath algorithmic cooling (HBAC) is a nonunitary extension of AC, which involves disposal of the extra entropy from the reset qubits to an external bath so that AC can be iteratively applied to achieve higher purity of system qubits [105].

The chapter is organized as follows: In the next section, I describe BB optimal control in detail. In section 2.4 and 2.5, I describe our spin system and pulse sequence, respectively. In section 2.6, I describe experimental results and simulations. Finally, section 2.7 contains discussions and conclusions.

2.3 Bang-bang (BB) optimal control

Consider a system in a state ρ_{in} that needs to be steered to a target state ρ. We discretize the time evolution into N segments each of duration Δt. In the rotating-frames of the RF carriers, let $\mathcal{H}_0$ be the internal Hamiltonian of the system and

$$\begin{aligned} \mathcal{H}_{k,n} &= A_{k,n}\left(I_x^k \cos\phi_{k,n} + I_y^k \sin\phi_{k,n}\right) \\ &= A_{k,n} Z_{k,n} I_x^k Z_{k,n}^\dagger \end{aligned} \tag{2.4}$$

be the RF Hamiltonian on k^{th} channel and n^{th} segment. Here $A_{k,n},\ \phi_{k,n}$ are the amplitudes and phases respectively, $Z_{k,n} = \exp(-i\phi_{k,n} I_z^k)$, and $I_x^k = \sum_i I_{ix}^k$, $I_y^k = \sum_i I_{iy}^k$, $I_z^k = \sum_i I_{iz}^k$ are the sums of spin operators of all the spins of the k^{th} nuclear species. The full piecewise constant Hamiltonian

$$\mathcal{H}_n = \mathcal{H}_0 + \sum_k \mathcal{H}_{k,n} \tag{2.5}$$

achieves an effective unitary evolution $U = \prod_{n=N}^{1} e^{-i\mathcal{H}_n \Delta t}$.

In this work, we try to find a unitary operator U that prepares the target state

$$\begin{aligned} \rho(0) &= U\rho_{\text{in}}U^\dagger \\ &= \{1 - \epsilon_S(0) - \epsilon_\Delta\}\frac{\mathbb{1}_4}{4} + \epsilon_S(0)|S_0\rangle\langle S_0| + \epsilon_\Delta\rho_\Delta, \end{aligned} \tag{2.6}$$

containing a long-lived singlet component $|S_0\rangle\langle S_0|$ with a maximum singlet-order $\epsilon_S(0)$. Here ρ_Δ is an undesired, though unavoidable, component containing triplet states as well as other artifact

coherences. The expectation value of the singlet component $|S_0\rangle\langle S_0|$ in $\rho(0)$ is

$$Q = \mathrm{Tr}\left[\rho(0)\ |S_0\rangle\langle S_0|\right] \approx \frac{3\epsilon_S(0)+1}{4}. \tag{2.7}$$

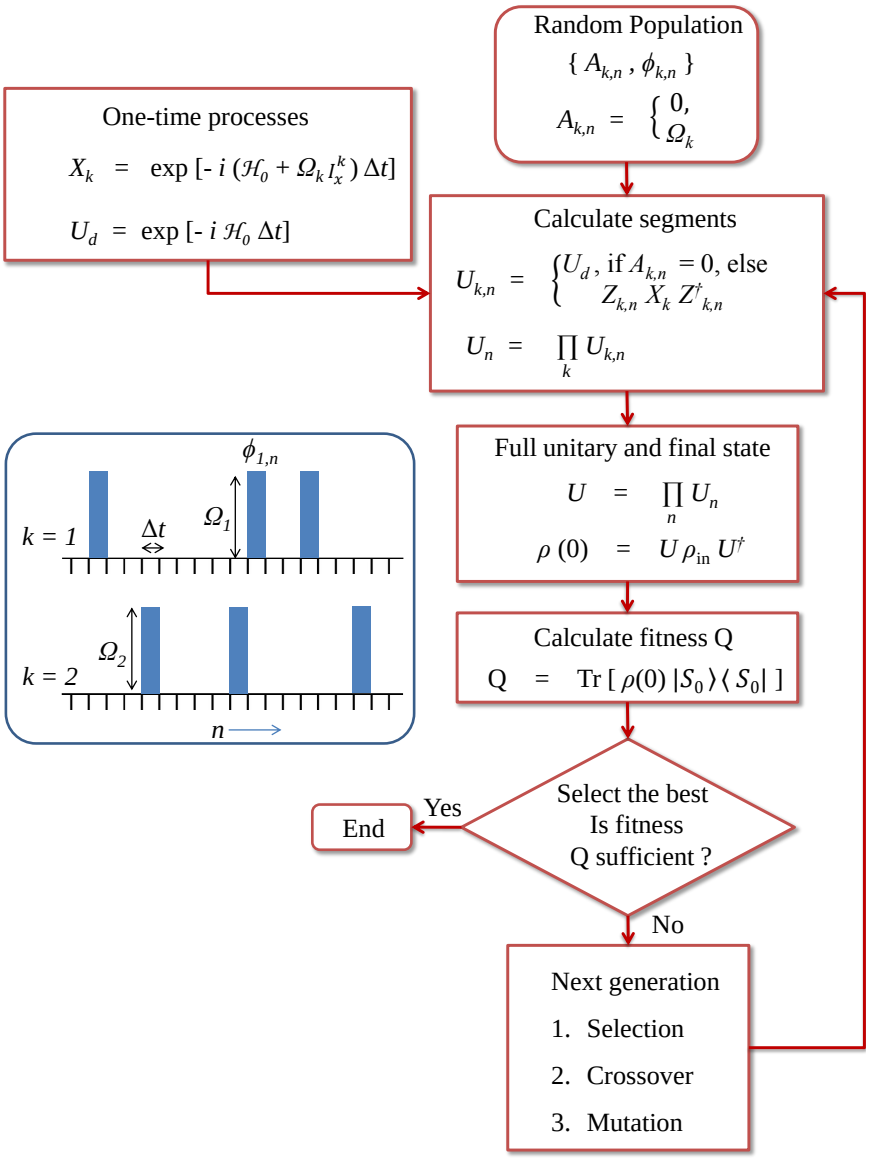

Figure 2.1: The flowchart describing BB optimal control with genetic algorithm. A schematic diagram of BB control is shown in the inset, wherein each rectangular box corresponds to a full power RF pulse, called a *bang*.

Therefore by maximizing Q via BB control, we can obtain an unitary operator preparing a maximum singlet-order. A subsequent spin-lock of duration τ rapidly damps out the short-lived

component ρ_Δ towards the maximally mixed state $\mathbb{1}_4/4$, such that the purified state is of the form

$$\rho(\tau) = \{1 - \epsilon_S(\tau)\}\, \mathbb{1}_4/4 + \epsilon_S(\tau)|S_0\rangle\langle S_0|, \tag{2.8}$$

where $\epsilon_S(\tau) = \epsilon_S(0)e^{-\tau/T_S}$ is the singlet-order decayed due to the long singlet life-time T_S. In the next section we use AC to enhance the singlet-order from ϵ_S to $\epsilon_S^{\mathrm{BBAC}}$ by polarization transfer from ancillary spins using BB control.

As opposed to schemes based on smooth RF modulations, BB control employs pulses having either zero or full RF amplitudes ($A_{k,n} = \Omega_k$ or 0) but variable phases ($\phi_{k,n}$) to generate arbitrary unitaries. A flowchart describing various steps of the BB optimal control using genetic algorithm is shown in Fig. 2.1. Here the delay propagator $U_d = \exp\left[-i\mathcal{H}_0\Delta t\right]$ and basic propagator for the kth species $X_k = \exp\left[-i\left(\mathcal{H}_0 + \Omega_k I_x^k\right)\Delta t\right]$ are calculated once outside the optimization loop. In general, it is possible to realize a phase-shifted bang operator by simply rotating the basic operator, i.e.,

$$\begin{aligned} U_{k,n} &= \exp\left[-i\left(\mathcal{H}_0 + \Omega_k Z_{k,n} I_x^k Z_{k,n}^\dagger\right)\Delta t\right] \\ &= Z_{k,n} X_k Z_{k,n}^\dagger, \end{aligned} \tag{2.9}$$

provided $[\mathcal{H}_0, I_z^k] = 0$. This condition holds for Zeeman, J-coupling, Dipolar coupling, as well as for quadrupolar Hamiltonians. Here $Z_{k,n}$ is a diagonal operator in Zeeman basis and hence is efficiently computed during the run-time of iterations. RF inhomogeneity can also be accounted by a one time preparation of a set of basic propagators corresponding to different RF amplitudes.

Thus, the major advantage of BB control is that the exponentiation of Hamiltonian to obtain the basic unitary operator (X_k) as well as the delay unitary operator (U_d) is rendered a one-time process that is outside of the iterations. Matrix exponentiation is a bottleneck in conventional algorithms based on amplitude modulation, particularly for large spin systems. Often it might be possible to employ efficient state evaluations such as Krylov exponentiation algorithm [106] for large sparse matrices to speed up optimization. On the other hand, BB protocol relies on the one-time calculation of the basic propagators and efficient generation of phase modulated bang operators. As a result, BB method allows quantum control of large spin systems as demonstrated in the later section. It is even more efficient in designing RF sequences with low duty-cycle requiring long evolutions of internal Hamiltonian such as polarization transfer operations.

2.4 NMR Spin System

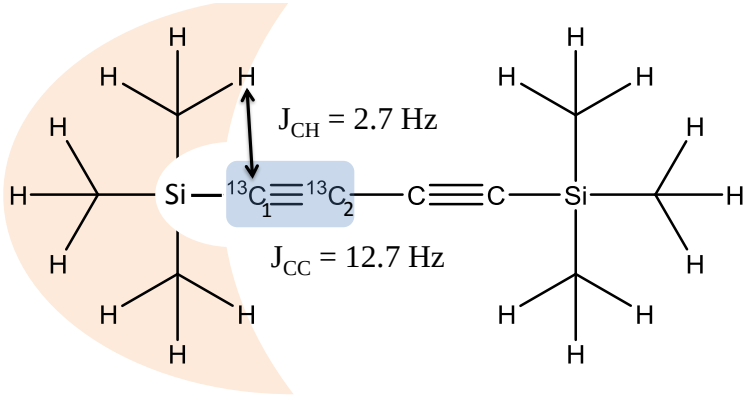

Figure 2.2: Structure of $1,4$-Bis (trimethylsilyl) butadiyne. Here protons in the shaded area act as ancillary spins which provide polarization to ^{13}C-^{13}C singlet-order.

To demonstrate enhancement of singlet-order, we use an 11-spin system including a pair of naturally abundant, weakly-coupled ^{13}C spins surrounded by nine chemically equivalent ^{1}H spins of $1,4$-Bis (trimethylsilyl) butadiyne (BTMSB). The sample was prepared by dissolving 120 mg of BTMSB in 0.7 ml of $CDCl_3$ (0.88 M). We use the protons to directly prepare enhanced ^{13}C-^{13}C singlet-order. The molecular structure of BTMSB is shown in Fig. 2.2. The molecular symmetry provides twice the probability of naturally abundant ^{13}C-^{13}C pairs. The chemical shift difference between the two ^{13}C spins is 2.32 ppm, and the $^{13}C_1$-$^{13}C_2$ J-coupling constant is 12.7 Hz, while J-coupling between $^{13}C_1$ and the closest equivalent protons is 2.7 Hz. The spin-lattice relaxation time constants (T_1) are about 3 s, 6.5 s, and 8.2 s for ^{1}H, $^{13}C_1$ and $^{13}C_2$ respectively. The effective transverse relaxation time constants (T_2^*) are, respectively, 0.3 s, 2.5 s, and 2.9 s.

2.5 NMR Pulse sequence

The pulse sequence employed for the preparation and enhancement of ^{13}C-^{13}C singlet-order is shown in Fig 2.3. The initial thermal equilibrium state of the system is

$$\rho_0 = \frac{\mathbb{1}_2^{\otimes 11}}{2^{11}} + \epsilon_{\mathrm{C}} \left(I_z^{\mathrm{C}_1} + I_z^{\mathrm{C}_2} \right) + \epsilon_{\mathrm{H}} \sum_{j=1}^{9} I_z^{\mathrm{H}_j} \tag{2.10}$$

where ϵ_{C} and ϵ_{H} are the carbon and proton polarizations respectively, and $\epsilon_{\mathrm{H}}/\epsilon_{\mathrm{C}} = \gamma_{\mathrm{H}}/\gamma_{\mathrm{C}} \simeq 4$.

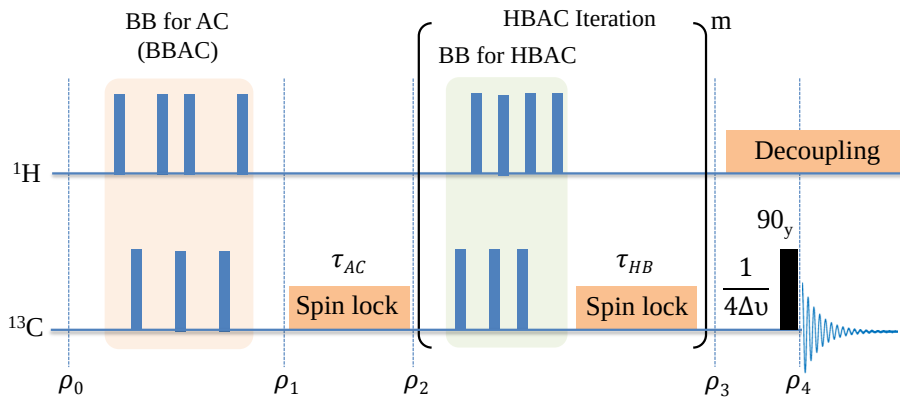

Figure 2.3: Pulse sequence for the preparation and enhancement of ^{13}C-^{13}C singlet-order using ^{1}H spins. Here m can take integral values $0, 1, 2, \cdots$ etc.

Then a BBAC singlet sequence is applied to prepare ^{13}C-^{13}C singlet-order. Thus the reduced density operator for carbon spins is now

$$\rho_1 = \left[1 - \epsilon_S^{\mathrm{BBAC}}(0) - \epsilon_\Delta\right] \frac{\mathbb{1}_4}{4} + \epsilon_S^{\mathrm{BBAC}}(0)|S_0\rangle\langle S_0| + \epsilon_\Delta \rho_\Delta, \tag{2.11}$$

where $\epsilon_S^{\mathrm{BBAC}}(0)$ represents the enhanced singlet-order. At the end of the spin-lock of duration τ_{AC}, one obtains a high quality singlet state

$$\rho_2 = \left[1 - \epsilon_S^{\mathrm{BBAC}}(\tau_{\mathrm{AC}})\right] \frac{\mathbb{1}_4}{4} + \epsilon_S^{\mathrm{BBAC}}(\tau_{\mathrm{AC}})|S_0\rangle\langle S_0|, \tag{2.12}$$

with the singlet-order $\epsilon_S^{\mathrm{BBAC}}(\tau_{\mathrm{AC}})$.

Suppose ^{1}H spins have much shorter T_1 relaxation time constant compared to the life time of singlet-order (T_S). Then during the spin-lock duration, ^{1}H spins regain polarization by spin-lattice relaxation and are available for further polarization transfer to ^{13}C-^{13}C singlet-order. In our pulse sequence this is achieved by another BB pulse. This process (Fig. 2.3) known as HBAC can be iterated to further enhance the singlet-order in favorable systems. At the end of m HBAC iterations we obtain the state

$$\rho_3 = \left[1 - \epsilon_S^{\mathrm{HB}_m}(\tau_{\mathrm{HB}})\right] \frac{\mathbb{1}_4}{4} + \epsilon_S^{\mathrm{HB}_m}(\tau_{\mathrm{HB}})|S_0\rangle\langle S_0|, \tag{2.13}$$

where $\epsilon_S^{\mathrm{HB}_m}(\tau_{\mathrm{HB}})$ is the singlet-order after the final spin-lock of duration τ_{HB}.

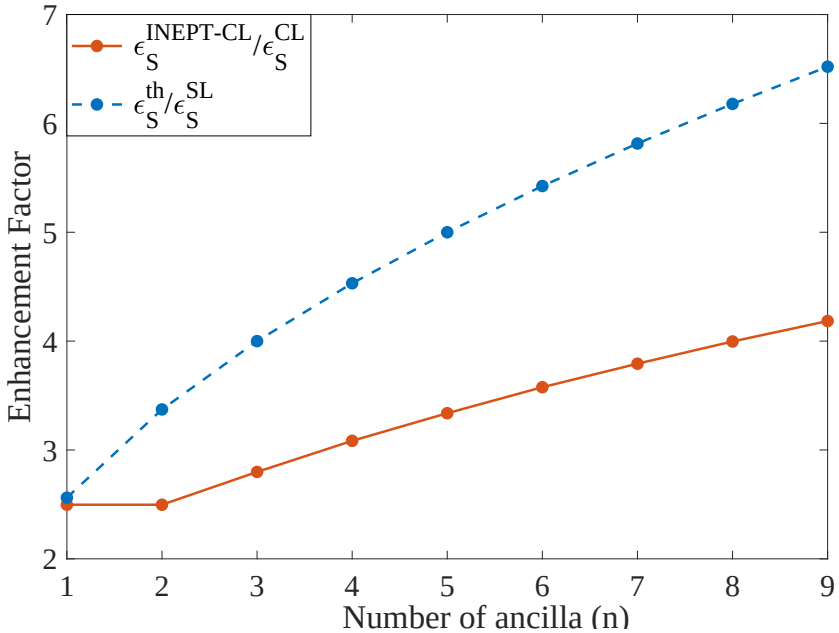

Figure 2.4: Comparison between entropically achievable singlet-order enhancement and that achievable using INEPT-CL singlet sequence versus number of ancilla in star-topology systems. Here $\gamma_X/\gamma_A = \gamma_X/\gamma_M = 4$ is assumed.

Finally, we convert the singlet-order into,

$$\rho_4 = \frac{\mathbb{1}_4}{4} - \epsilon_S^{\text{HB}_m}(\tau_{\text{HB}}) \left(I_z^{\text{C}_1} I_y^{\text{C}_2} - I_y^{\text{C}_1} I_z^{\text{C}_2} + I_x^{\text{C}_1} I_x^{\text{C}_2} \right), \tag{2.14}$$

where zy and yz terms form the observable single quantum coherences of ^{13}C spins.

2.6 Enhancing LLS

2.6.1 Bounds on achievable singlet-order

Consider a $X_n AM$ type of spin-system where only spin A is coupled to magnetically equivalent X spins. Entropic calculations suggest an upper bound for the polarization transfer from X spins to A spins by a factor of $\alpha = \sqrt{\gamma_A^2 + n\gamma_X^2}/\gamma_A$, where γ_X and γ_A are gyromagnetic ratios of X and A spins respectively [102, 107]. If Carravetta-Levitt (CL) singlet sequence [68] is applied on polarization enhanced A spin and thermally polarized M spin while decoupling X spins, a enhancement factor of $\epsilon_S^{th} = (\alpha+1)/2$ can be achieved for singlet-order. However in practice the achieved enhancement factor is smaller than the entropic value. Fig. 2.4 shows the singlet-order enhancement factor with entropic α values and with that achievable by INEPT-CL (refocused

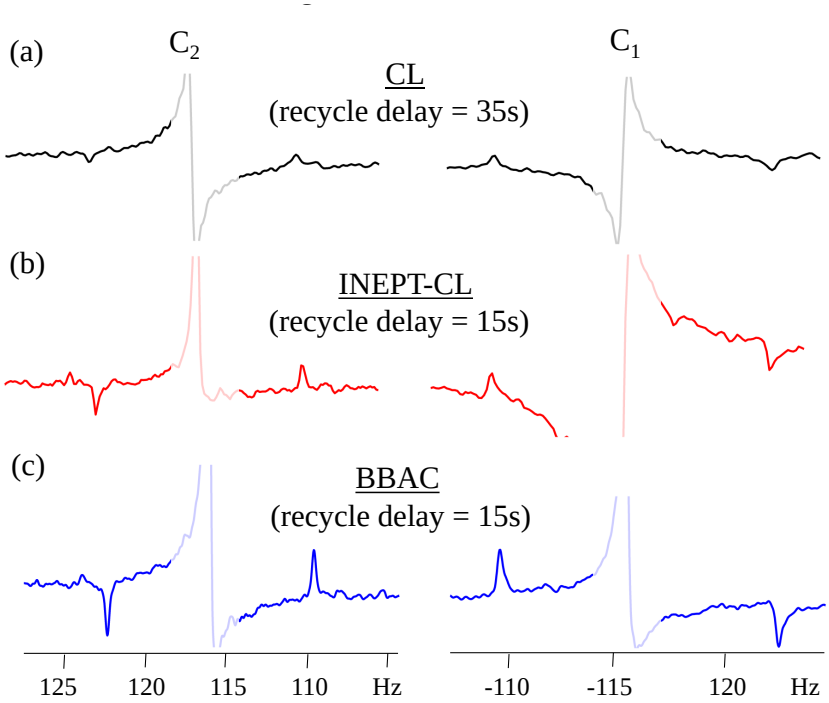

Figure 2.5: ^{13}C spectra of BTMSB obtained by converting ^{13}C-^{13}C singlet-order at natural abundance into single-quantum coherence using: (a) only CL, (b) INEPT-CL, and (c) BBAC singlet sequences. All spectra were recorded with WALTZ-16 spin-lock (1.5 kHz, $\tau_{\mathrm{AC}} = 10$ s). The central peaks corresponding to ^{13}C-^{12}C pairs are de-emphasized.

INEPT [10] folowed by CL sequence) for $\gamma_X/\gamma_A = \gamma_X/\gamma_M = 4$.

2.6.2 Experimental results and numerical analysis

We implemented the algorithm described in section 2.1 in MATLAB [45]. We used the genetic algorithm for 5000 generations with a population size of 100. While it is hard to judge the global optimality, we selected the best out of many solutions obtained. For AC, the best solution was of total duration 296 ms and consisted 592 segments each of 500 µs duration. For HBAC, the solution was of duration 248.5 ms and consisted 497 segments.

All experiments were performed using a 9.4 T (400 MHz) Bruker NMR spectrometer at an ambient temperature of 298 K using a standard high-resolution BBO probe. Fig. 2.5 (a) displays the ^{13}C spectra corresponding to ^{13}C-^{13}C singlet-order at natural abundance obtained using CL singlet sequence without involving any polarization transfer [68]. The recycle delay was set to 35 s (approximately five times T_1 of carbons) and a total 512 scans were recorded for $\tau_{\mathrm{AC}} = 10$s. Although the characteristic signature of the singlet state is visible in terms of the antiphase

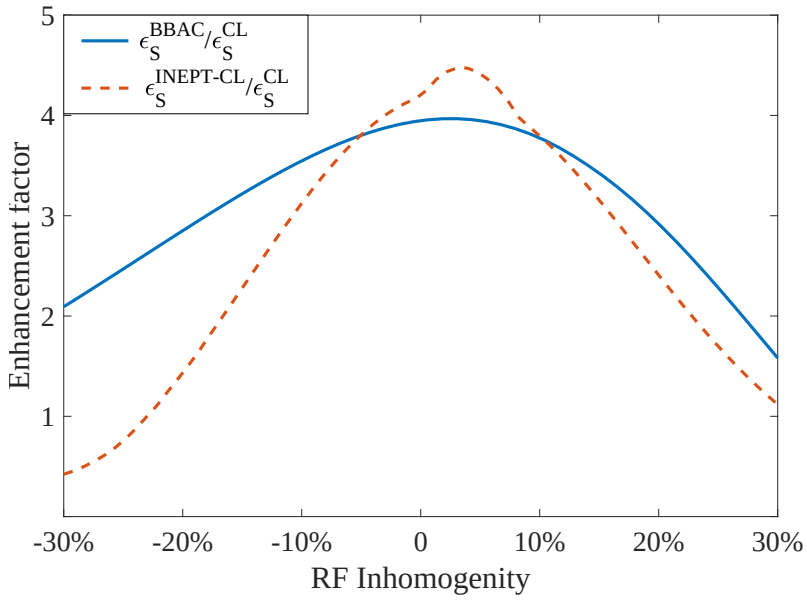

Figure 2.6: Variation of enhancement factor with RF inhomogeneity for INEPT-CL sequence and direct transfer to singlet-order using BBAC .

magnetizations, the signal to noise ratio is rather poor.

Fig. 2.5 (b) and 2.5 (c) display the ^{13}C spectra corresponding to ^{13}C-^{13}C singlet-order using INEPT-CL and BBAC singlet sequences respectively again recorded with 512 scans for spin-lock duration $\tau_{\mathrm{AC}} = 10$s. Since the polarization is mainly contributed by ^{1}H spins, we need a recycle delay of only 15 s (approximately five times T_1 of protons) and accordingly required only half the experimental time as that of without polarization transfer. The estimated enhancements of singlet-order by the polarization transfer schemes are, $\epsilon_S^{\mathrm{INEPT-CL}}/\epsilon_S^{\mathrm{CL}} \approx 2.0$ and $\epsilon_S^{\mathrm{BBAC}}/\epsilon_S^{\mathrm{CL}} \approx 3.4$, leading to an overall reduction in the experimental times by a factor of $(2\sqrt{2})^2 = 8$ and $(3.4\sqrt{2})^2 = 23$ respectively. One of the reasons for higher enhancement of BBAC sequence maybe its relatively higher robustness compared to INEPT-CL, as shown in Fig. 2.6. To simulate the impact of RF inhomogeneity, the fidelity of the singlet order using both INEPT-CL and BBAC sequence was calculated using various values of the amplitude of the applied RF field in the range $[0.7\omega_1, 1.3\omega_1]$, where ω_1 is the nominal amplitude without any RF inhomogeneity. This amounts to 30% RF inhomogeneity. Moreover, the BBAC sequence required less than 80% of RF needed by the minimal INEPT-CL sequence in terms of the total nutation angle.

The enhanced singlet-order allows us to conveniently monitor its decay versus the spin-lock duration τ_{AC}. The results shown in Fig. 2.7 indicate the singlet decay constant T_S of about 25.9

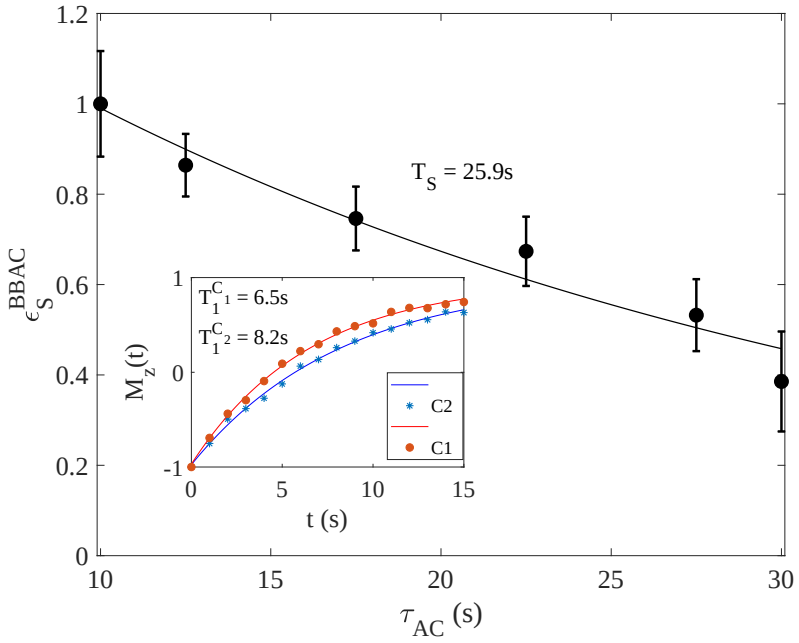

Figure 2.7: The decay of singlet-order versus spin-lock duration τ_{AC}. The vertical axis is normalized w.r.t. the first data point. Inversion-recovery curves and corresponding T_1 values of both carbons are shown in the inset.

s. Thus, the singlet-order is approximately 3 to 4 times longer lived compared to the T_1 values of carbons. In this particular spin system, we did not observe any advantage of HBAC over AC. HBAC is suitable for systems with fast relaxing ancillary spins and very slow relaxing system spins [108]. In such a system, protons recover their magnetization (after AC) much faster than the decay of singlet state, so that further polarization transfer can be carried out. In our system, the T_1 to T_S contrast was insufficient to observe this effect.

We now numerically analyze the BBAC singlet sequence to understand the dynamics of singlet-order enhancement. Fig. 2.8 (a) shows the profile of BBAC pulse. Here time discretization was done with $\Delta t = 500$ µs, and RF amplitude $\Omega_{\mathrm{H}}/(2\pi) = \Omega_{\mathrm{C}}/(2\pi) = 250$ Hz. Thus each bang corresponds to a 45° nutation. At the end of the BBAC sequence the singlet enhancement factor reaches a maximum value of 4 as shown in Fig. 2.8 (b). Experimentally, however, we achieved an enhancement of only 3.4, presumably due to RF inhomogeneity, hardware non-linearity, and relaxation effects.

Since it is harder to fully understand the dynamics of eleven spins leading to the enhanced singlet-order, we analyze the following evolutions. (i) To understand the polarization transfer, we

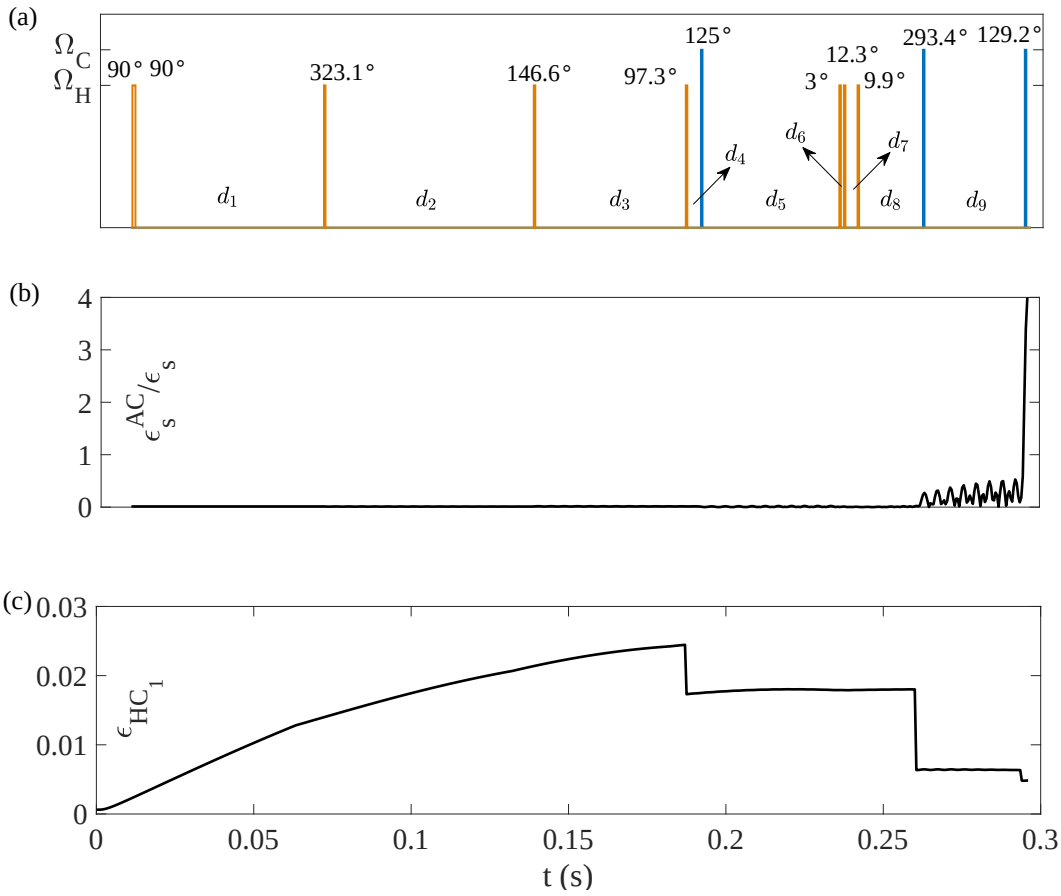

Figure 2.8: (a) Profile of BBAC singlet sequence consisting of bangs on proton as well as carbon channels with amplitudes Ω_{H} and Ω_{C} respectively. Each bang is of duration 0.5 ms. The phases in degrees are shown above the bangs. The delays are: $d_1 = 62.5$ ms , $d_2 = 69$ ms, $d_3 = 50$ ms, $d_4 = 5$ ms, $d_5 = 45.5$ ms, $d_6 = 1.5$ ms, $d_7 = 4.5$ ms, $d_8 = 21.5$ ms, and $d_9 = 33.5$ ms. Progress of (b) simulated enhancement factor $\epsilon_S^{\mathrm{BBAC}}/\epsilon_S^{\mathrm{CL}}$, (c) the evolution of ϵ_{HC_1} quantifying the polarization transfer (Eq.2.15) from protons to carbon spin orders.

take the reduced density matrix of C_1 carbon and one of the protons and estimate

$$\epsilon_{\mathrm{HC}_1} = \sqrt{\sum_{j=x,y,z} \left(\mathrm{Tr}\left[\rho\, I_j^{\mathrm{H}}\, I_z^{\mathrm{C}_1}\right]\right)^2}. \tag{2.15}$$

(ii) To capture the effective generation of the singlet-order, we analyze the reduced density matrix of the two carbons. Fig 2.8 (c) shows the evolution of ϵ_{HC_1} with time. It builds up until the first bang on carbon and then decreases with each carbon bang, indicating the subsequent conversions into the carbon spin orders. Fig. 2.9 (a) and (b) respectively display the evolution of various populations and coherences in the singlet-triplet basis as a function of time starting from state ρ_0 of Eq. 2.10. Sequence starts with a thermal equilibrium populations, which are indicated in the

inset of Fig. 2.9 (a). The degenerate product states $|\uparrow\downarrow\rangle$ and $|\downarrow\uparrow\rangle$ are transformed to $|S_0\rangle$ and $|T_0\rangle$ respectively, which are initially equally populated. However, the states $|\uparrow\uparrow\rangle$ and $|\downarrow\downarrow\rangle$ transform to $|T_+\rangle$ and $|T_-\rangle$ respectively, and accordingly exhibit highest and lowest populations. The relative

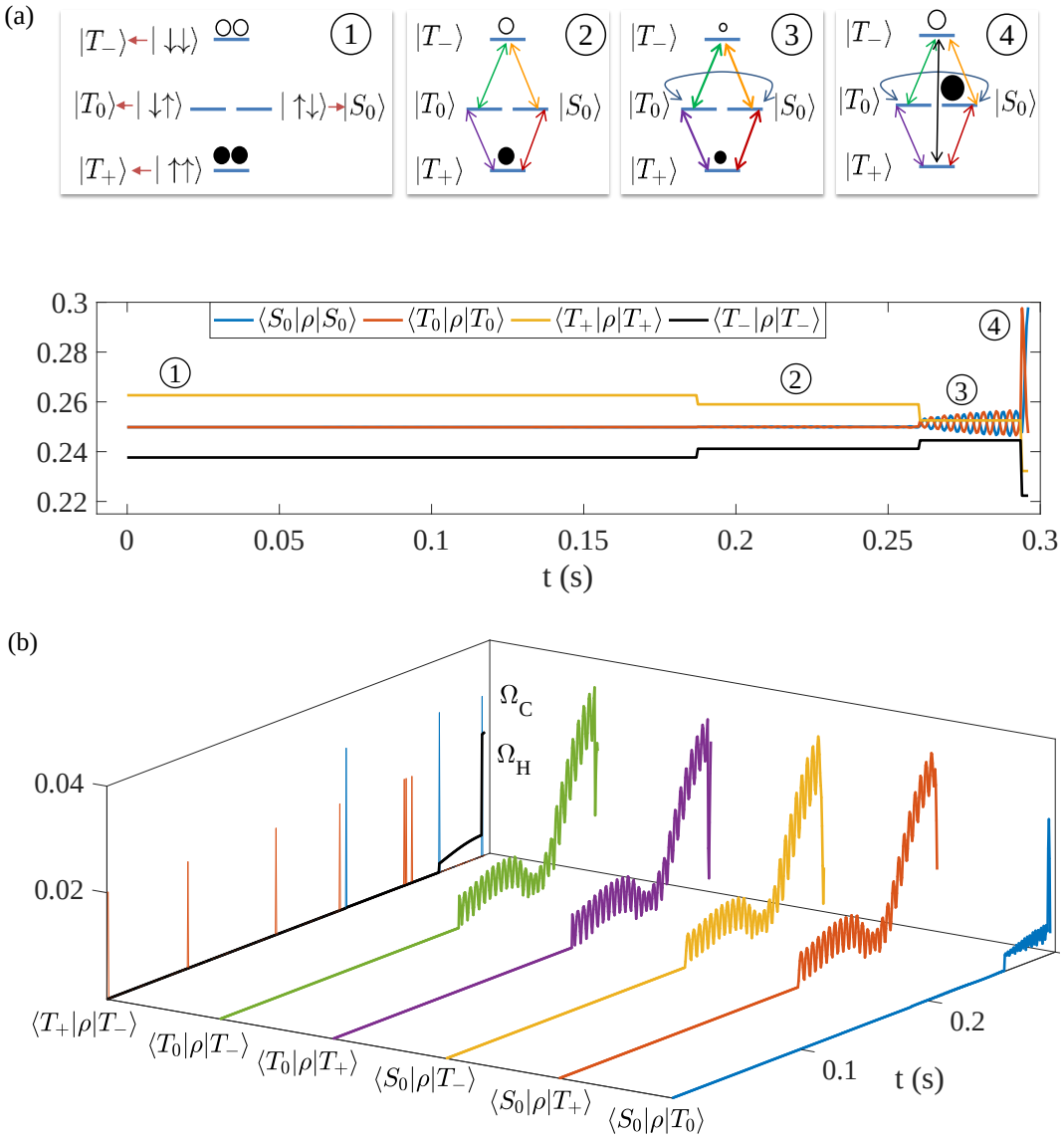

Figure 2.9: (a) Various populations in the singlet-triplet basis, and (b) various coherences in the singlet-triplet basis versus time during the BBAC sequence.

populations are little affected by the proton bangs and are only altered by the carbon bangs. After the first carbon bang, the population of $|T_+\rangle$ decreases and of $|T_-\rangle$ increases, while that of $|T_0\rangle$ and $|S_0\rangle$ remain unaffected. However various single-quantum coherences are also generated, as shown in the second inset of Fig. 2.9 (a). After the second carbon bang, the population

difference between $|T_+\rangle$ and $|T_-\rangle$ are further decreased, while the zero-quantum coherence between $|S_0\rangle$ and $|T_0\rangle$ are created. The last carbon bang brings a large population into $|S_0\rangle$ at the expense of other states. Various coherences still survive to some extent and form the residual part described in Eq. 2.11. During a subsequent spin-lock, singlet-state becomes the ground state, the degenerate triplet states quickly equilibrate, and the short-lived coherences decay away, thus creating enhanced and pure singlet-order.

2.7 Discussions and conclusions

Sophisticated quantum control techniques are recently being used in both spectroscopy as well as in quantum information to achieve complex and precise spin dynamics [43–46, 109–113]. The challenge in many of such techniques is the numerical complexity involved in evaluating and optimizing propagators of large spin systems. In this regard, the Bang-Bang (BB) quantum control technique offers a unique advantage, since it only needs a one-time evaluation of basic propagators by matrix exponentiation. Therefore, we can synthesize BB controls for larger spin-systems. Here we have described the various steps in the BB control technique using a flowchart. Although presently we use the full Hilbert space, it might be possible to achieve a further speed-up by exploiting the symmetry of the spin system.

In this work, we achieve the quantum control of 11-spin system by transferring polarization from nine ancillary spins into the singlet-order of a spin-pair. We experimentally demonstrate this method in a naturally rare ^{13}C-^{13}C spin-pair, with a probability of 0.011%, and obtain an enhanced singlet-order by a factor of 3.4, compared to a standard method without involving polarization transfer. However, owing to the faster T_1 relaxation of the ancillary protons, the BB approach needed only half the experimental time compared to the latter. Thus effectively, we have approximately 23 times reduction in experimental time. Although the above sequence is neither unique nor may be the most optimal one, the significant enhancement achieved by it proves the efficacy of the bang-bang approach.

Exploiting the enhanced sensitivity, we investigated the decay of the singlet-order under spin-lock and found it to be three to four times longer lived compared to individual spin-lattice relaxation time constants. It is interesting to see the feasibility of creating and maintaining long-lived states in such large spin-systems. This offers an opportunity for huge polarization transfer into

singlet-order in a naturally-rare homonuclear spin-pair.

We also investigated the heat-bath algorithmic cooling (HBAC) which attempts to further enhance the singlet-order by iterative transfer of polarization from ancillary spins. HBAC is particularly suited for systems with fast relaxing ancillary spins and slow relaxing target spins [108]. In principle, the long-lived singlet states are ideal for storing the spin-order between the iterations where ancillary spins re-thermalize by giving away extra heat to their bath. With this motivation, we explored HBAC in the 11-spin system described above. However, due to insufficient contrast between the life times of singlet-order and ancillary spins, as well as an insufficient enhancement by each iteration, we could not observe any significant advantage of HBAC process in this system.

Note that there already exits methods such as Nuclear Overhausser Effect (NOE) [114], which exploit cross-relaxation to enhance the polarization of the target qubit. In fact, NOE can be regarded as one of the processes through which HBAC can be performed [115]. It can achieve higher polarization for the target qubit (See Ref. [116] for a detailed analysis) by exploiting cross-relaxation of the qubits as compared to methods which exploit individual relaxations of the qubits such as Partner Pairing Algorithm (PPA) [117].

The methods described here can be applied to other homonuclear spin-pairs such as naturally rare ^{15}N-^{15}N or even naturally abundant ^{31}P-^{31}P pairs. We also anticipate finding many other interesting applications of BB control techniques in spectroscopy as well as in quantum information processing.

CHAPTER 3

Noise spectroscopy of multi-qubit states

Abstract

Characterizing and understanding noise affecting quantum states has immense benefits in spectroscopy as well as in realizing quantum devices. Transverse relaxation times under a set of dynamical decoupling (DD) sequences with varying interpulse delays were earlier used for obtaining the noise spectral densities of single-qubit coherences. In this work, using a pair of homonuclear spins and NMR techniques, we experimentally characterize noise in certain decoherence-free subspaces. We also explore the noise of similar states in a heteronuclear spin pair. Further, using a 10-qubit system, we investigate noise profiles of various multiqubit coherences and study the scaling of noise with respect to the coherence order. Finally, using the experimentally obtained noise spectrum of the 10-qubit NOON state, we predict the performance of a Uhrig DD sequence and verify it experimentally.

Reported in

Deepak Khurana, Govind Unnikrishnan, T. S. Mahesh, *Spectral investigation of the noise influencing multi-qubit states,* Phys. Rev. A 94, 062334 (2016).

3.1 Introduction

The inevitable presence of local or global electromagnetic noise may cause the loss of quantum coherences of spin systems or induce the redistribution of spin populations. This phenomenon, which is often described in terms of decoherence or depolarization, appears in NMR as a net relaxation of transverse or longitudinal magnetization. In order to build robust quantum technologies, we need to devise strategies to protect the qubit from the detrimental effect of the decoherence. To this end, passive techniques like decoherence-free subspaces (DFS) [118, 119] as well as active techniques like dynamical decoupling (DD) [120] and quantum error correcting codes [121, 122] have been developed. While the passive techniques rely on exploiting the

symmetries in the interaction Hamiltonian, the active techniques focus on systematic modulation of the quantum states to suppress decoherence. To ensure maximum efficiency, these strategies must be judiciously optimized according to the characteristic of the environmental noise. Hence it is crucial to characterize the surrounding environment not only to provides insights into the physical process of noise affecting the qubit, but also to optimize DFS conditions as well as to design better controls for active suppression of noise.

Fortunately, all the relevant information to completely characterize the environmental noise is encoded in the noise spectrum, which records the amount of noise present at various frequencies. Interestingly, the qubit itself assist us in finding noise spectrum because the surrounding environment leaves its traces on the dynamics of the qubit while interacting with it. However, these traces are the collective fingerprint of all the frequency components of noise together. The technique of filtering out contribution of each frequency component from this collective fingerprint is called *Quantum noise spectroscopy* (QNS). The first procedure to carry out QNS was independently proposed by Yuge et al. [123] and Àlvarez and Suter [124] which uses the filtering capability of DD sequences [125]. This method is extensively reviewed in Ref [126]. Further, Szańkowski et al. [127] proposed a method to probe spectra of correlation between noise sources by using two qubits under application of appropriate DD sequences which is further generalized to the case of multiple qubits in Ref. [128].

In this chapter, I discuss the noise influencing various types of quantum coherences, including DFSs, single-quantum (SQ), as well as multiple quantum coherences (MQC). An example of DFS is the singlet subspace in a two-qubit system [119]. As described in last chapter, an excess population in the singlet state, over the uniformly distributed triplet states, is termed as a singlet order. It has been shown that such an order, under favorable circumstances, has much longer lifetimes than the usual longitudinal relaxation time scales and is therefore known as a long-lived singlet order (LLS) [68]. Similarly, the coherence between the singlet state and the zero-quantum triplet state also has longer life-times than the usual transverse relaxation time scales, and is therefore termed as a long-lived coherence (LLC) [129]. On the other hand, several other SQ and MQCs lack the symmetry properties and are consequently prone to stronger decoherence. Recently, longer lifetime of LLS and LLC is exploited in NMR for many applications such as storage of hyperpolarization [93], studying slow dynamic processes [85], estimation of J-coupling

with higher precision [130] and many more [71]. Similarly, MQCs have been used for quantum sensing [131] and probing information scrambling using out-of-time ordered correlations [132, 133]. Hence it imperative to investigate the noise affecting these special coherences to ensure their robust operation in the aforementioned applications.

The chapter is organized as follows. In the following section, I describe the theoretical formalism of QNS. In section 3.3 and 3.4, I describe experimental extraction of the noise spectra affecting DFS and MQCs, respectively. Finally I conclude in section 3.5.

3.2 Theory of noise spectroscopy

Here I provide a brief review of the theoretical aspects of QNS. We consider the qubit to be coupled to a bath via a purely dephasing interaction. Assuming the system Hamiltonian $\mathcal{H}_S = \omega_0\sigma_z/2$ and the bath Hamiltonian $\mathcal{H}_B$, the joint-evolution is described by the Hamiltonian

$$\mathcal{H} = \mathcal{H}_S + \mathcal{H}_{SB} + \mathcal{H}_B. \tag{3.1}$$

Here $\mathcal{H}_{SB} = j_{SB}\sigma_z B/2$ describes the system-bath interaction with B being the bath operator and j_{SB} being the system-bath coupling strength. In the interaction picture of the bath Hamiltonian, the bath operator

$$B'(t) = e^{-i\mathcal{H}_B t} B e^{i\mathcal{H}_B t} \tag{3.2}$$

becomes time-dependent. After invoking semi-classical approximation and tracing-out the bath variables, the Hamiltonian reduces to

$$\mathcal{H}' = \mathcal{H}_S + j_{SB} b'(t)\sigma_z/2, \tag{3.3}$$

where $b'(t)$ is a stochastic function. We treat the bath to be classical and $b'(t)$ to be zero-mean stationary Gaussian process, as has been assumed before [123, 124]. However, an extension to a non-Gaussian case has also been reported recently [134, 135].

Suppose an external control field is applied for a total time T in the form of DD sequence involving a series of on resonant π pules to refocus the dephasing caused by interaction Hamiltonian. In the interaction representation associated with the DD sequence, the Hamiltonian trans-

forms to

$$\mathcal{H}'' = f(t,T) j_{SB} b'(t) \sigma_z/2, \tag{3.4}$$

where $f(t,T)$ is the modulation function that switches between $+1$ and -1 with the application of every π-pulse (see Fig. 3.1). The Fourier transform of $f(t,T)$ is known as the Filter function $F(\omega,T) = \int dt e^{-i\omega t} f(t,T)$.

Noise spectral density $S(\omega)$ is defined as the Fourier transform of the autocorrelation function $g(t_2 - t_1) = \langle b'(t_1) b'(t_2) \rangle$, i.e.,

$$S(\omega) = \int_{-\infty}^{\infty} dt e^{-i\omega(t_2 - t_1)} g(t_2 - t_1). \tag{3.5}$$

The decay of quantum coherence is influenced by the noise spectral density as well as the filter function [136, 137]. This decay can be modeled in the form $\exp[-\chi(t)]$, wherein the time-dependent argument is given by,

$$\chi(t) = \frac{1}{2\pi} \int_0^{\infty} d\omega S(\omega) |F(\omega,T)|^2, \tag{3.6}$$

for case of a symmetric auto correlation function ($S(-\omega) = S(\omega)$) [138–140]. For a given distribution of pulses, modulation function $f(t)$ can be written as Fourier series

$$f(t,T) = \Theta(T-t)\Theta(t) \sum_{k=-\infty}^{\infty} A_k \exp(i\omega_k t), \tag{3.7}$$

with $\omega_k = k\omega_0$ where ω_0 is characteristic frequency which is inverse of period of $f(t,T)$ associated with the applied DD sequence. For the CPMG sequence [141, 142] with inter pulse delay 2τ, $\omega_0 = 2\pi/4\tau = \pi/2\tau$. Now the filter function can be written as

$$F(\omega,T) = \int_0^T dt e^{-i\omega t} \sum_k A_k e^{i\omega_k t} = \sum_k A_k e^{-\frac{iT(\omega-\omega_k)}{2}} T\text{sinc}\left[\frac{T(\omega-\omega_k)}{2}\right], \tag{3.8}$$

where $\text{sinc}(x) = \sin(x)/x$. After plugging $F(\omega,T)$ in Eq. 3.6 and noting that $T\text{sinc}(\omega T/2) \to 2\pi\delta(\omega)$ and $T\text{sinc}^2(\omega T/2) \to 2\pi\delta(\omega)$ as $T \to \infty$,

$$\chi(T) \approx T \sum_{k=0}^{\infty} |A_k|^2 S(\omega_k). \tag{3.9}$$

If the decay can be approximated to a exponential with decay rate $1/T_2$ then

$$\frac{1}{T_2} \approx \sum_{k=0}^{\infty} |A_k|^2 S(\omega_k). \tag{3.10}$$

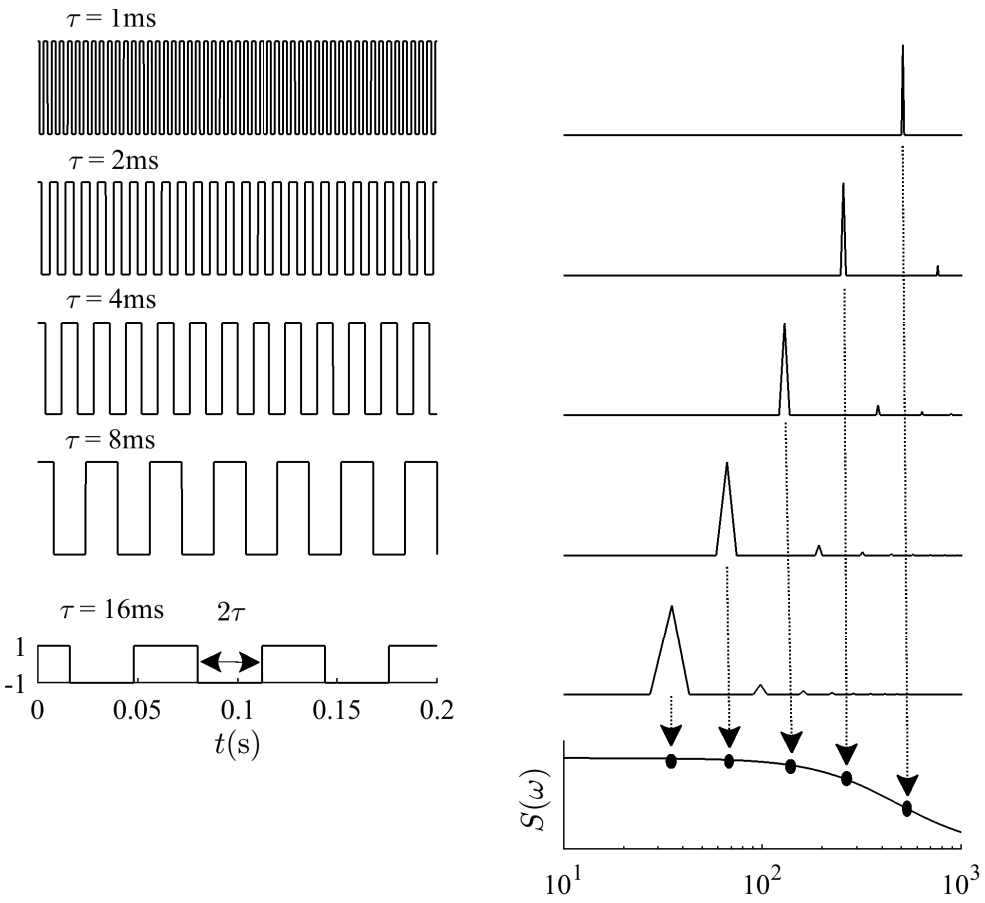

Figure 3.1: The modulation functions $f(t,T)$ (left column) and the corresponding Fourier transforms, i.e., Filter functions $F(\omega,T)$ (right column). The 1st order sampling points of the filter functions are illustrated using a schematic spectral density function $S(\omega)$ as shown in the lowest trace of the right column.

In the case of a free-evolution without any DD sequence, the modulation function $f(t,T)$ becomes constant and therefore, the filter-function $F(\omega,T)$ is a sinc-function centered at $\omega = 0$, and the decay rate $1/T_2$ depends only on $S(0)$. For the CPMG sequence with uniformly distributed π pulses at an interval 2τ, $f(t)$ switches between $+1$ and -1 with a period 4τ. The schematic diagrams of $f(t,T)$ and the corresponding filter functions $|F(\omega,T)|^2$ for a set of τ values are shown in Fig. 3.1. In this case, $A_k^2 = (4/\pi^2 k^2)$ for odd k and $A_k = 0$ otherwise.

Hence

$$\frac{1}{T_2} = \frac{4}{\pi^2} \sum_{l=0}^{\infty} \frac{1}{(2l+1)^2} S(\omega_{2l+1}). \tag{3.11}$$

Thus the decay rate $1/T_2$ for a given τ is determined by the harmonics at $\omega_{2l+1} = \pi(2l+1)/2\tau$, as illustrated in Fig. 3.1. Hence from the experimentally measured T_2 values for $\tau \in [\tau_{\min}, \tau_{\max}]$, one can extract the spectral density points $S(\omega_{2l+1})$ in the range $\omega \in [\pi/2\tau_{\max}, \pi/2\tau_{\min}]$ by inverting the above equation. In the following we discuss two ways of extracting the noise spectrum $S(\omega)$ from Eq. 3.11.

An approximate way is to truncate the series in Eq. 3.11 to the zeroth order term so that,

$$S\left(\frac{\pi}{2\tau}\right) \approx \frac{\pi^2}{4T_2}. \tag{3.12}$$

This method is suitable for spectral densities with sharp cut-offs at low-frequencies [143]. Otherwise, ignoring higher order terms may introduce an error of up to about 10%.

On the other hand, we can account for the zeroth as well as many higher order terms of spectral density by using a suitable model function for the spectral density. Random isotropic rotations of liquid molecules usually lead to exponential autocorrelation function and therefore, the corresponding spectral density is Lorentzian [136]. Multiple relaxation sources may lead to multi-Lorentzian spectral density, as observed in the experiments described in the next section. Our phenomenological model thus consists of a linear combination of Lorentzians

$$S_L(\omega) = \sum_{j=1}^{L} \frac{\lambda_j}{(\omega - \omega_j)^2 + \lambda_j^2}. \tag{3.13}$$

The parameters ω_j (center-frequency) and λ_j (line-width) can be determined by numerically maximizing the overlap between the experimental T_2 values and those calculated using the model function $S_L(\omega)$. Another benefit of obtaining the functional form of spectral density is that it allows one to evaluate the performance of various DD sequences at arbitrary inter-pulse spacing, as illustrated in section 3.4.

In the case of multi-qubit systems, all the qubits may be coupled to a common environment, or each qubit can be coupled to a separate environment. The former and later case correspond to maximally correlated or partially correlated environments. Hence, along with the self-noise spectrum due to each noise source, the coherence is also affected by correlation among them.

In this regard, protocols to completely characterize the environment by monitoring the dynamics of various coherences of a multi-qubit system, under careful application DD sequences, was proposed [127, 128]. However, in this work, we apply the same CPMG sequence on all the qubits, which captures the combined effect of self and correlation noise spectra.

3.3 Noise spectroscopy of long-lived states

In this section, we compare the noise influencing two-qubit coherences in homonuclear as well as hetronuclear NMR spin systems. Specifically, we focus on SQ coherences and specific superpositions of singlet and triplet states.

3.3.1 Homonuclaer spin pair

We used the two phenyl ^{1}H nuclei of 2,3,6-trichlorophenol dissolved in dimethyl sulphoxide-D6. The experiments were carried out at 300 K in two different magnetic fields corresponding to Larmor frequencies $\nu_0 = 400$ MHz as well as $\nu_0 = 600$ MHz. The chemical shift difference $\Delta\nu \times 10^6/\nu_0 = 0.21$ ppm and the scalar coupling constant $J = 8$ Hz. Under weak-coupling approximation, the NMR Hamiltonian is

$$\mathcal{H} = \pi\Delta\nu I_z - \pi\Delta\nu S_z + \pi J 2 I_z S_z, \tag{3.14}$$

where I_z and S_z are the spin operators.

The natural choice for expressing LLS and LLC is the singlet triplet basis, formed by the eigenvectors of the isotropic interaction Hamiltonian $\mathbf{I} \cdot \mathbf{S}$, i.e.,

$$\begin{aligned} |T_0\rangle &= \frac{1}{\sqrt{2}}(|01\rangle + |10\rangle), \\ |T_+\rangle &= |00\rangle, \\ |T_-\rangle &= |11\rangle, \text{ and} \\ |S_0\rangle &= \frac{1}{\sqrt{2}}(|01\rangle - |10\rangle), \end{aligned} \tag{3.15}$$

where $\{|00\rangle, |01\rangle, |10\rangle, |11\rangle\}$ form the Zeeman eigenbasis.

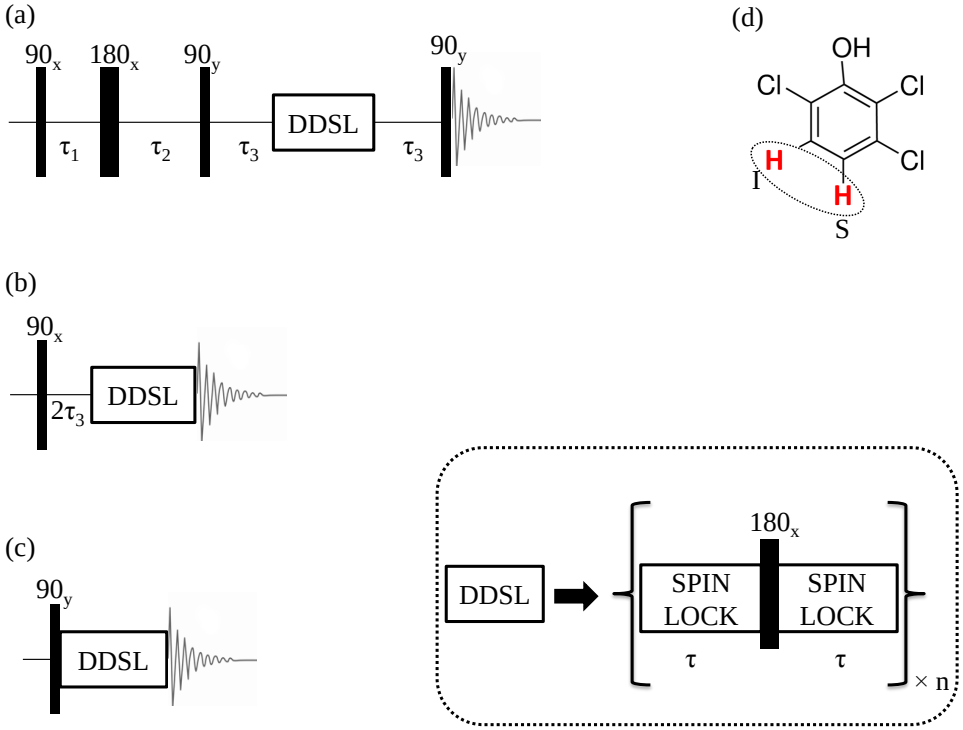

Figure 3.2: Pulse sequences used to measure the noise spectrum of (a) ρ_{LLS}, (b) ρ_{LLC}, and (c) ρ_{SL}. Here $\tau_1 = 1/(4J)$, $\tau_2 = 1/(4J) + 1/(2\Delta\nu)$, $\tau_3 = 1/(4\Delta\nu)$, and n is the number of times the loop is repeated. (d) Structure of 2,3,6-trichlorophenol. The CPMG DD sequence with spin-lock along x-axis is shown in the inset (DDSL).

In particular, we focus on the following coherences:

$$\begin{aligned}
\rho_{\mathrm{LLS}} &= |S_0\rangle\langle S_0| - |T_0\rangle\langle T_0| \\
\rho_{\mathrm{LLC}} &= |S_0\rangle\langle T_0| + |T_0\rangle\langle S_0| \\
\rho_{\mathrm{SL}} &= |T_+\rangle\langle T_+| - |T_-\rangle\langle T_-|.
\end{aligned} \tag{3.16}$$

In the above, ρ_{LLS}, ρ_{LLC}, and ρ_{SL} are realized by preparing the states $-\mathbf{I}\cdot\mathbf{S}$, $I_x - S_x$, and $I_x + S_x$ respectively, and applying a strong spin-lock along the x axis [68, 129]. Here we have considered ρ_{SL} for the sake of comparison with the other long-lived states. The pulse sequences corresponding to these states are shown in Fig. 3.2.

We use the multi-Lorentzian model function described in Sec. 3.2 to extract the noise spectrum. The best fit was achieved with a minimum of three Lorentzian functions (i.e., $L = 3$) as described in Eq. 3.13. We scan over a range of spectral frequencies $\omega = \pi/2\tau$ by varying the duration 2τ between the π pulses, and measure the corresponding T_2 values. WALTZ-16 spin-

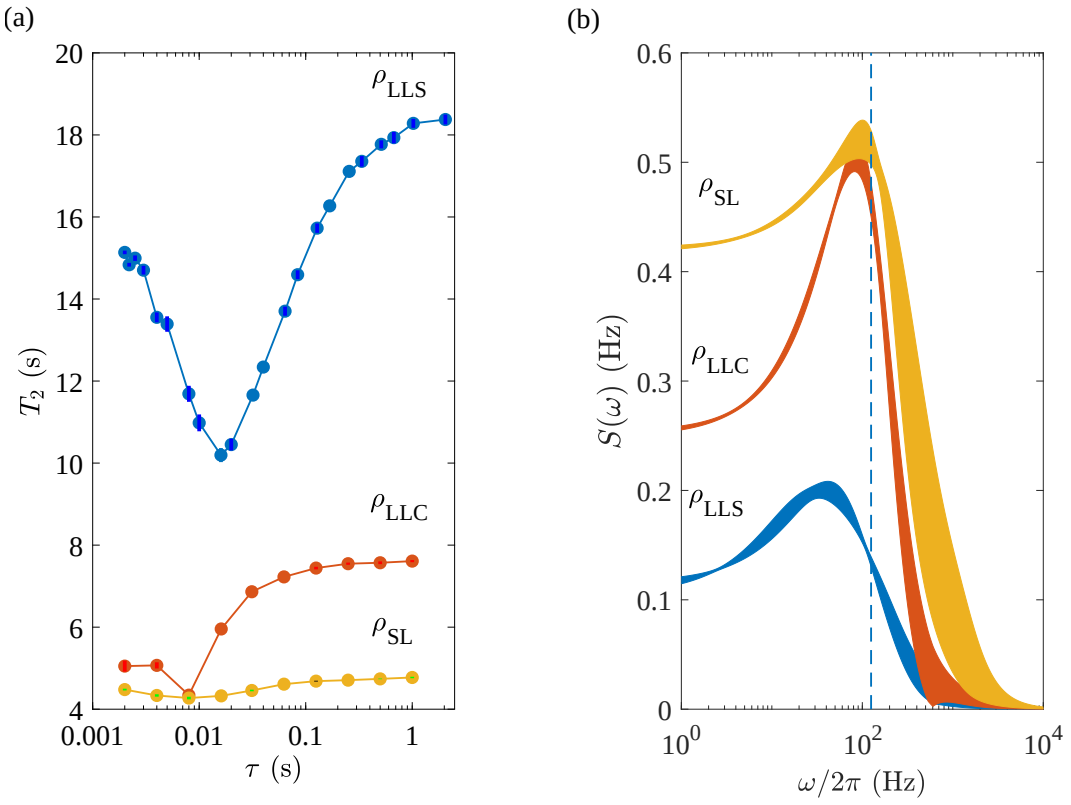

Figure 3.3: (a) Experimental decay constants (dots) of 2,3,6-trichlorophenol (averaged for both protons) in 400 MHz spectrometer for a range of τ values and for different states as indicated. The solid lines correspond to decay constants obtained from the best fit by the 3-Lorentzian model as described in Eq. 3.13. (b) The corresponding noise spectral density bands. The dashed line at 125 Hz corresponds to the maximum harmonics sampled with $\tau = 2$ ms.

lock of 2 kHz amplitude was applied along the x-axis during the delays between the π pulses. The experimental T_2 values for all the three states and for τ values ranging from 2 ms to 2 s are displayed in Fig. 3.3(a). Note that the major source of noise in our experiments is time-dependent inhomogeneities in the static field (though the inhomogeneities in the magnetic field lead to static perturbation, the molecular motion makes it time-dependent [144]) which has correlation time of ms to s. That is why DD sequences with interpulse delay in ms to s range can suppress the decoherence and can be used for noise spectroscopy. The uncertainties in the noise spectrum (represented by the width of the bands) are estimated by several iterations of maximizations also considering the standard deviations in T_2 values.

As expected, ρ_{LLS} has the lowest noise in the whole-frequency range indicating long-lifetimes. On the other hand, ρ_{SL} has the highest noise indicating a relatively short-lived state. The long-

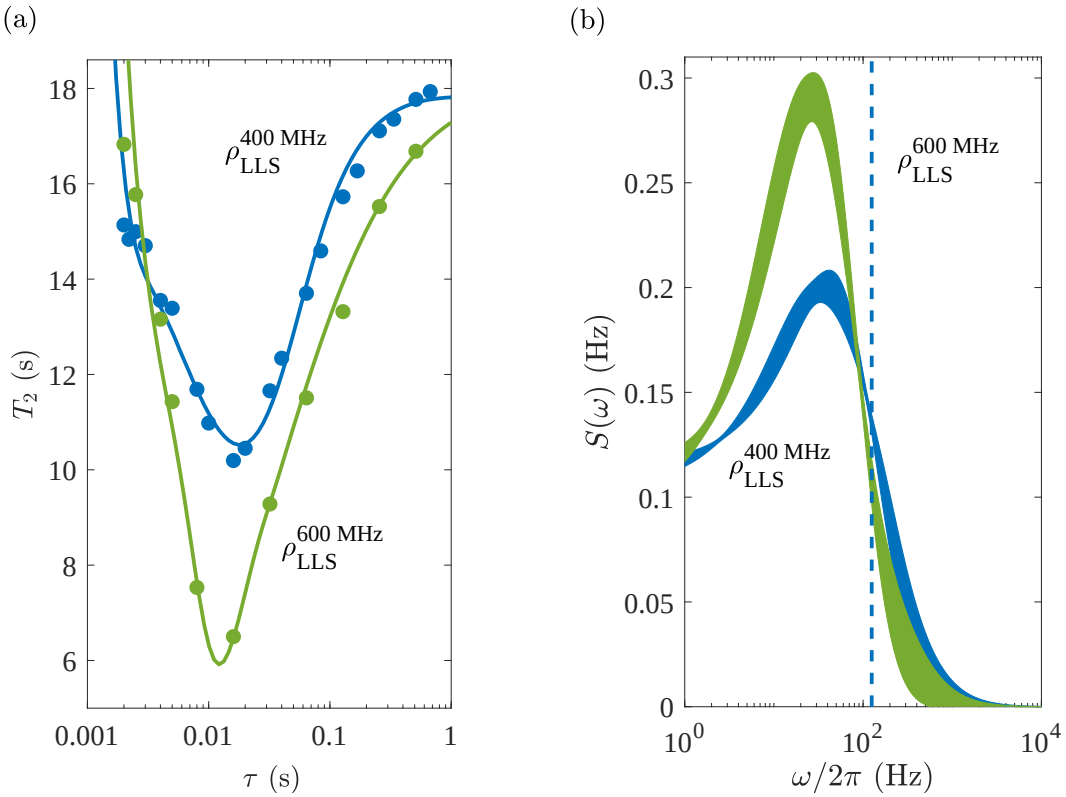

Figure 3.4: (a) The experimental decay constants (dots) at various τ delays for the singlet state ρ_{LLS} at two different magnetic fields, i.e., 400 MHz and 600 MHz as indicated. The solid lines correspond to decay constants obtained from the best fit by the 3-Lorentzian model as described in Eq. 3.13. (b) The corresponding noise spectra.

lived coherence ρ_{LLC} has an intermediate noise-profile. Owing to the hardware limitations, the highest frequency sampled by the experiments is 125 Hz (indicated by a dotted line in Fig. 3.3(b)), corresponding $\tau = 2$ ms. The noise-profiles above this cutoff frequency are basically an extrapolation obtained by the model functions.

Interestingly, in all the three spectral-density profiles we observe a hump close to 100 Hz. Replacing the hydroxyl proton with deuterium did not affect the hump. We have also observed a systematic dependence of the hump with the spin-lock power, which possibly relates its origin to an interference between spin-lock and DD sequences. However further investigations are required to confirm this point.

Although it is well known that singlet state is longer lived at lower fields [145, 146], it is not obvious how the spectral characteristics of noise changes under a higher field. Therefore it is useful to compare the noise spectrum at two different fields. With this intention, we have

measured the noises of singlet state of same system, i.e., the proton pair of 2,3,6-trichlorophenol, at 400 MHz as well as at 600 MHz spectrometers under identical conditions. The T_2 values and the corresponding spectral density bands are shown in Fig. 3.4. As expected, the noise is significantly stronger at 600 MHz.

3.3.2 Heteronuclear spin-pair

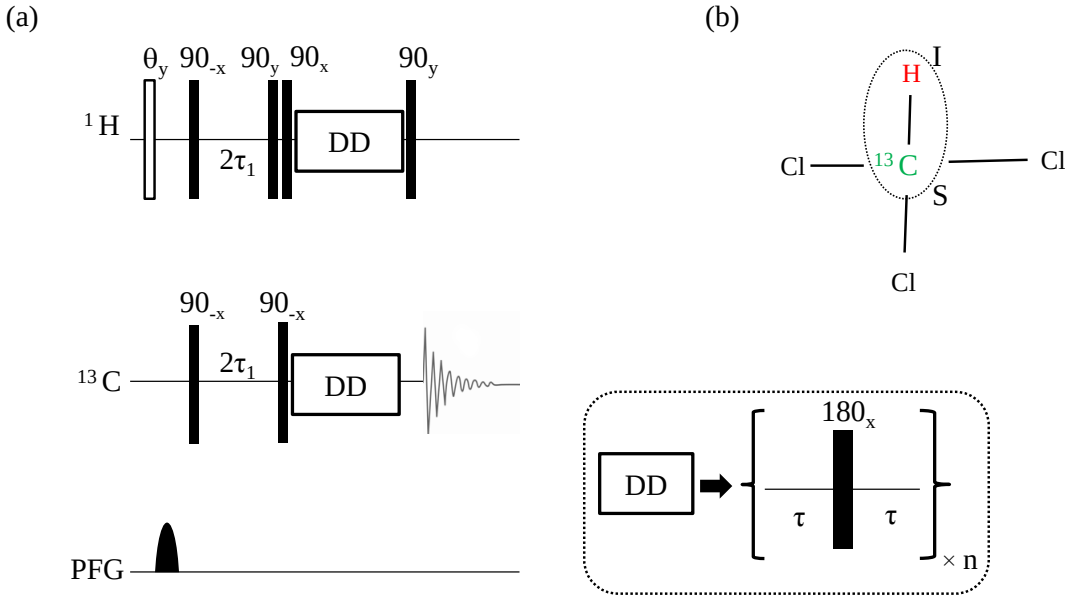

Figure 3.5: (a) Pulse sequence to measure noise spectrum in a heteronuclear spin system. (b) Molecular structure of Chloroform. Here singlet state is prepared on ^{1}H and ^{13}C spins with a coupling constant $J_{\mathrm{CH}} = 209$ Hz between them. The CPMG DD sequence is shown in the inset.

In a hetronuclear spin pair, such as ^{1}H-^{13}C in ^{13}C Chlorform (dissolved in $CDCl_3$; see Fig. 3.5b), the singlet subspace is not a DFS, because a strong magnetic field breaks the symmetry between two spins and a spin-lock to restore the symmetry is not practical. Therefore, a heteronuclear singlet-state, though easy to prepare, is no longer an eigenstate of the interaction Hamiltonian. A pulse sequence to measure their noise spectrum is shown in Fig. 3.5a. It begins with a $\theta = \cos^{-1}(1/4)$ pulse on ^{1}H spin followed by a pulsed-field-gradient to equalize the polarizations and prepare the state $I_z + S_z$. The following RF pulses and delays convert it to $-I_xS_x - I_yS_y \equiv |S_0\rangle\langle S_0| - |T_0\rangle\langle T_0|$. A CPMG DD sequence with a variable τ delay followed by a final 90_y on ^{1}H is then used to measure the noise spectrum. The results are shown in Fig. 3.6. For comparison, we have also included the noise spectra of single-spin states I_x and S_x. Here

^{1}H spin has longer T_2 values and accordingly lower noise profile compared to ^{13}C. Unlike in the homonuclear case, the heteronuclear singlet has the shortest T_2 values and therefore highest noise profile. Therefore a heteronuclear singlet is not an LLS at high fields [71].

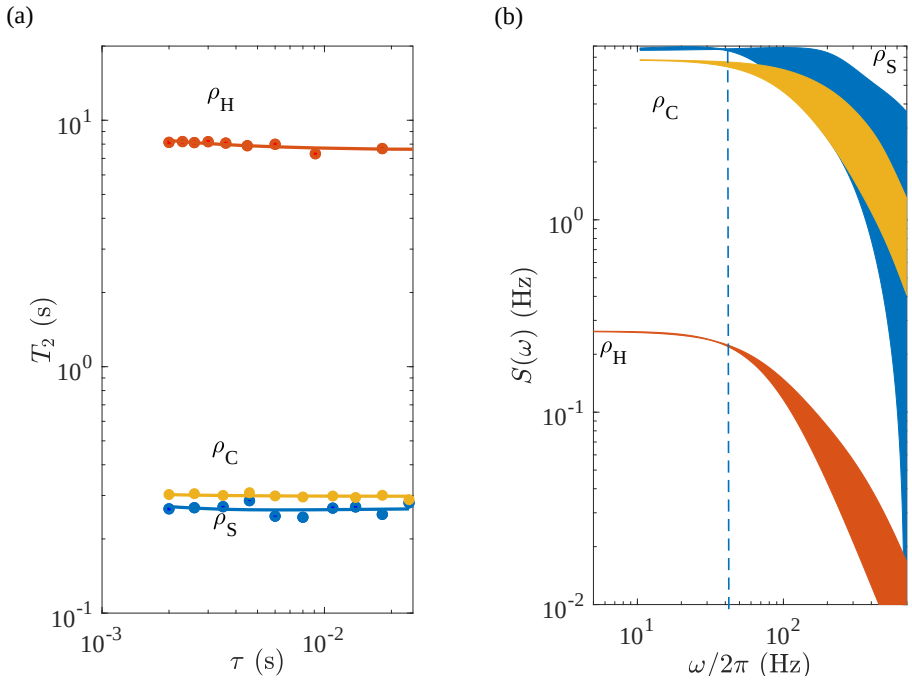

Figure 3.6: (a) The experimental decay constants (dots) of ^{13}C-Chloroform at various τ delays for single spin states $\rho_H = I_x$, $\rho_C = S_x$, and the singlet state ρ_S at 500 MHz. The solid lines correspond to decay constants obtained from the best fit by the 3-Lorentzian model as described in Eq. 3.13. (b) The corresponding noise spectra.

3.4 Noise spectroscopy of Multiple quantum coherences (MQC)

Consider an N-spin star-topology system wherein a central spin (denoted by M) is uniformly coupled to $N-1$ magnetically equivalent spins (denoted by A). Such a system allows a convenient way to prepare many large quantum coherences. The method involves applying a Hadamard gate (denoted by H) on the central spin followed by a CNOT gate as described in Fig. 3.7. In thermal equilibrium, the central spin will have an excess $|0\rangle_M$ population while the surrounding spins have a Boltzmann distribution over all the states $|N-1,0\rangle_A$ to $|0,N-1\rangle_A$, wherein the first and second numbers denote the numbers of spins in $|0\rangle$ and $|1\rangle$ states respectively. The effect of Hadamard and CNOT gates can now be described as

$$
\begin{aligned}
&|0\rangle_M \sum_{k=0}^{N-1} |N-1-k,k\rangle_A \\
&\xrightarrow{\text{H}} \frac{|0\rangle_M + |1\rangle_M}{\sqrt{2}} \sum_{k=0}^{N-1} |N-1-k,k\rangle_A \\
&\xrightarrow{\text{CNOT}} \frac{1}{\sqrt{2}} \sum_{k=0}^{N-1} |0\rangle_M |N-1-k,k\rangle_A + |1\rangle_M |k,N-1-k\rangle_A.
\end{aligned}
$$

The last sum represents a collection of coherences with quantum numbers $N, N-2, \cdots, 0$ for even N and $N, N-2, \cdots, 1$ for odd N. Such coherences are often referred to as $|\text{MSSM}\rangle$ (many-some, some-many) states [131]. A special MSSM state is the N-quantum $|\text{NOON}\rangle$ state

$$|\text{NOON}\rangle = (|000..0\rangle + |111..1\rangle)/\sqrt{2}. \tag{3.17}$$

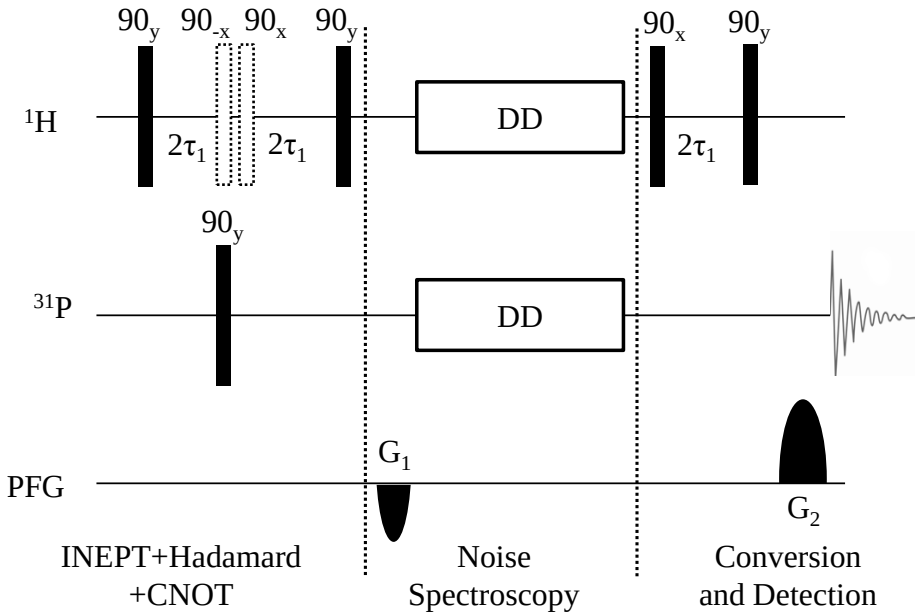

Figure 3.7: Pulse sequence to measure noise spectra of the MSSM states. An initial INEPT (insensitive nuclei enhanced by polarization transfer) [36] operation is used to transfer magnetization from ^{1}H to ^{31}P. The PFGs G_1 and G_2 are chosen such that $\phi_2(k) = -\phi_1(k)$ to select out an MSSM state with a particular lopsidedness $l(k)$. A CPMG-DD sequence with composite π-pulses was used. Dashed lines are guide for the reader to separate the three compartments according to their purpose: (i) preparation of MQCs (INEPT+Hadamrd+CNOT) (ii) Noise spectroscopy of MQCs and (iii) Observation of MQCs (conversion to single quantum coherences).

The MSSM states can be individually studied by selective filtering of their signals using a pair

of pulsed-field-gradients (PFG) (see Fig. 3.7). If γ_A and γ_M denote the respective gyromagnetic ratios of A and M spins, we can express the dephasing caused by the first PFG by,

$$\phi_1(k) \propto \frac{\gamma_M + (N-2k-1)\gamma_A}{\gamma_A} = l(k), \tag{3.18}$$

where the term in the right hand side is known as the lopsidedness of the MSSM state and

$$\frac{\gamma_M - (N-1)\gamma_A}{\gamma_A} \leq l(k) \leq \frac{\gamma_M + (N-1)\gamma_A}{\gamma_A}. \tag{3.19}$$

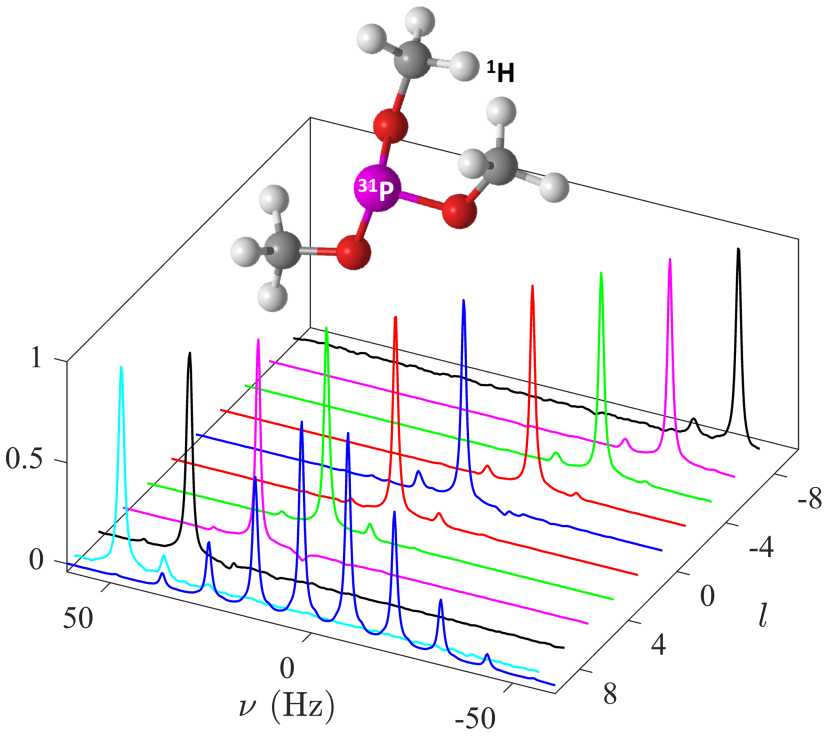

Figure 3.8: The spectral lines corresponding to various MSSM states with varying lopsidedness l. Each spectral line is individually normalized. The reference spectrum with all the lines is shown at the front. The structure of Trimethylphosphite is also shown at the top-left corner.

Each MSSM state is converted back into an observable single-quantum M spin coherence by the application of a second CNOT

$$\frac{1}{\sqrt{2}} \sum_{k=0}^{N-1} |0\rangle_M |N-1-k, k\rangle_A + e^{i\phi_1(k)} |1\rangle_M |k, N-1-k\rangle_A$$
$$\xrightarrow{CNOT} \left(\sum_{k=0}^{N-1} \frac{|0\rangle_M + e^{i\phi_1(k)}|1\rangle_M}{\sqrt{2}} \right) |N-1-k, k\rangle_A.$$

Selection of the signal from a desired MSSM state with a particular $l(k)$ value is achieved with the help of a second PFG which introduces a phase $\phi_2(k) = -\phi_1(k)$. The noise spectroscopy of the MSSM states can be studied by inserting the DD sequence just before the second CNOT (see Fig. 3.7).

Experiments were carried out in a Bruker 500 MHz spectrometer at 300 K. Trimethylphosphite (see Fig. 3.8) dissolved in DMSO was used as a 10-spin star-topology system including a central ^{31}P spin (M spin) and the nine surrounding ^{1}H spins (A spins). The scalar spin-spin coupling J_{PH} was about 11 Hz. The signals from various MSSM states (obtained with the pulse-sequence shown in Fig. 3.7) along with a reference spectrum are shown in Fig. 3.8.

Results and discussions: The results of the noise spectroscopy of various MSSM states are shown in Fig. 3.9. As expected, the spectral density profiles appear to go higher with the magnitude of the lopsidedness, and accordingly the NOON state has the highest noise profile.

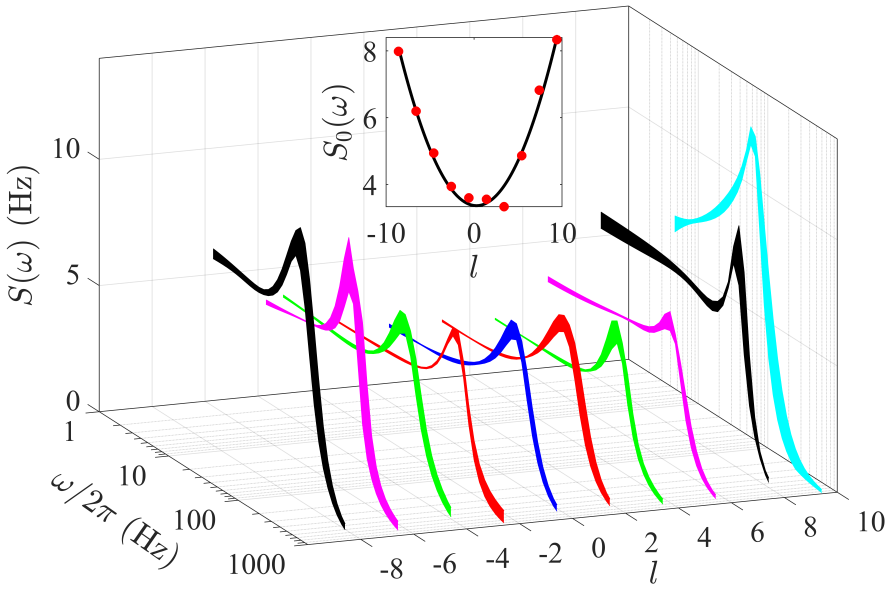

Figure 3.9: Trimethylphosphite noise-spectra for various MSSM states with different lopsidedness l. The dashed lines parallel to l-axis represent the maximum frequency (250 Hz) sampled in experiments. The inset shows the scaling of low-frequency spectral density values with l.

It is interesting to study the scaling of the low-frequency noise ($\approx S(0)$) versus the lopsidedness. The inset of Fig. 3.9 shows the experimental values of low-frequency noise (at lowest frequencies sampled) and a fit with a shifted parabola $c_2 l^2 + c_0$. The best fit was found at $c_2 = 0.06 \pm 0.01$ and $c_0 = 3.37 \pm 0.34$. A quadratic scaling of noise with lopsidedness is obvious

from the inset in Fig. 3.9.

According to Redfield theory of relaxation, the transverse relaxation is a result of two processes - adiabatic and nonadiabatic [136, 147]. The energy conserving adiabatic part arises by longitudinal noise and leads to dephasing. The nonadiabatic part is due to the transverse noise and can induce transitions. Tang et al had observed that the completely correlated longitudinal noise results in relaxation rates that vary quadratically with the coherence order [148]. In our system, the coherence order is characterized by lopsidedness. Thus the quadratic dependence of spectral density with lopsidedness points out that the noise is predominantly correlated, i.e., noise affects all the spins identically. The background part in the scaling (c_0) is due remaining contributions including the nonadiabatic relaxation and the self-relaxation of the probe qubit (^{31}P). It can be noted that similar studies of scaling of decoherence were earlier reported in a solid state NMR system by Krojanski et al [149].

An immediate application of extracting the noise spectrum is in evaluating the performances of various types DD sequences and selecting the optimum sequence for preserving quantum coherences. Uhrig dynamical decoupling (UDD) [150], for example involves, a nonuniform distribution of π pulses placed at time instants

$$t_j = \tau_c \sin^2\left(\frac{\pi j}{2N_\pi + 2}\right), \tag{3.20}$$

where N_π is the total number of π pulses in one period (τ_c), also known as the order of the UDD sequence (denoted UDD-N$_\pi$). It can be easily seen that UDD-1 and UDD-2 are identical to a CPMG sequence.

Having the functional form of the noise spectral density we can now predict the relative decay rates of a quantum state under a given DD sequence. As an example, the band in Fig. 4.4 shows the the predicated decay rates of the NOON state (spectral density shown in Fig. 3.9) under UDD-3 sequence for a range of τ_c values. The corresponding experimental decay rates are shown by dots. The reasonable agreement between experimental and predicted values of decay rates demonstrates the benefit of extracting the spectral distribution of noise. Similar results were obtained in the case of other MSSM states. It should be noted that imperfections in the π-pulses such as finite duration, sensitivity to RF inhomogeneity over the sample volume, and calibration errors may introduce additional uncertainties in the noise-spectrum estimation and may affect DD

performance as well.

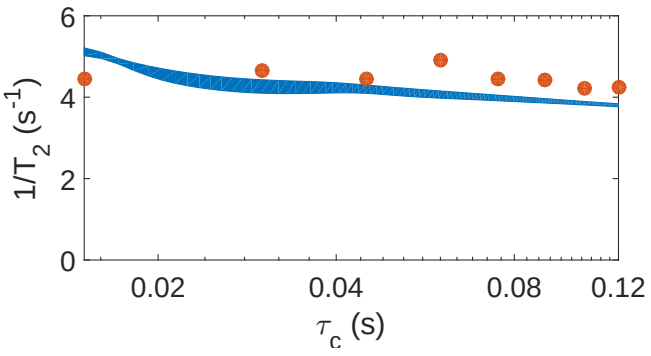

Figure 3.10: Decay rates versus UDD-3 cycle duration τ_c calculated using Eq. 3.10 for the experimental noise spectrum of 10-qubit NOON state. The dots correspond to experimental results.

3.5 Conclusions

While we are entering the era of quantum devices, noise remains a hurdle in storing quantum superpositions. Exploiting decoherence-free-subspaces (DFS) is one of the convenient ways to preserve quantum coherences. DFS is already being used for storing hyper-polarization [93], studying slow molecular dynamics [85], characterizing molecular diffusion [86, 87], precise measurements of coupling constants [130], as well as in fault-tolerant quantum computing [151]. However the noises influencing such special quantum coherences have not been hitherto characterized experimentally. In this chapter, we have experimentally characterized and compared noise spectral densities of various multi-qubit coherences.

We found that the noise spectrum of the long-lived singlet order (LLS) under spin-lock of a homonuclear spin-pair had the lowest profile indicating the strong protection offered by the symmetry in DFS resulting in long-livedness of the state. The long-lived-coherence (LLC) between singlet and the zero-quantum triplet had a higher noise profile, but still lower than the normal uncorrelated (single-spin) coherence. We have also measured the extent of noise in LLS under different field strengths and as expected, we found a higher noise with a stronger field, although the overall spectral features remained similar. On the other hand, the uncorrelated spins showed lower noise content compared to singlet states in a heteronuclear spin system, indicating an asymmetry in the system. Further, we have also explored the noise profiles of various higher-order coherences in a 10-spin system, and found a predominantly quadratic scaling of noise with

respect to coherence order. Finally, using the noise spectrum of the NOON state we predicted its decay rates under a 3rd order Uhrig dynamical decoupling sequence and verified the same with experiments.

We believe that such studies are useful for understanding the physics of noise affecting quantum systems as well as to design ways to suppress decoherence. A better understanding of noise and their suppression will be crucial not only for the physical realization of quantum devices but also for general spectroscopic applications.

CHAPTER 4

Emulation and control of quantum non-Markovian dynamics

Abstract

We experimentally emulate, in a controlled fashion, the non-Markovian dynamics of a pure dephasing spin-boson model at zero temperature. Specifically, we use a randomized set of external radio-frequency fields to engineer a desired noise power spectrum to effectively realize a non-Markovian environment for a single NMR qubit. The information backflow, characteristic to the non-Markovianity, is captured in the nonmonotonicity of the decoherence function and von Neumann entropy of the system. Using such emulated non-Markovian environments, we experimentally study the efficiency of the Carr-Purcell-Meiboom-Gill dynamical decoupling (DD) sequence to inhibit the loss of coherence. Using the filter function formalism, we design optimized DD sequences that maximize coherence protection for non-Markovian environments and study their efficiencies experimentally. Finally, we discuss DD-assisted tuning of the effective non-Markovianity.

Reported in

Deepak Khurana, Bijay Kumar Agarwalla, and T. S. Mahesh, *Experimental emulation of quantum non-Markovian dynamics and coherence protection in the presence of information back-flow*, Phys. Rev. A 99, 022107 (2019).

4.1 Introduction

Despite promising to outperform their classical counterparts by miles, quantum technologies are inherently plagued by the inevitable interactions with the surrounding environment leading to decoherence [14], which limits their utilization to full potential. At microscopic level, under certain assumptions namely weak system-environment coupling, uncorrelated initial state, and short environmental correlation times, reduced dynamics of the open quantum system (OQS) can be described by master equation of Lindblad structure with constant Lindblad operator and

positive decay rates [21, 22] (see section 1.2.3 for a little more detail about assumptions). Such dynamics is generally labeled as Markovian and corresponding dynamical map describing the evolution of reduced OQS satisfy semi-group property.

In realistic scenarios, memory effects associated with environment must be taken into consideration when these assumptions are not justified and as a consequence the corresponding dynamical map does not satisfy semi-group property. Therefore, it is essential to go beyond the Markovian description and study *non-Markovian* effects in the quantum dynamics. Unfortunately, the definition of non-Markovianity from the theory of classical stochastic process can not be transferred directly to the quantum regime [152], and a definition of quantum non-Markovianity is required, which is not based on classical notions. In this regard, several definitions of non-Markovianity exist in literature [20, 153, 154, 154, 155]. However, there is no general agreement on one definition and therefore characterization of non-Markovian dynamics is highly context dependent [154]. Moreover, these memory effects have been shown to be resources for certain quantum information tasks [156–161] which further motivate to understand the deviation of OQS dynamics from Markovian description. To this end, recently, several definitions and measures to quantify the degree of non-Markovianity have emerged [23, 162–168] from quantum information perspective. These definitions mainly rely on studying time evolution of certain information theoretical quantities under the action of the dynamical map. In this work, we use Breuer-Laine-Pilo (BLP) measure [23] which is based on distinguishability (trace distance [9]) between quantum states of OQS. Distinguishability is always contractive under the action of the Markovian dynamical map. Therefore, a momentary increase in distinguishability is a signature of non-Markovianity and physically interpreted as information back-flow from the environment. A comparative study of these measures for OQS model considered in this paper, namely pure dephasing [169] of a qubit, is carried out in Ref [170, 171]. All common definitions of non-Markovianity coincide in this case [20, 172]. However corresponding measures proposed to quantify the amount of non-Markovianity are not equivalent [170, 171]. We refer the reader to ref [20, 153] for detailed review of quantum non-Markovian dynamics.

Any rescue strategy developed to counter detrimental impact of decoherence on quantum information must be quantitatively benchmarked to ensure its robustness against various kinds of realistic environments. In this regard, non-Markovianity measure defined from quantum infor-

mation perspective enables one to study the impact of information back-flow on quantum control protocols in a more quantitative manner [173–179]. Specifically, dynamical decoupling (DD) [120, 180] is one of the most successful techniques developed in the past two decades. Efficiency of a DD sequence is related to correlation times of the environment and accordingly various DD schemes have been designed to suit the type of the environment [180–183, 183–192]. Therefore it is imperative to experimentally investigate impact of memory effects quantified using non-Markovianity measures on the efficiency of DD sequences.

To ensure a faithful benchmarking one has to reproduce effect of the environment (mainly noise spectral density) in a controlled fashion. In this regard, a systematic transition from Markovian to non-Markovian dephasing dynamics was demonstrated in photonic systems [193]. However, a full control over synthesis of noise spectral density is required for quantum control benchmarking purposes which can be achieved using artificially engineered environments [194–199].

Equipped with an elaborate control on quantum dynamics, NMR systems are excellent testbed for these kind of studies. In this chapter, using ^{1}H nuclear spins of water molecules in liquid-state NMR setup as a qubit-ensemble, we experimentally mimic the non-Markovian dynamics of a pure dephasing quantum spin-boson model via injection of classically colored noise. We utilize amplitude and phase-modulated external radio-frequency (RF) fields to produce a desired noise power spectrum [194]. The signature of non-Markovianity is captured in terms of non-monotonicity of the decay of trace distance [23] (BLP measure) and the behavior of von Neumann entropy of reduced OQS. Using engineered non-Markovian environments, we experimentally investigate the efficiency of Carr-Purcell-Meiboom-Gill (CPMG) DD sequence [142, 200] in protecting coherence. Further, using filter function formalism [188], we design optimized DD sequences that achieve a superior coherence protection for a given non-Markovian environment and study their experimental efficiency. We also indicate the potential application of DD sequences in tuning the effective non-Markovianity.

4.2 Emulation of non-Markovian dephasing dynamics

In this chapter, we consider the spin-boson pure dephasing Hamiltonian [169]

$$\mathcal{H} = \omega_0\sigma_z/2 + \sum_k \omega_k b_k^\dagger b_k + \sum_k \sigma_z(g_k b_k + g_k^* b_k^\dagger), \tag{4.1}$$

consisting of precession of a single-qubit with a frequency ω_0 and Pauli z-operator σ_z (1^{st} term), a bosonic environment with creation (annihilation) operator $b_k^\dagger(b_k)$ (2^{nd} term) and the mutual interaction with coupling constant g_k (3^{rd} term). This Hamiltonian model is exactly solvable and leads to the decay of coherences without affecting the populations. The decoherence function is of the form $\Gamma_0(t) = e^{-\chi_0(t)}$,

$$\chi_0(t) = 2\int_0^\infty d\omega J(\omega)\coth(\omega/2k_BT)\frac{\sin^2(\omega t/2)}{\omega^2}, \tag{4.2}$$

where k_BT and $J(\omega) = \sum_k |g_k|^2\delta(\omega-\omega_k)$ describe the thermal energy and the spectral density of the environment respectively. In absence of initial system-environment correlation, the reduced density matrix of OQS in the interaction picture follows a master equation with a single Lindblad operator

$$\dot{\rho} = \Phi_t\rho = \gamma_0(t)[\sigma_z\rho(t)\sigma_z - \rho(t)], \qquad \gamma_0(t) = -\dot{\Gamma}_0(t)/\Gamma_0(t)$$

The dynamical map Φ_t leads to non-Markovian dynamics as decay rate $\gamma_0(t)$ becomes negative for some $t \geq 0$ depending upon temperature and spectral density of the environment. This holds according to all common definitions of non-Markovianity [20, 172] as pointed out earlier. However various measures of non-Markovianity are not equivalent [170, 171]. Here we use the one based on the contractive property of trace distance

$$\mathcal{D}(\rho_1, \rho_2) = ||\rho_1 - \rho_2||/2,$$

where $||\rho|| = \text{Tr}(\sqrt{\rho^\dagger\rho})$ [9]. Under a Markovian dynamical map $\Phi : \rho(0) \to \rho(t)$, the trace distance is always contractive, i.e.,

$$\mathcal{D}(\rho_1(t), \rho_2(t)) \leq \mathcal{D}(\rho_1(0), \rho_2(0))$$

for all pairs of initial states $\{\rho_1(0), \rho_2(0)\}$. Here, the equality holds for the evolution under a unitary map. On the other hand, a dynamical map is non-Markovian if there exists a pair of initial states for which the trace distance shows a non-monotonic behavior. Such a non-monotonicity of the trace distance is associated with information back-flow from the environment [20, 23, 153]. Accordingly, the BLP measure [23] of non-Markovianity is defined as

$$\mathcal{N} = \max_{\rho_1(0),\rho_2(0)} \int_{\sigma>0} \sigma(t)dt, \text{ where, } \sigma(t) = \dot{\mathcal{D}}(\rho_1(t), \rho_2(t)).$$

In this case non-Markovianity measure $\mathcal{N}$ is maximized for any pair of antipodal initial states on Bloch sphere [201] and $\sigma(t) = \dot{\Gamma}_0(t)$. Accordingly, non-Markovianity measure takes a simple form,

$$\mathcal{N} = \sum_k [\Gamma_0(t_k^f) - \Gamma_0(t_k^i)],$$

considering all the intervals $[t_k^i, t_k^f]$ wherein $\dot{\Gamma}_0(t) > 0$.

The reduced dynamics of OQS under spin-boson dephasing Hamiltonian (Eq. 4.1) can be emulated by considering its semi-classical limit $[\omega_0 + \xi(t)]\sigma_z/2$, where $\xi(t)$ is a stationary Gaussian stochastic process with zero mean and with a correlation function $\langle \xi(t_1)\xi(t_2)\rangle = g(t_1 - t_2)$. The Fourier transform $S(\omega)$ of time averaged $g(t)$ is called noise power spectrum which replaces $\pi J(\omega)\coth(\omega/2k_BT)$ in Eq. 4.2, so that the decoherence function in this limit reduces to

$$\chi_0^c(t) = \frac{1}{2\pi}\int_0^\infty d\omega S(\omega)|F_0(\omega, t)|^2, \tag{4.3}$$

where the free-evolution filter-function $|F_0(\omega,t)|^2 = 4\sin^2(\omega t/2)/\omega^2$. It suggests that we can

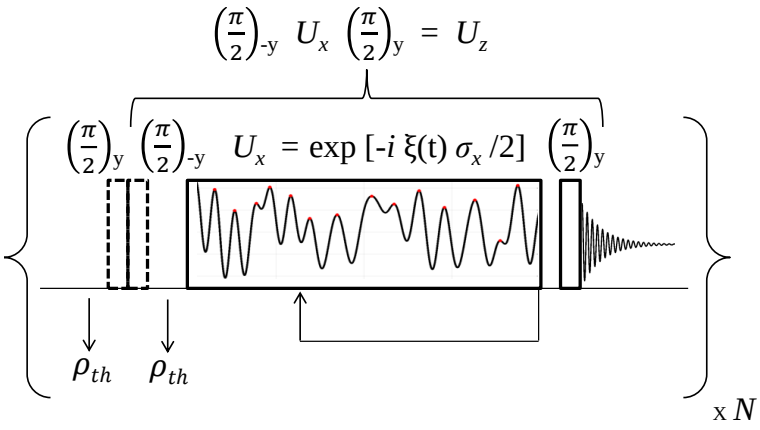

Figure 4.1: NMR pulse-sequence used to implement a non-Markovian dephasing dynamics. Here $\rho_{\rm th} = (\mathbb{I} + \epsilon\sigma_z)/2$ is the initial thermal state with purity factor ϵ. The final signal is obtained by averaging over N independent realizations of the stochastic process $\xi(t)$ as in Eq. 4.4.

mimic the non-Markovian dynamics of a single qubit coupled to a bosonic environment with a synthetic noise power spectrum. We engineer such a power spectrum via a temporal average over a set of stochastic fields of the form,

$$\xi(t) = \gamma\sum_{k=1}^{M} a(k)\cos(k\omega_b t + \phi), \tag{4.4}$$

where γ is strength of noise, $a(k)$ is the amplitude of the k^{th} Fourier component, ω_b is the base frequency, and $\phi \in [-\pi, \pi]$ is a random number with an uniform distribution. Note that though each of the realizations of $\xi(t)$ is a coherent time-dependent field and leads to unitary dynamics, a temporal average of many realizations leads to effective non-unitary dynamics. The resulting noise power spectrum is of the form [194],

$$S(\omega) = \frac{\pi\gamma^2}{2} \sum_{k=1}^{M} a^2(k)[\delta(\omega - k\omega_b) + \delta(\omega + k\omega_b)]. \tag{4.5}$$

In our experiments, we consider the spectral density

$$J(\omega) = \lambda \exp(-\omega/\omega_c)\, \omega^s/\omega_c^{s-1}, \tag{4.6}$$

where Ohmicity parameter $s = 1$, $s < 1$ and $s > 1$ corresponds to Ohmic, sub-Ohmic and super-Ohmic spectrum respectively. Comparing Eqs. 4.2, 4.6 and 4.5, we find that for spectral density mentioned above

$$a^2(k) = \frac{(k\omega_b)^s}{\omega_c^{s-1}} e^{-k\omega_b/\omega_c} \coth\left(\frac{k\omega_b}{2k_BT}\right), \quad \gamma^2 = 2\lambda, \tag{4.7}$$

which implies we can emulate pure dephasing dynamics with a non-Markovian behavior of a bosonic reservoir by properly tuning s, γ, T, and ω_c. In this chapter, we confine ourselves to zero temperature ($T = 0$) case.

The functional forms of $\mathcal{N}$ versus the dimensionless coupling constant λ and Ohmicity parameter s, have been investigated in [170, 171]. It has been shown in earlier works [170, 171, 177] that dephasing dynamics becomes BLP non-Markovian ($\mathcal{N} > 0$) for $s > 2$ and $T = 0$. Interestingly, environments corresponding to $s \leq 2$ do not give rise to non-Markovianity, according to BLP measure, despite having non-zero correlation times.

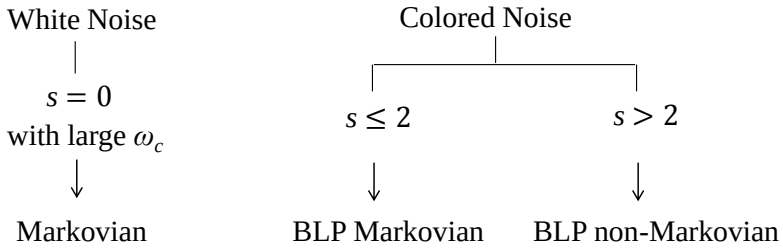

To experimentally emulate the non-Markovian dynamics, we take a NMR sample consists

of 20% H_2O in 80% D_2O, with a trace of $CuSO_4$ that shortens ^1H longitudinal and transverse relaxation times to $T_1 \approx 200$ms and $T_2 \approx 180$ms respectively. The experiments are carried out in a Bruker 500 MHz NMR spectrometer at an ambient temperature of 300 K. Here the two Zeeman levels of the spin-1/2 ^1H nucleus forms the qubit and stochastic controls required to engineer a desired $S(\omega)$ are realized by transverse radio-frequency (RF) fields whose amplitude and phase are modulated according to Eq. 4.4. The corresponding NMR pulse-sequence requires an initial $(\pi/2)_y$ pulse to prepare coherence followed by a stochastic longitudinal control field $U_z(t) = e^{-i\xi(t)\sigma_z/2}$. However, as illustrated in Fig. 4.1, $U_z(t)$ is implemented by a transverse stochastic unitary operator $U_x(t)$ sandwiched between $(\pi/2)_{-y}$ and $(\pi/2)_y$ pulses, wherein the $(\pi/2)_{-y}$ pulse is nullified with the initial $(\pi/2)_y$ pulse. Finally, an effective dephasing dynamics is achieved by temporally averaging NMR signals over $N = 1000$ independent realizations of the stochastic process $\xi(t)$ (Eq. 4.4) consisting of $M = 1000$ Fourier components.

We tuned the strength of injected noise $\lambda \in [10, 100]$, base and cut-off frequency $\omega_b = 2\pi \times 4$ rad/s and $\omega_c = 2\pi \times 320$ rad/s respectively, and the ohmicity parameter $s \in [1, 6]$ so that the signal decays out in 2.5 ms ($\approx 5\,\omega_c^{-1}$). Fig. 4.2(a) contrasts the temporal averaged signal in presence of BLP Markovian ($s = 1, \lambda = 10, \mathcal{N} = 0$) environment with the BLP non-Markovian environment ($s = 4, \lambda = 10, \mathcal{N} > 0$) with corresponding theory and numerical simulations. For the non-Markovian case, the onset of information back-flow ($\dot{\Gamma}_0(t) > 0$) occurs at about 495 μs as marked by the dashed line. In our experiments, since $\Gamma_0(t)$ decays out in 2.5 ms $\ll T_2$, the intrinsic transverse dephasing has little effect on the engineered dephasing. However, the discrepancy between the simulations and experiments is mainly due to other experimental limitations such as spatial inhomogeneity in RF pulses. The experimentally obtained non-Markovianity measure $\mathcal{N}$ versus Ohmicity parameter s (Fig. 4.2(b)) and coupling constant λ (Fig. 4.2(c)), show an overall agreement with the corresponding theoretical [170, 171] and numerical simulations. For free-evolution (Eq. 4.3), the non-Markovianity measure is almost zero for low value of Ohmicity parameter ($s \leq 2$) as well as for high values ($s > 6$), due to minimal overlap of the spectral density $S(\omega)$ with the high-frequency parts of the filter-function $|F_0(\omega, t)|^2$. For $\lambda = 10$, the maximum non-Markovianity is obtained for $s = 4.5$. Unlike the theoretical curves, the finite size of the temporal ensembles ($N = 1000$) leads to additional oscillations in experimental as well as simulated curves (Fig. 4.2(a)), resulting in an overestimation of the non-Markovianity

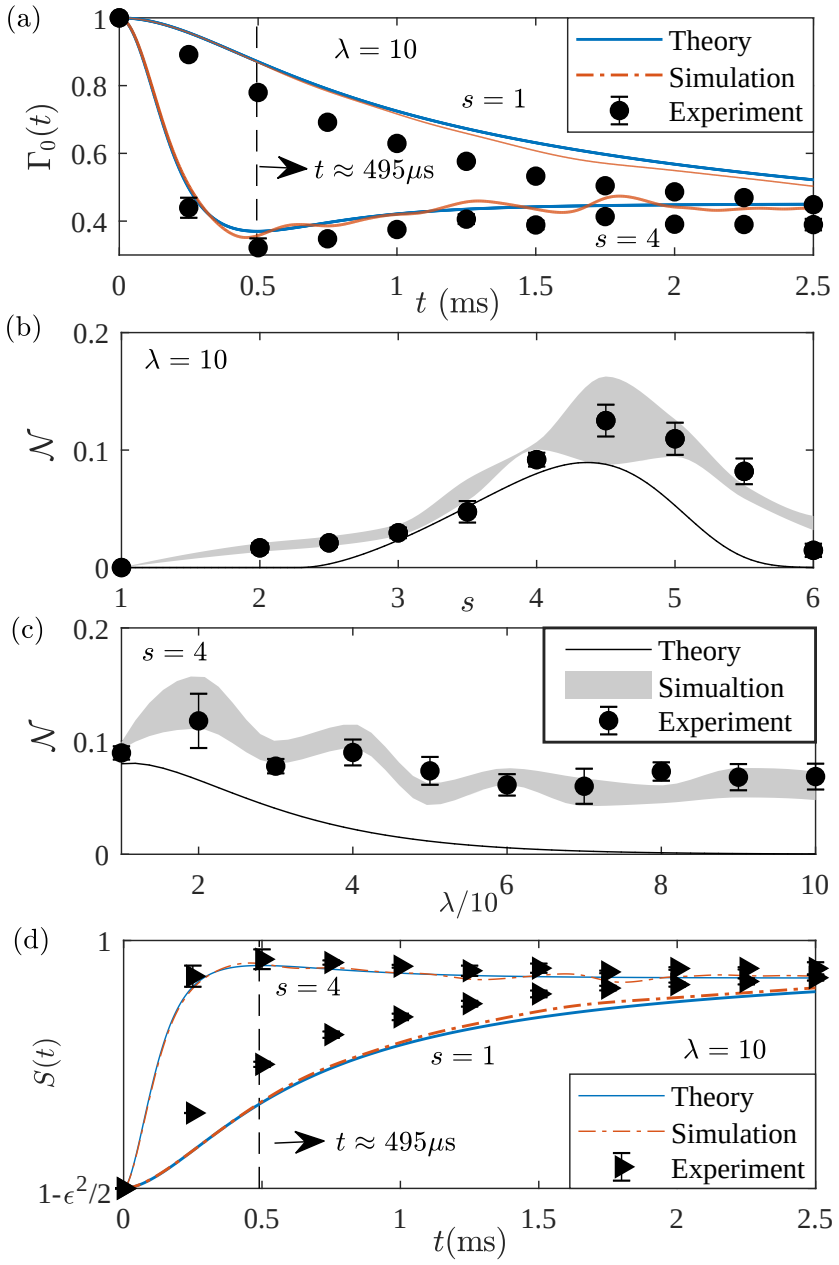

Figure 4.2: (a) Temporally averaged decoherence functions for BLP Markovian ($s = 1, \lambda = 10$) and BLP non-Markovian ($s = 4, \lambda = 10$) emulated environments. Non-Markovianity measure $\mathcal{N}$ versus (b) ohmicity parameter s for $\lambda = 10$ and (c) coupling constant λ for $s = 4$. The shaded regions for simulations and error bars in experiments correspond to standard deviations over 10 distinct bins each of 900 realizations, and they capture the finite-ensemble effects. (d) Variation of von-Neumann entropy of the system with time.

parameter $\mathcal{N}$ in Fig. 4.2(b) and (c). To this end, appropriate smoothening procedure was adopted to minimize the effect of such spurious signal oscillations (see Appendix). It is also interesting to look at von-Neumann entropy of the system $\mathcal{S}(\rho(t))$ which provides a thermodynamic perspective on the transition from Markovian to non-Markovian dynamics. As described in section 1.1.2.6, for a single qubit with an initial state $\rho = \mathbb{1}/2 + \epsilon\sigma_x/2$,

$$\mathcal{S}(\rho(t)) = -\mathrm{Tr}[\rho(t)\log_2\rho(t)] \approx 1 - \epsilon^2\Gamma_0^2(t)/2, \tag{4.8}$$

(blue-line) along with corresponding simulated (red-line) and experimental (symbols) entropies are also shown in Fig. 4.2 (d). While the monotonic growth of entropy for $s = 1$ indicates Markovian behavior, the slight drop of entropy from $t \approx 0.5$ ms for $s = 4$ is a signature of non-Markovianity.

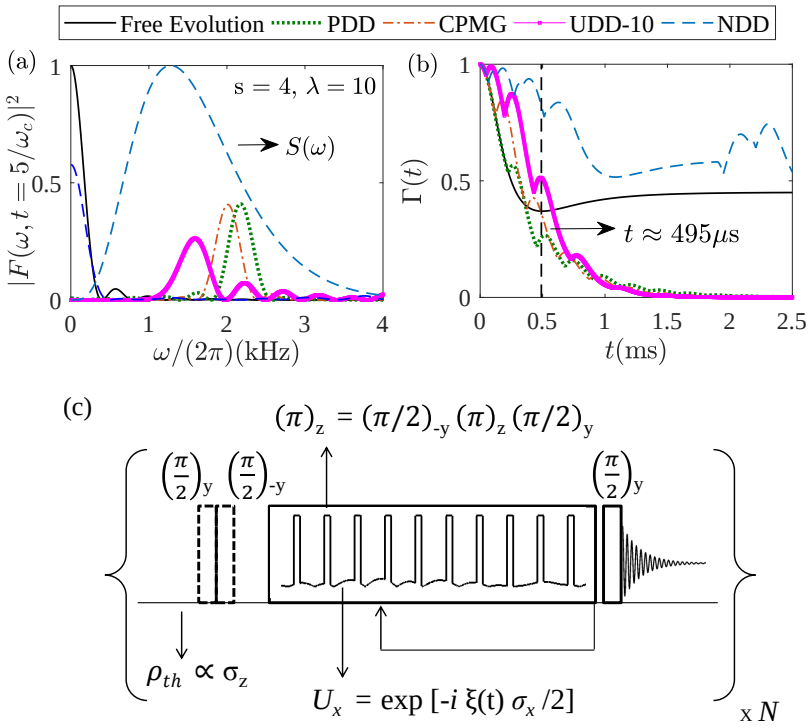

Figure 4.3: Noise spectrum (dashed line) for BLP non-Markovian environment corresponding to $s = 4$, $\lambda = 10$ and filter-functions $|F(\omega,t)|^2$ at $t = 5\ \omega_c^{-1}$ for various DD sequences as well as for free-evolution (a) and corresponding decoherence functions (b). (c) Circuit used to apply dynamical decoupling along with noise modulation.

4.3 Dynamical decoupling for non-Markovian environments

Consider a DD-protected qubit undergoing sequential phase-flips (π pulses) represented by the rectangular-wave modulation function $f(t) \in \{-1, 1\}$. In this case, the effective decoherence function $\Gamma(t) = e^{-\chi^c(t)}$, where $\chi^c(t)$ has a similar form as in Eq. 4.3, except that the filter-function is replaced with the Fourier transform,

$$F(\omega, t) = \int_0^t f(t')e^{-i\omega t'}dt'. \tag{4.9}$$

Construction of a DD sequence is based on engineering a filter-function $F(\omega, t)$ which minimizes its overlap with a given noise power spectrum $S(\omega)$, and thereby minimizes $\Gamma(t)$. Therefore, the performance of a DD sequence depends crucially on the timescale associated with the environmental correlation function. Only in case of $s = 0$ for very large value of ω_c (white noise), decay of coherence is exponential and DD sequences generally fail. In presence of BLP Markovian environments ($s \leq 2$, $\mathcal{N} = 0$), it has been theoretically shown that the PDD sequence [120] is most efficient [177] when delay between inversion pulses Δt is smaller than ω_c^{-1} as expected. However, PDD sequence becomes inefficient as non-Markovian effects become relevant ($s > 2$, $\mathcal{N} > 0$) even when $\Delta t < \omega_c^{-1}$. This can be easily understood in terms of filter function formalism as shown in Fig 4.3(a) for $\Delta t \approx 0.5\ \omega_c^{-1}$ in presence of BLP non-Markovian environment corresponding to the Ohmicity parameter $s = 4$ and the coupling constant $\lambda = 10$. Along with PDD, we also plot filter function of CPMG [142, 200] and UDD [183] sequences. Due to substantial overlap with noise spectrum with filter function, these sequences under perform for $s > 2$.

If we pack more π pulses in a given total duration, CPMG and PDD filter function peaks will move to higher frequencies, thus reducing the overlap with noise spectrum. However for a fair comparison, we keep same number of π pulses over a fixed total duration for all DD sequences. Each π pulse, instead of being an instantaneous spin flip, has in practice a finite duration, associated pulse errors, and requires certain energy output from the duty-cycle limited hardware [144, 192, 202]. For a given duration, the total number of π pulses therefore constitutes the resource required for DD.

We synthesize *non-Markovian DD-sequence* (NDD) that maximizes coherence protection parameter, $\mathcal{P} = \int_0^t dt'\Gamma(t')/t$ [177] for a known non-Markovian environment, by numerically op-

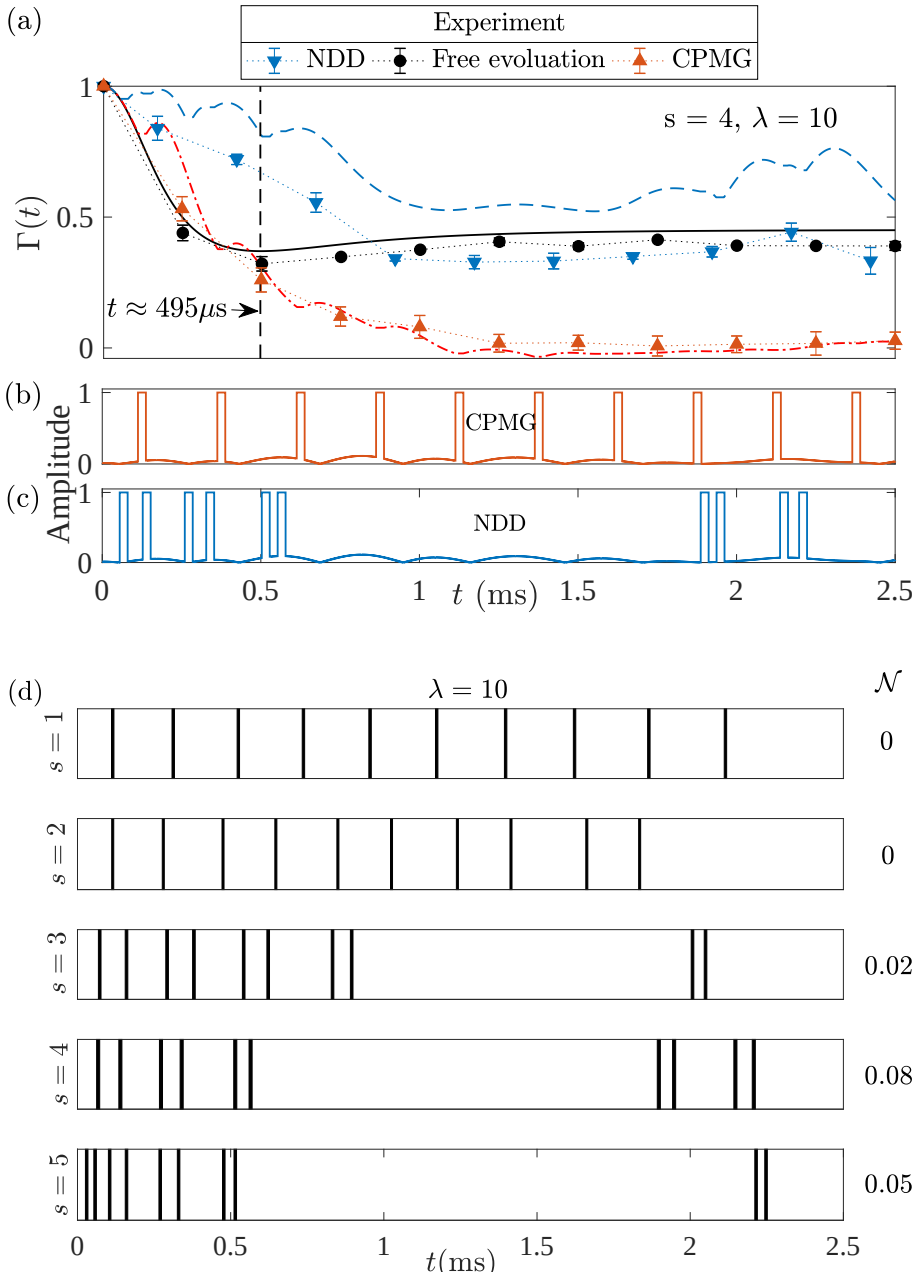

Figure 4.4: (a) Theoretical and experimental (symbols) decoherence functions with free-evolution (smooth), CPMG (dash-dot) (b), or NDD (dash) (c) sequences. In (b) and (c) one particular noise realization is interleaved with π pulses. (d) Optimal DD sequences for various ohmicity parameter $s \in \{1, 5\}$. Corresponding values of non-Markovianity measure are also indicated.

timizing the time-instants of π pulses keeping the total number of pulses (n) to be a constant. Specifically, we use genetic algorithm for optimization in this n-dimensional space where genes are delay between the π pulses. We provide CPMG as initial guess to the algorithm and optimization was constrained by the minimum delay between DD pulses, i.e., width of the DD pulse itself which was 50μs. The algorithm took up to 500 generations to reach an optimal solution. The circuit used to apply DD pulses along with noisy modulation is shown in Fig 4.3 (c). We interleave π_z pulses each of duration 50μs with the noise modulation profile for each realization and the noisy modulation is only applied during free-precession time to maintain high fidelity of π_z pulses.

Filter-functions for NDD sequence designed for BLP non-Markovian environment ($\mathcal{N} > 0$) corresponding to Ohmicity $s = 4$ with noise strength $\lambda = 10$ is shown in Fig. 4.3 (a) along with other sequences including free-evolution. Note that NDD filter-function has the minimal overlap with $S(\omega)$ indicating a better coherence protection as evident from the corresponding decoherence functions plotted in Fig. 4.3 (b). The inefficiency of other sequences can be attributed to the localization of the noise strength at the intermediate frequencies. Fig. 4.4 (a) compares the theoretical and experimental (symbols) performances of CPMG sequence (Fig. 4.4 (b)) with NDD (Fig. 4.4 (c)) and free-evolution for BLP non-Markovian environment corresponding to $s = 4$ and $\lambda = 10$. Each of the 1000 realizations for emulated environmental x-modulations (see Fig. 5.7) was interleaved with a total of ten composite π_z pulses of width 50 µs . Experimentally, the fidelity of π_z pulse was $\approx 98\%$ which indicates towards 15% radio frequency inhomogeneity. It is interesting to note that for durations less than 0.5 ms, CPMG shows faint improvement over free-evolution. However, once the information back-flow sets in, CPMG not only fails to protect the coherence, but also has a detrimental impact on it. In contrast, the NDD sequence should have a much better coherence protection as indicated by the theoretical decoherence function. Experimentally, there is a significant protection for up to 1 ms, and then the performance drops below free-evolution presumably due to finite pulse-widths, calibration errors, and other pulse-imperfections. Generation of numerous NDD sequences starting from random guesses and for various values of Ohmicity parameter $s \in \{1, 5\}$, revealed a general pattern involving bunching of π pulses at the beginning and at the end of sequences for BLP non-Markovian environments ($s > 2$). This feature explains the exclusion of filter-function at the intermediate frequencies as

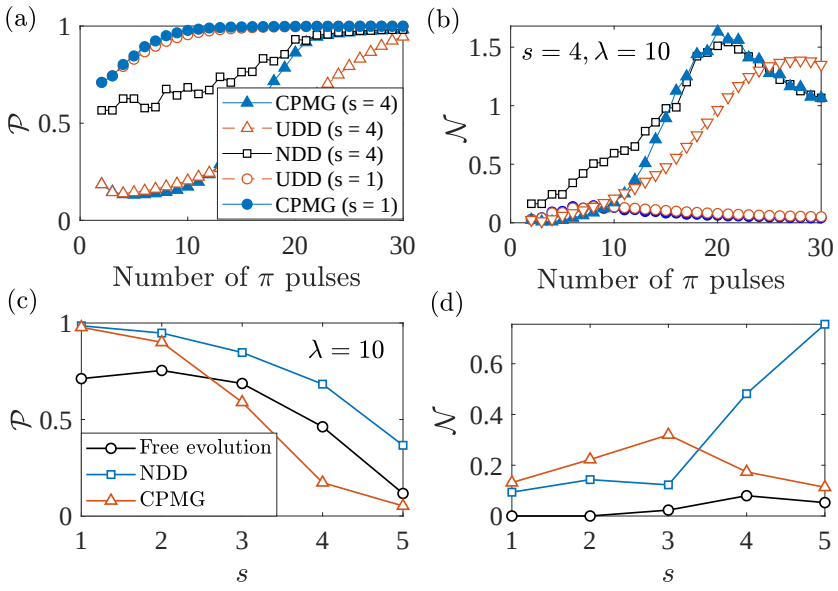

Figure 4.5: Numerically evaluated coherence protection $\mathcal{P}$ and non-Markovianity parameter $\mathcal{N}$ is plotted for various DD-sequences versus number of π pulses in (a) and (b). Same parameter plotted for various value of s under the application of CPMG, NDD as well as free evolution. NDD sequences shown in Fig. 4.4 (d) were used in this case.

observed in Fig. 4.4(a) and consequently the minimization of overlap with the spectral density. This pattern may help the NDD sequence to take advantage of the inherent information back-flow by avoiding π pulses in the intermediate time durations.

In Fig. 4.5(a) and Fig. 4.5(b), the protection parameter $\mathcal{P}$ and non-Markovianity measure $\mathcal{N}$, respectively, are plotted versus the number of π_z pulses (various Δt regimes) for CPMG, UDD and optimal NDD sequences. As expected, in the absence of information back-flow ($s = 1, \lambda = 10$), the protection parameter increases linearly before saturation, in contrast to a nonlinear behavior (before saturation) in the presence of information back-flow ($s = 4, \lambda = 10$). For high value of number of pulses (for shorter Δt) optimal solution reaches CPMG irrespective of noise spectrum (Markovian or non-Markovian). Interestingly, independent of noise spectra ($s = 1$ or $s = 4$) and the DD sequence used, the non-Markovianity measure increases with number of π pulses and starts decreasing after the protection parameter achieves the maximum value. This behavior indicates that number of spin flips can be regarded as tuning knob to engineer desired non-Markovian environments.

Since concept of DD is also associated with information back-flow, it is natural to ask the question whether there is any correlation between protection provided by optimal DD sequences

and non-Markovianity introduced by them in terms of BLP measure. In this regard, we plot parameter $\mathcal{P}$ as well as $\mathcal{N}$ for CPMG and NDD sequences as a function of Ohmicity parameter s for $\Delta t = 0.5\ \omega_c^{-1}$ and $\lambda = 10$ in Fig. 4.5 (c) and (d). Non-Markovianity is higher compared to free evolution for both CPMG and NDD sequences. However, we do not observe any clear evidence of correlation between protection and non-Markovianity.

4.4 Conclusion

In this chapter, I described experimentally emulating the non-Markovian dynamics of a pure dephasing spin boson model at zero temperature by engineering noise power spectrum with the help of a temporal averaged set of randomized external fields. We characterized the emulated non-Markovianity using BLP measure [23] and von Neumann entropy of the system. Emulating quantum non-Markovian dynamics is important not only from the fundamental point of view to understand dynamics of information back-flow [20, 23, 153, 155, 162, 171, 193] and thermodynamic properties such as flow of heat, entropy production [203–207], but also from a practical perspective of developing coherence protection protocols in presence of environmental memory effects [173, 174, 176, 177, 179]. With excellent control over quantum dynamics, we believe that NMR systems are excellent experimental test-beds to study more complex and not exactly solvable non-Markovian dynamics.

We experimentally investigated the efficiency of CPMG DD sequence in presence of non-Markovian environments with non-zero BLP measure. Moreover, using the filter function formalism [187, 188, 208–211] we designed DD sequences that optimize the position of π pulses (phase-flips) to maximize coherence protection for a specific non-Markovian environment. We observed a bunching of π pulses in the beginning and end of the sequence which hints towards exploiting information-back flow associated with non-Markovianity of dynamics. This pattern might be insightful to incorporate non-Markovianity into the optimization routines. As the number of π pulses is increased keeping the total duration fixed, the optimal sequences approach toward CPMG sequence as expected. BLP measure increases with number of π pulses till maximum protection is achieved. This aspect can be used as tuning knob to engineer non-Markovianity in a systematic fashion. We believe that our investigations constitute an important step to study impact of memory effects of environment on more involved quantum control protocols and con-

tribute towards understanding non-Markovianity as a resource for quantum technologies.

4.5 Appendix: Estimation of non-Markovianity measure $\mathcal{N}$

For emulating non-Markovian dynamics by noise power spectrum engineering using randomized control fields, a finite number of realization are possible due to experimental constraints of time required (five times longitudinal relaxation time $5 \times T_1 = 2$s) for reinitialization after every realization of $\xi(t)$. It produces oscillation artifact on top of characteristic non monotonicity of decoherence function due to non-Markovianity Fig. 4.6(a). Smoothing can not be used on time domain data directly because it can not differentiate between spurious oscillations and concerned non monotonicity. However, in Fourier domain these two can be separated since the artifact appears as noise on top of peak due to non-Markovianity in Fourier transform of $\Gamma_0(t)$ (Fig. 4.6(b)). We smoothen out these oscillation using standard data processing techniques (Fig. 4.6(c)) keeping maximum of the peak intact and then we inverse Fourier transform to get smoothened decoherence function (Fig. 4.6(d)).

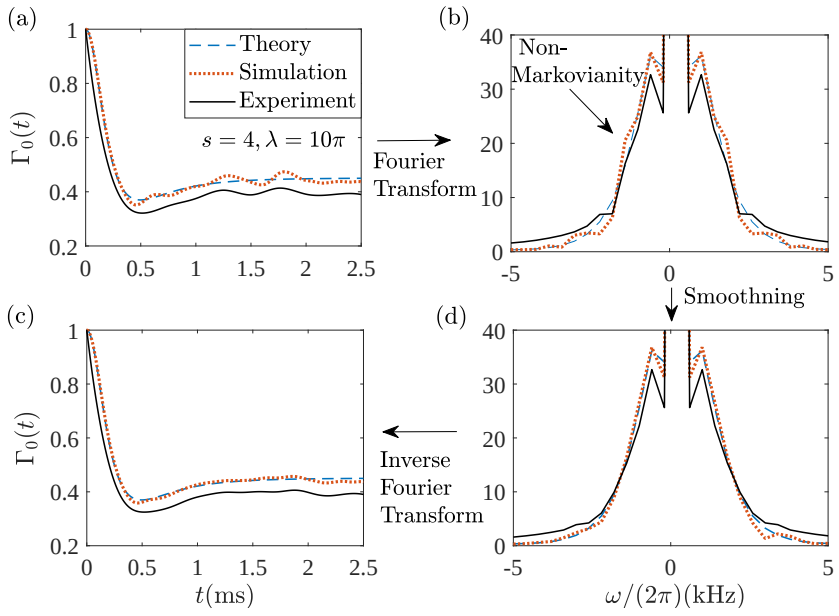

Figure 4.6: Smoothing process to estimate non-Markovianity measure $\mathcal{N}$

CHAPTER 5

Unambiguous measurement of information scrambling

Abstract

We investigate the scrambling of information in a hierarchical star-topology system using out-of-time-ordered correlation (OTOC) functions. The system consists of a central qubit directly interacting with a set of satellite qubits, which in turn interact with a second layer of satellite qubits. This particular topology not only allows convenient preparation and filtering of multiple quantum coherences between the central qubit and the first layer but also to engineer scrambling in a controlled manner. Hence, it provides us with an opportunity to experimentally study scrambling of information localized in multi-spin correlations via the construction of relevant OTOCs. Since the measurement of OTOC requires a time evolution, the non-scrambling processes such as decoherence and certain experimental errors create an ambiguity. Therefore, the unambiguous quantification of information scrambling requires suppressing contributions from decoherence to the OTOC dynamics. To this end, we propose and experimentally demonstrate a constant time protocol which is able to filter contribution exclusively from information scrambling.

Reported in

Deepak Khurana, V.R. Krithika , and T. S. Mahesh, *Unambiguous measurement of information scrambling in a hierarchical star-topology system*, arXiv:1906.02692 (2019).

5.1 Introduction

Scrambling of initially localized quantum information into many degrees of freedom via the creation of non-local correlations leads to a perceived loss of quantum information in practical time scales. In recent investigations, measurement of information scrambling has been related to many practical aspects such as diagnosis of quantum chaos [212–214], entanglement [133], detection of many-body localization [215–218], quantum phase transitions [219, 220], and thermalization

[221]. The center to all these studies is the experimentally measurable physical quantity called the out-of-time-ordered correlation (OTOC) functions [212, 213, 222]. An OTOC function is four point correlation function where the operators are not ordered in time, and its temporal decay is taken as indication of information scrambling in a many-body quantum system [223]. Despite significant theoretical investigations across condensed matter and high-energy research, experimental measurement of OTOC functions is challenging because it involves the reversal of time evolution. Several protocols such as interferometric [224, 225], quantum clock [226], and quasi-probabilities [227] are proposed. On the experimental side, early success with NMR [132, 215, 228] and ion-traps platforms [229, 230] have been reported.

In realistic scenarios, decoherence and experimental errors also contribute to the decay of OTOC, and thereby create an ambiguity in the observation of information scrambling [230, 231]. To address this issue, methods based on the use of quantum teleportation [229, 232] and OTOC quasi-probabilities [233] have been put forward recently for verified measurement of information scrambling.

Till now, experimental studies have largely focused on the investigation of scrambling of information localized in uncorrelated degrees of freedom. Recently, the scrambling of information localized in many-body correlations, such as multiple quantum coherences (MQCs) has also been reported [132]. MQCs have been used for practical purposes such as quantum sensing [131], detecting entanglement [133], noise spectroscopy [234] to name a few which makes it imperative to study the impact of scrambling on these states.

In this regard, star-topology systems are well suited for this purpose because they allow a controlled and convenient preparation of various MQCs [131, 235]. Further, if the star-topology system has multiple layers, it provides an opportunity to study scrambling of information localized in multi-spin correlations of inner layers to outer layers. Such hierarchical star-topology systems (HSTS) are important not only from the perspective of studying information scrambling but also they can be treated as a model for realistic environments to study dynamics of open quantum systems. For example, ^{15}N impurities around a nitrogen vacancy center in diamond acts the first layer and surrounding ^{13}C spins constitute the second layer [236].

In this work, using nuclear magnetic resonance (NMR) methods, we study information scrambling in a HSTS consisting of a central qubit surrounded by two layers of satellite qubits. We can

initialize the system in a desired MQC between the central qubit and the first layer. Subsequently, we drive the dynamics from the scrambling to non-scrambling regime by tuning the nonintegrability of evolution propagator. Moreover, we propose a constant time protocol (CTP) to solely capture the scrambling dynamics while disregarding the decoherence effects. Finally, we experimentally demonstrate the CTP protocol for the exclusive study of scrambling dynamics of a specific MQC.

The paper is organized as follows: In the following section, we briefly review the OTOC formalism and introduce CTP. In section III, we describe the experimental system and explain MQC preparation. In section IV, we first investigate the OTOC dynamics corresponding to various MQCs by numerical methods. Further, we describe the experimental study of the scrambling dynamics of a particular MQC using CTP. Finally, we conclude in section V.

5.2 Quantifying information scrambling: Out-of-time-ordered correlation (OTOC) function

Consider two operators $B(t)$ and $A(0)$, with commutator $C(t) = [A(0), B(t)]$ and let $C(0) = 0$. OTOC function is then defined as [212, 213, 222]

$$O(t) = \langle B^\dagger(t) A^\dagger(0) B(t) A(0) \rangle_\beta, \tag{5.1}$$

where $B(t) = U^\dagger(t) B(0) U(t)$ is evolved in Heisenberg picture with unitary operator $U(t) = e^{-i\mathcal{H}t}$ with $\hbar = 1$. Here $\mathcal{H}$ is the Hamiltonian governing the system dynamics and $\langle * \rangle_\beta = \mathrm{Tr}(* \cdot e^{-\beta\mathcal{H}})/Z$ is the average over a thermal ensemble prepared with a temperature $1/(k_B\beta)$, with k_B being the Boltzmann constant and $Z = \mathrm{Tr}(e^{-\beta\mathcal{H}})$ being the partition function. If $A(0)$ and $B(t)$ are unitaries, then the OTOC function can be related to the norm of the commutator $C(t)$ by

$$\mathcal{O}(t) = \mathrm{Re}[O(t)] = 1 - \frac{1}{2} \left\langle C^\dagger(t) C(t) \right\rangle_\beta . \tag{5.2}$$

In general, as $\mathcal{O}(t)$ evolves under the unitary operator $U(t)$, it exhibits occasional revivals to unity unless there exists a loss of information. This loss of information is either due to decoherence or due to the leakage of information via scrambling. In either case, the above commutation norm fails to vanish over time, thus preventing the OTOC revivals. However, in practice, both of these effects lead to an effective loss of OTOC revivals in practical timescales.

In the following we assume $A(0) = \rho(0)$, the initial state of the system and $B(t)$ is a unitary operator. Let us consider following two extreme cases.

(i) A pure initial state ($\rho^2(0) = \rho(0)$) corresponding to zero temperature, i.e., $\beta \to \infty$. In this case

$$\begin{aligned}\mathcal{O}(t) &= \mathrm{Re}[\langle B^\dagger(t)\rho^\dagger(0)B(t)\rho(0)\rangle_{\beta\to\infty}] \\ &= \mathrm{Re}[\mathrm{Tr}\{B^\dagger(t)\rho(0)B(t)\rho(0)\}]. \end{aligned} \tag{5.3}$$

(ii) A highly mixed qubit state corresponding to high-temperature NMR conditions, $\rho(0) = \mathbb{1}/2 + \epsilon\rho_\Delta(0)$, where the traceless part $\rho_\Delta(0)$ is often termed as the deviation density matrix. Here $\epsilon \propto \beta \simeq 0$ is the purity factor. Now,

$$\begin{aligned}\mathcal{O}(t) &= \mathrm{Re}[\langle B^\dagger(t)\rho^\dagger(0)B(t)\rho(0)\rangle_{\beta\to 0}] \\ &\sim \mathrm{Re}[\mathrm{Tr}\{B^\dagger(t)\rho_\Delta(0)B(t)\rho_\Delta(0)\}], \end{aligned} \tag{5.4}$$

up to ϵ^2 factor and a constant background (see Appendix A).

Moreover, if $B^\dagger(t) = U(t)$ is the evolution propagator, then

$$\mathcal{O}(t) = \langle\rho(t)|\rho(0)\rangle \;\text{ or }\; \langle\rho_\Delta(t)|\rho_\Delta(0)\rangle \tag{5.5}$$

as is relevant. Thus in this setting, $\mathcal{O}(t)$ can be measured by the overlap between the instantaneous state with the initial state.

5.3 Unambiguous measurement of OTOC

In order to perform an exclusive study of scrambling, it is important to separate the decoherence effects. To this end, certain protocols based on OTOC quasi probabilities [227, 233] and quantum teleportation [229, 232] have been proposed. In the following we propose an alternate approach based on the constant-time protocol (CTP) (illustrated in Fig.5.1) commonly used in multi-dimensional NMR spectroscopy [237].

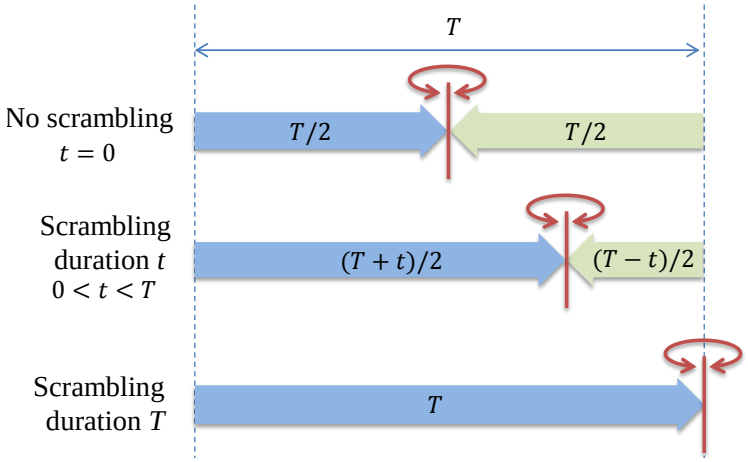

Figure 5.1: Schematic illustration of CTP protocol. The blue and green bars indicate forward and backward evolutions respectively. While decoherence is active throughout the duration T, scrambling is active only for the net forward evolution time t.

We decompose the time-evolution unitary operator $U(t)$ into two parts,

$$\begin{aligned} U(t) &= e^{-i\mathcal{H}t} \\ &= e^{i\mathcal{H}(T-t)/2} e^{-i\mathcal{H}(T+t)/2} \\ &= U^{\dagger}\left(\frac{T-t}{2}\right) U\left(\frac{T+t}{2}\right). \end{aligned} \tag{5.6}$$

Thus scrambling under the unitary operator effectively happens only for time t, but the decoherence is active throughout the total time T. Hence by carrying out multiple experiments by varying t for an experimentally feasible fixed T, one can reconstruct unambiguous evolution under scrambling Hamiltonian. This protocol can be incorporated in all the standard OTOC measurement methods [132, 133, 224–228, 230].

5.4 Hierarchical star topology system (HSTS)

In this work, we consider an N-qubit HSTS with a central qubit surrounded by N_1 qubits in the first layer and N_2 qubits in the second layer. Specifically, the experimental NMR system consists of a ^{31}P spin surrounded by a layer of six equivalent ^{1}H spins. Each of ^{1}H spin is further coupled to three ^{19}F spins in the second layer, as shown in Fig 5.2. Such a system allows us to explore controlled scrambling of information stored in correlations of the central qubit with the first layer to the second layer.

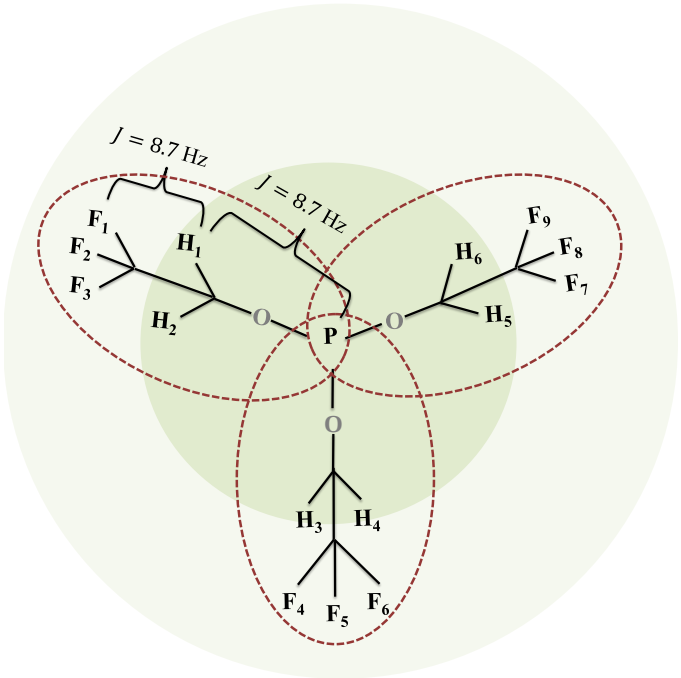

Figure 5.2: Molecule structure of tris(2,2,2-trifluoroethyl) phosphite. One ^{31}P spin, six ^{1}H spins and nine ^{19}F spins act as central spin, first and second layer respectively. Each branch constitutes one ^{31}P spin, two ^{1}H spins and three ^{19}F spins.

Let $\hbar = 1$, $\alpha \in \{x, y, z\}$, and σ_α^P, $\sigma_{i\alpha}^H$ and $\sigma_{j\alpha}^F$ be Pauli-α operators for ^{31}P, ith ^{1}H and jth ^{19}F respectively. We also define the collective terms

$$H_\alpha = \sum_{i=1}^{N_1} \sigma_{i\alpha}^H \quad \text{and} \quad F_\alpha = \sum_{j=1}^{N_2} \sigma_{j\alpha}^F.$$

The Hamiltonian of a K-branch system can be written as a sum of internal interactions and external fields,

$$\mathcal{H}_K = \sum_{k=1}^{K} \mathcal{H}_{\text{int}}^{(k)} + \mathcal{H}_{\text{ext}}^{(k)} + \sum_{\alpha \in x,z} \sigma_\alpha^P. \tag{5.7}$$

The branch-wise decomposition of the Hamiltonian is convenient for numerical simulations of OTOC dynamics with partial system size. Here the kth branch internal interaction Hamiltonian is

$$\mathcal{H}_{\text{int}}^{(k)} = \frac{\pi J}{2} \left(\sum_{i=1}^{2} \sigma_z^P \sigma_{mz}^H + \sum_{i=1}^{2} \sum_{j=1}^{3} \sigma_{mz}^H \sigma_{nz}^F \right), \tag{5.8}$$

where $m = 2(k-1) + i$ and $n = 3(k-1) + j$. Thus, in each branch, the central ^{31}P spin is coupled to two ^{1}H spins and each ^{1}H spin is further coupled to three ^{19}F spins. In our system,

$J = 8.7$ Hz happens to be the single scalar coupling constant.

The external Hamiltonian $\mathcal{H}_{\text{ext}}^{(k)}$ on the kth branch constitutes the application of equal amplitudes gJ of x and z fields employed to introduce non-integrability in the dynamics:

$$\mathcal{H}_{\text{ext}}^{(k)} = \frac{gJ\pi}{2} \sum_{\alpha \in x,z} \left(\sum_{i=1}^{2} \sigma_{m\alpha}^{H} + \sum_{j=1}^{3} \sigma_{n\alpha}^{F} \right). \tag{5.9}$$

The impact of system size and decoherence for such as HSTS are discussed in Appendix B.

5.5 Preparing Multiple quantum coherences (MQCs) in HSTS

Now we describe the preparation of combination MQCs between the central qubit and the first layer. Suppose the central spin ^{31}P is initialized in $|\pm\rangle^P = (|0\rangle^P \pm |1\rangle^P)/\sqrt{2}$ and the surrounding ^{1}H spins are in the state

$$|\xi_n^{N_1}\rangle = |N_1 - n, n\rangle^H \tag{5.10}$$

indicating $N_1 - n$ spins in $|0\rangle$ state and $n \in [0, N_1]$ spins in $|1\rangle$ state. We now apply a CNOT gate

$$U_c = \left\{ (|0\rangle\langle 0|)^P \otimes \mathbb{1}^H + (|1\rangle\langle 1|)^P \otimes H_x \right\} \otimes \mathbb{1}^F = U_c^\dagger \tag{5.11}$$

with central ^{31}P spin as the control and surrounding ^{1}H spins as target. The resulting state is

$$\rho_q^{\pm}(0) = |\psi_q^{\pm}\rangle\langle\psi_q^{\pm}| \otimes \mathbb{1}^F / 2^{N_2} \tag{5.12}$$

with

$$|\psi_q^{\pm}\rangle = \frac{|0\rangle^P |\xi_n^{N_1}\rangle \pm |1\rangle^P |\xi_{N_1-n}^{N_1}\rangle}{\sqrt{2}}, \tag{5.13}$$

which represents a combination MQC with quantum number

$$q = N_1 - 2n + 1. \tag{5.14}$$

In the following section, we describe scrambling of information out of these MQCs.

5.6 Scrambling dynamics of combination MQCs

Following the discussion preceding Eq. 5.4, we choose

$$\rho_\Delta(0) = \rho_q^x(0) = \rho_q^+(0) - \rho_q^-(0). \tag{5.15}$$

Therefore, we consider the unambiguous study of OTOC dynamics with the following operators:

$$\begin{aligned} A(0) &= \rho_q^x(0) \text{ and} \\ B(t) &= U^\dagger(t). \end{aligned} \tag{5.16}$$

In this case, the OTOC function becomes

$$\begin{aligned} \mathcal{O}_q(t) \approx & \text{Re}\left[\langle B^\dagger(t)A^\dagger(0)B(t)A(0)\rangle_{\beta=0}\right] \\ &= \text{Tr}\{U(t)\rho_q^x(0)U^\dagger(t)\ \rho_q^x(0)\} \\ &= \text{Tr}\{\rho(t)\rho_q^x(0)\}. \end{aligned} \tag{5.17}$$

The propagator $U(t)$ involves all the spins including those in the second layer and may lead to an effective leakage of coherence from the initial q-quantum combination MQC subspace as shown schematically in Fig. 5.3. In this regard, we observed via numerical simulations that under Hamiltonian considered in this work (Eq. 5.7), the leakage predominantly happens to second layer instead of other combinational MQCs. In Fig. 5.4, we plot this leakage measured using quantity $\text{Tr}[\rho(t)(F_x + F_y)]$, where $\rho(t) = U(t)\rho_{-1}^x U^\dagger(t)$ for various values of g which becomes more and more irregular as g increases.

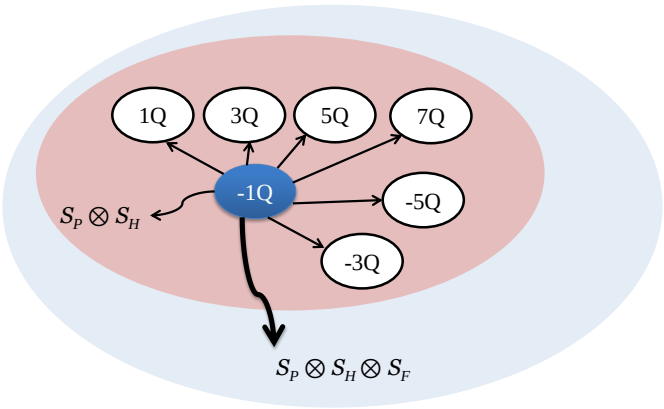

Figure 5.3: Leakage of information localized in MQC subspace corresponding to $q = -1$, i.e, $\rho_{-1}^x(0)$. Here S_P, S_H and S_F represent Hilbert spaces corresponding to ^{31}P, ^{1}H and ^{19}F spins respectively. Quantitative analysis is shown in Fig. 5.4.

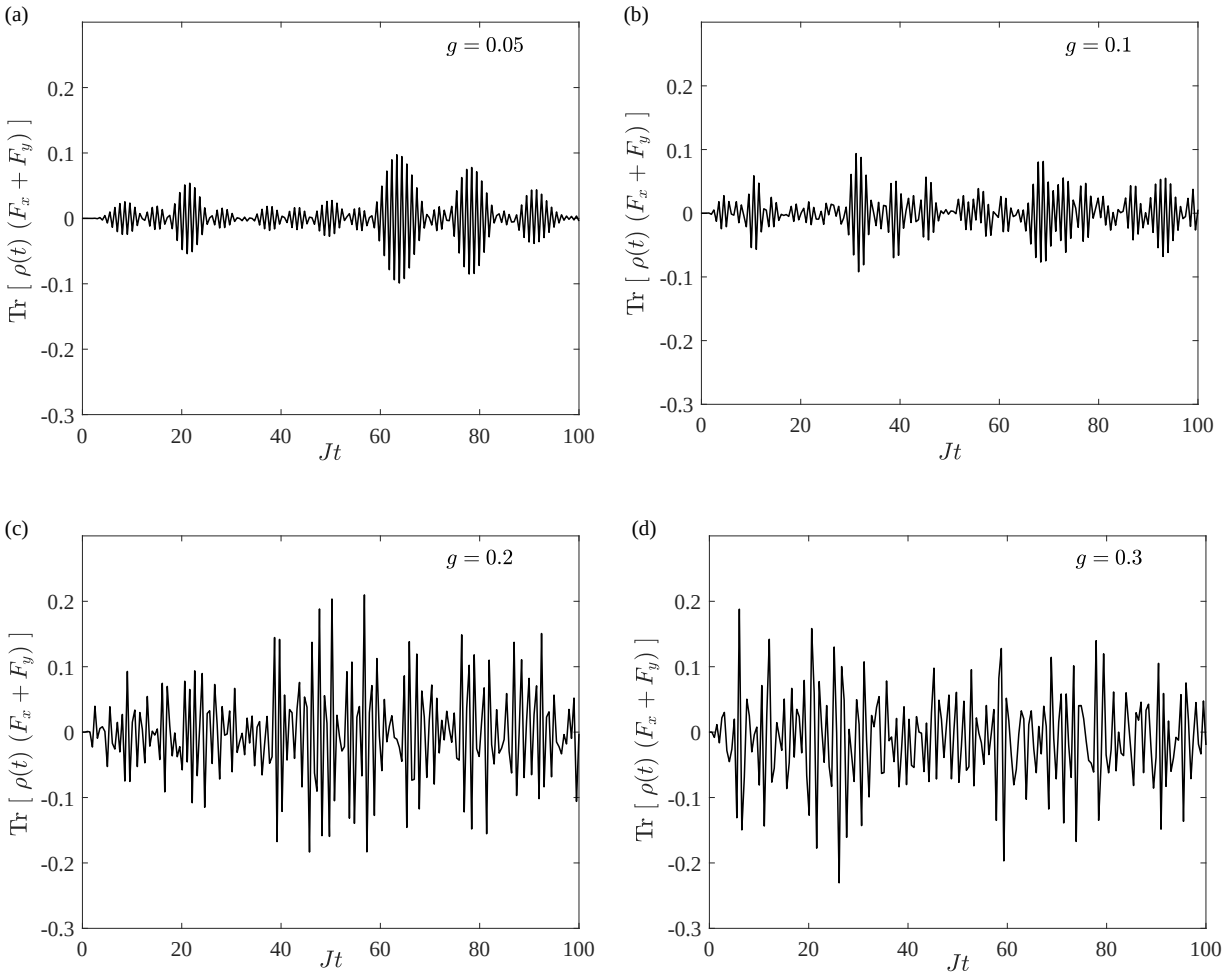

Figure 5.4: Leakage of information stored in MQC subspace corresponding $q = -1$ to the second layer measured using overlap $\mathrm{Tr}[\rho(t)(F_x + F_y)]$, where $\rho(t) = U(t)\rho_x^{-1}(0)U^\dagger(t)$.

5.6.1 Numerical simulations

We have performed the following numerical simulations to gain more insight into the scrambling dynamics of combination MQCs. Considering the computational cost, we simulated only the partial system with $K = 2$ in the Hamiltonian given in Eq. 5.7. Here no decoherence is introduced, and the observed effects are only due to the scrambling dynamics.

Fig. 5.5 displays the simulated OTOC for various coherence orders q and Jt for various g values. For the case $g = 0$, the dynamics is integrable, as shown in Fig. 5.5(a). In this case, the OTOC function shows periodic oscillations for all the MQCs, without any effective decay, suggesting no information scrambling. Note that the profiles of $q = 5$ and $q = -3$ match exactly. This is because, the corresponding states $|\psi_5\rangle$ and $|\psi_{-3}\rangle$ differ only by the state of the central

qubit which does not evolve under the scrambling Hamiltonian in the absence of the external fields. Similarly, $q = 3$ and $q = -1$ also match for the same reason.

However, once the external fields are applied, i.e., $g > 0$, the dynamics becomes non-integrable. In this case, the OTOC oscillations become nonperiodic, as shown in Figs. 5.5(b-d). More importantly, the OTOC profiles now suffer from effective decays due to a gradual loss of information out of the MQC $\rho_q^x(0)$. In fact, the stronger the strength g of the external fields, the more efficient is the scrambling. This dependence of scrambling with nonintegrability of dynamics has also been noted earlier [228] in the context of a spin chain.

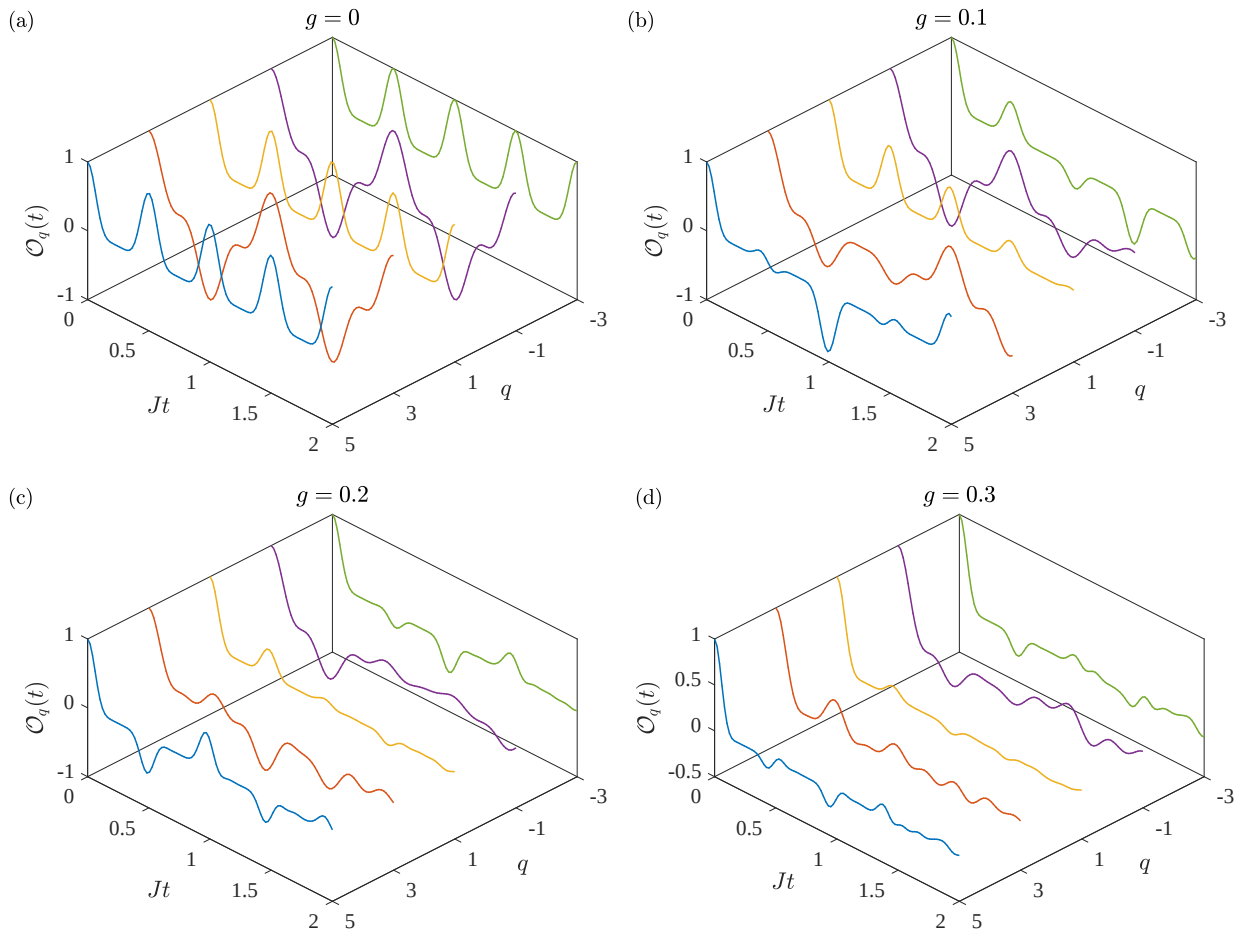

Figure 5.5: Simulated time evolutions of OTOC functions (normalized) for combination MQCs of coherence orders $q \in \{-3, -1, 1, 3, 5\}$ for (a) $g = 0$, (b) $g = 0.1$, (c) $g = 0.2$, and (d) $g = 0.3$. All the simulations are carried out for a two-branch HSTS ($K = 2$). Here no additional decoherence is introduced and all the decays are purely due to the information scrambling.

Further insight can be obtained by looking at the frequency profiles of OTOC functions. Fig. 5.6(e-h) display Fourier transforms $\mathcal{F}(\mathcal{O}_q(t))$ for various combination MQCs at different g val-

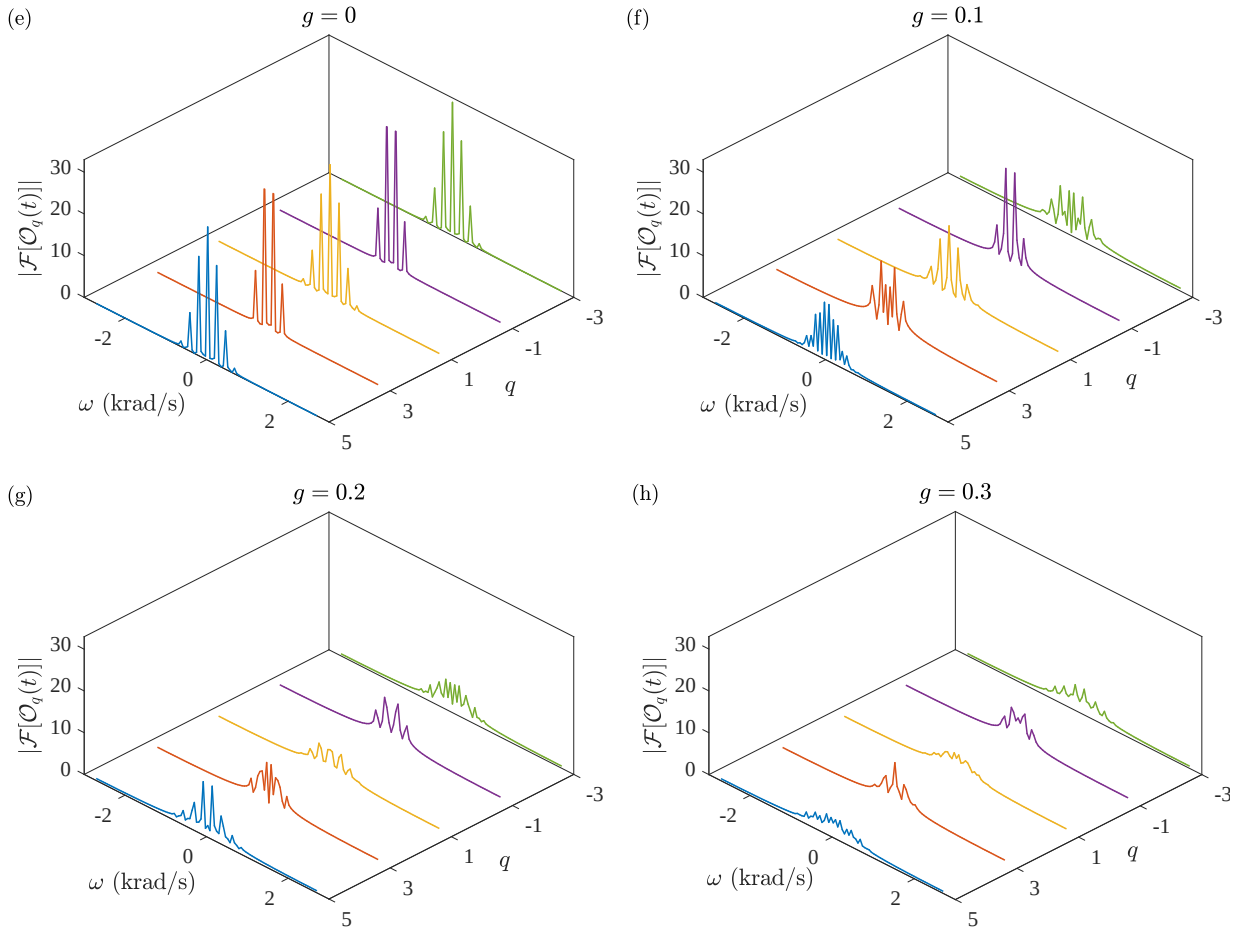

Figure 5.6: Corresponding Fourier transforms $\mathcal{F}[\mathcal{O}(t)]$ of OTOC time domain profile shown in Fig. 5.5.

ues. At $g = 0$, the spectral lines are sharp, indicating finite frequency components. However, as we introduce the external fields, i.e., for $g > 0$, we find the emergence of more frequency components, which indicates a stronger leakage of information leading to more efficient scrambling. As g increases further, we observe an effective smoothening of frequency profiles. At this point, the time domain decay profiles appear almost exponential decays, and therefore, it becomes hard to differentiate them from decoherence induced decays. This fact emphasizes the importance of CTP in practical situations. Further analysis of dependence of long time average of OTOC on coherence order is described in Appendix C.

In the next subsection, we experimentally apply CTP to reveal information scrambling for filtered combination quantum coherence $q = -1$.

5.6.2 Experiments

The NMR experiments were carried out in a Bruker NMR spectrometer with a static field of 11.2 T. As described in section III, the sample consisted of tris(2,2,2-trifluoroethyl) phosphite (see Fig. 5.2) dissolved in deuterated dimethyl sulphoxide (0.05 ml in 0.5 ml). The sample was maintained at an ambient temperature of 298 K. The ^{31}P NMR spectra corresponding various filtered MQCs along with a reference spectrum are shown in Fig. 5.7(a). Each transition is labeled by spin states $|\xi_n^{N_1}\rangle$ of the ^{1}H spins.

The experimental protocol is described schematically in Fig. 5.7 (b). Starting from thermal equilibrium, we prepare $\rho_q^x(0)$ (see Eq. 5.15) using a $(\pi/2)_y$ pulse on ^{31}P followed by a CNOT gate U_c. Note that the CNOT gate is applied in parallel to all the ^{1}H spins exploiting the star-topology of the system. Then we use the CTP method to control the scrambling time t with fixed total time T as described in Fig. 5.1. The final state $\rho(t)$ is converted into the observable single quantum magnetization of the central spin using a second CNOT gate $U_c^\dagger = U_c$. The resulting signal is

$$\begin{aligned}
s_q^x(t) &= \mathrm{Tr}\left[(\sigma_x^P \otimes |\xi_n^{N_1}\rangle\langle\xi_n^{N_1}| \otimes \mathbb{1}^F)\, U_c^\dagger \rho(t) U_c\right] \\
&= \mathrm{Tr}\left[U_c(\sigma_x^P \otimes |\xi_n^{N_1}\rangle\langle\xi_n^{N_1}| \otimes \mathbb{1}^F) U_c^\dagger\, \rho(t)\right] \\
&= \mathrm{Tr}\left[U_c\left\{|+\rangle^P\langle+|^P \otimes |\xi_n^{N_1}\rangle\langle\xi_n^{N_1}| \otimes \mathbb{1}^F\right\} U_c^\dagger\, \rho(t)\right] \\
&\quad - \mathrm{Tr}\left[U_c\left\{|-\rangle^P\langle-|^P \otimes |\xi_n^{N_1}\rangle\langle\xi_n^{N_1}| \otimes \mathbb{1}^F\right\} U_c^\dagger\, \rho(t)\right] \\
&= \mathrm{Tr}\left[\rho_q^+(0)\rho(t)\right] - \mathrm{Tr}\left[\rho_q^-(0)\rho(t)\right] \\
&= \mathrm{Tr}\left[\rho_q^x(0)\rho(t)\right] \\
&= \mathcal{O}_q(t), \qquad (5.18)
\end{aligned}$$

where we have used Eq. 5.12 and 5.15. Thus OTOC can be directly extracted from the NMR signal $s_q^x(t)$ of the central ^{31}P spin.

The NMR pulse sequence for the preparation of the combination MQCs is shown in Fig. 5.7 (c). We start with the application of a $(\pi/2)_x$ pulse on ^{19}F spins followed by a pulsed-field-gradient (PFG) G_0 along z direction to prepare them in the maximally mixed $(\mathbb{1}/2)^{\otimes N_2}$ state. Subsequently a Hadamard gate using a $(\pi/2)_y$ is applied on ^{31}P. The CNOT operation is realized via ^{1}H-^{31}P J-coupling. During this period we refocus the interactions with ^{19}F spins

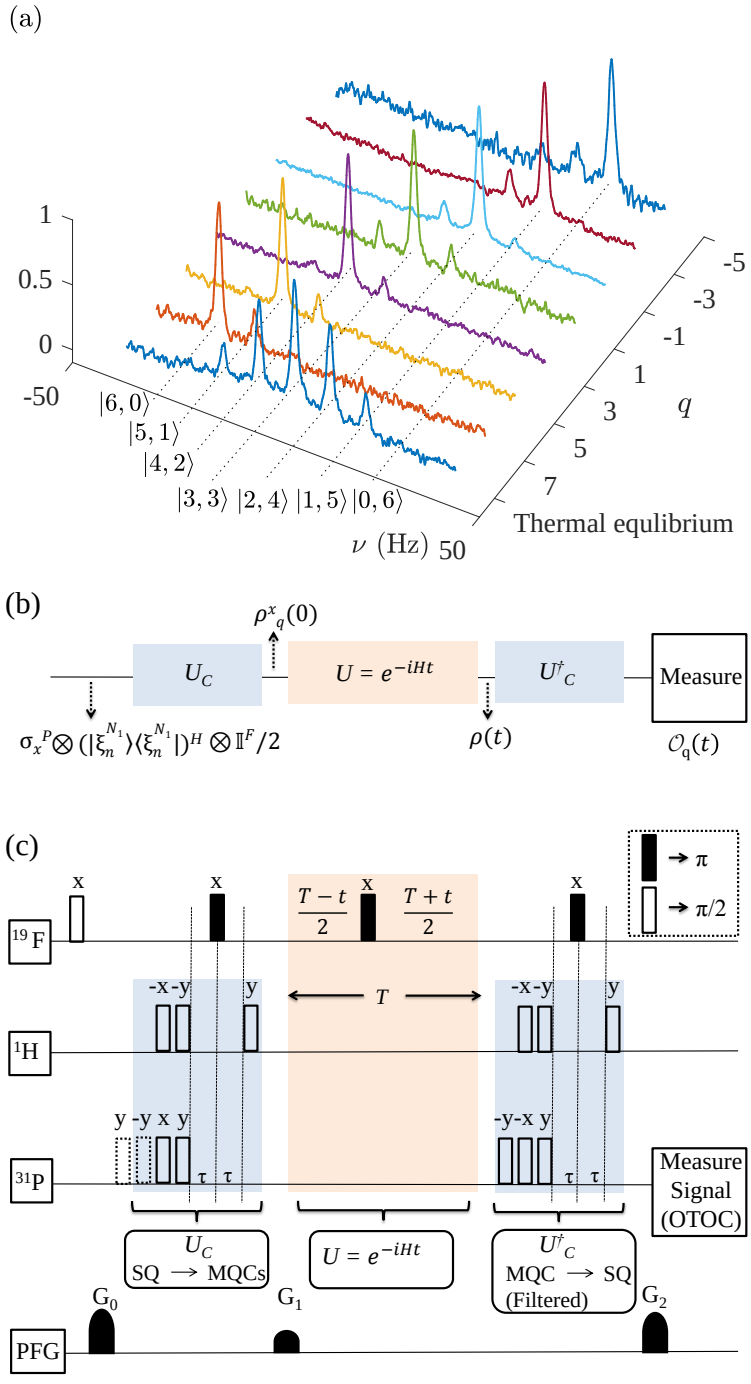

Figure 5.7: (a) A reference ^{31}P NMR spectrum (first trace) and spectra corresponding to various quantum numbers q as indicated. The transitions are labeled by corresponding states $|\xi_n^{N_1}\rangle$ of ^{1}H spins. (b) Schematic illustration of the experimental protocol to study scrambling dynamics of MQCs. (c) The NMR pulse sequence to implement the protocol in (b). The open and filled rectangles correspond to $\pi/2$ and π rotation with phases as indicated. Here PFG denotes pulse field gradients along z-direction used to select a particular coherence pathway between MQCs and SQ (single quantum coherence) and $\tau = 1/4J$ indicates evolution time under coupling Hamiltonian given in Eq. 5.8.

using a $(\pi)_x$ pulse on ^{19}F. The unambiguous study of scrambling is carried out using the CTP method as described in the previous section (see Eq. 5.6). The time-reversal step in CTP is also realized using a $(\pi)_x$ pulse on ^{19}F. We vary the time parameter t by holding the total time T constant, so that the decoherence effects are same in all the experiments, while scrambling duration is systematically varied. Finally, MQCs are converted back to an observable single-quantum coherence. A specific MQC $\rho_q^x(0)$ of a particular quantum number q is filtered out by a pair of PFGs of strengths G_1 and G_2 as shown in Fig. 5.7 (c). The ratio of the PFGs to filter the q-quantum combination MQC is set to [235]

$$\frac{G_1}{G_2} = -\frac{\gamma_P + (q-1)\gamma_H}{\gamma_P}, \tag{5.19}$$

where γ_P and γ_H are gyro-magnetic ratios of ^{31}P and ^{1}H respectively. Figs. 5.8 (a-c) display the experimentally measured OTOC functions corresponding to the quantum number $q = -1$ for various values of the nonintegrability parameter g. We have chosen $q = -1$ coherence because of its comparatively longer coherence time than the other MQCs. Fig. 5.8(a) displays OTOC evolution for $g = 0$ which belongs to the integrable regime and hence does not introduce scrambling. Here we are able to separate all three types of dynamics as follows:

(i) Only decoherence (without unitary evolution $U(t)$): It is realized by effectively nullifying the interaction between ^{1}H spins of the first layer and ^{19}F spins of the second layer using a $(\pi)_x$ pulse on ^{19}F spins at the center of the time evolution. The decay profile leads to an effective coherence time $T_2^* \simeq 140$ ms (empty squares in Fig. 5.8(a)).

(ii) Unitary dynamics along with decoherence: It is realized by allowing the interaction of ^{1}H spins with ^{19}F spins (triangles in Fig. 5.8(a)). This dynamics shows an oscillatory decay of OTOC, which in practical timescales of observation can be confused with the scrambling.

(iii) Pure unitary dynamics - realized by CTP (circles in Fig. 5.8(a)). Here we observe almost decay-less oscillations with strong revivals of OTOC confirming the absence of genuine scrambling. The higher error bars, in this case, are due to lower signal to noise ratio.

Since case (ii) is the combined effect of the case (i) and (iii), one may expect the curve with triangles to match with the product of curves with squares and circles. However, here we find an

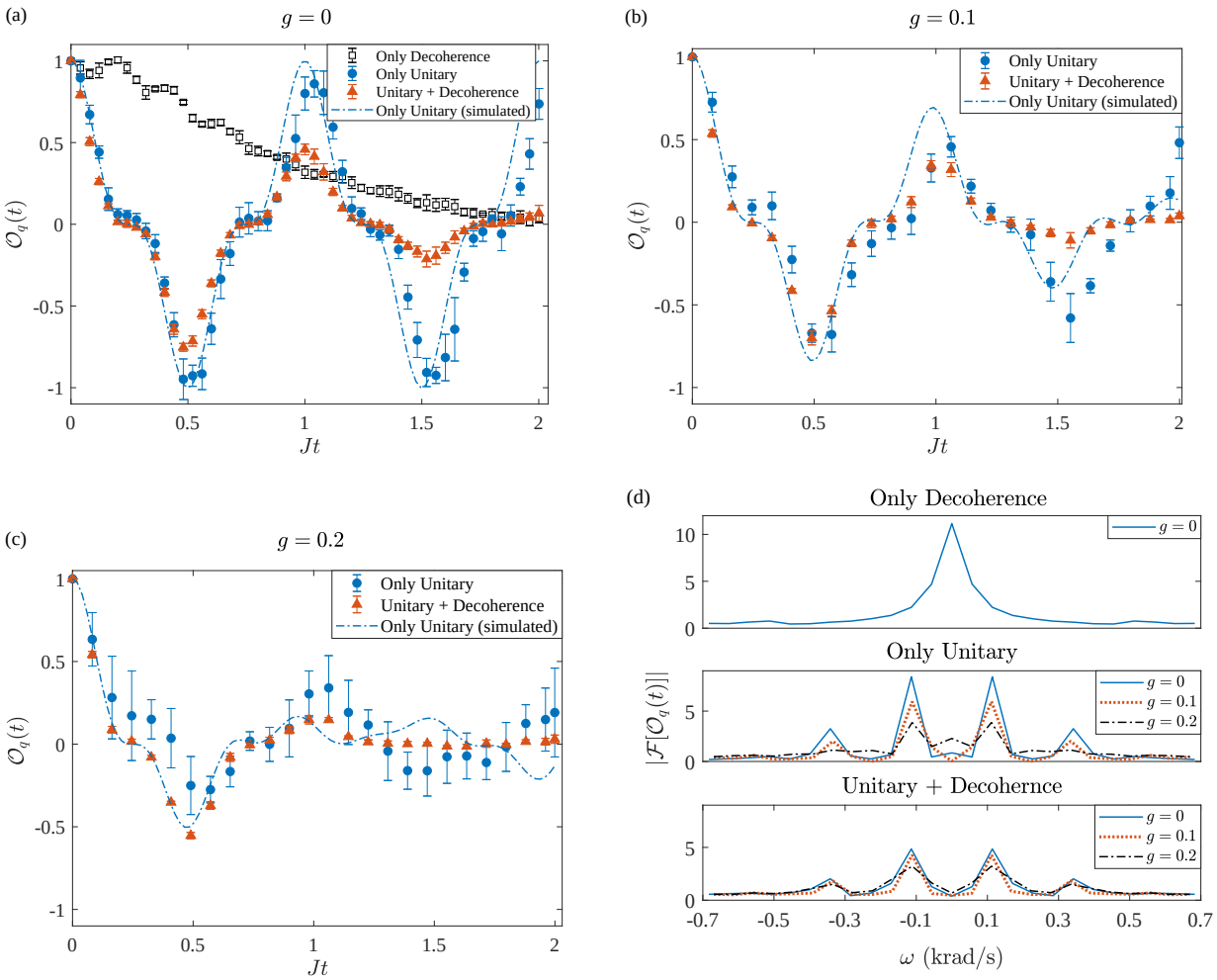

Figure 5.8: Experimentally measured OTOC (normalized) corresponding to time evolution of $q = -1$ quantum coherence in (a) integrable ($g = 0$) and (b-c) non-integrable ($g \neq 0$) regime. Dashed lines in (a-c) are obtained by numerical simulation using two-branch ($K = 2$) HSTS. Corresponding Fourier transform profiles are shown in (d).

interesting observation: the triangles over-shoot the empty squares at certain time instants (e.g. near $Jt = 1$) possibly signaling an information back-flow due to non-Markovianity [20, 153].

In Fig. 5.8(b) and (c) we show time evolution of OTOC with $g = 0.1$ and $g = 0.2$ respectively. Here the presence of external fields leads to nonintegrable dynamics and consequently exhibit information scrambling. As a result, the OTOC does not show revivals back to the initial value. One can compare the OTOC data with unitary dynamics + decoherence in (a) (triangles) with OTOC data with only unitary dynamics (circles) in (c). While both show decaying revivals, the former is devoid of scrambling while the latter is purely due to scrambling. This suggests the importance of separating the decoherence effects before quantifying scrambling. Fig. 5.8(d)

displays the Fourier transform of the OTOC data. As discussed in the previous subsection, we find broader and more dispersed spectral lines as we increase g, indicating stronger information scrambling.

Note that in our experiments, the CTP consists of a π pulse whose position is varied to refocus unitary evolution for a specific time. The successful implementation of the CTP relies upon the fact that decoherence is unaffected by the control operations during the protocol. The presence of the π pulse can refocus the slowly varying (low frequency) component of the decoherence and can cause an error in the separation of scrambling from decoherence. However, as indicated by excellent agreement of simulated and experimental data in our experiments, it seems that the π pulse does not have a drastic effect on decoherence present in our system. Still, we believe that more investigation is required into the noise spectrum of our system as well as the application of CTP protocol on other experimental platforms to further comment on this issue.

5.7 Conclusions

In this work, we have studied scrambling of information in a double layered star-topology system. This topology allows us to efficiently prepare multiple quantum coherences involving central qubit and the first layer qubits. The scrambling is introduced in a controlled manner using the tunable external fields.

A major hurdle in the unambiguous study of scrambling is to account for the contribution from decoherence to OTOC dynamics. In this regard, we proposed a constant-time protocol which enables us to filter out contribution solely from scrambling.

Using a sixteen-spin double layered star-topology NMR system, we experimentally demonstrated the unambiguous study of scrambling of information stored in the combination multiple quantum coherence involving central qubit and six satellite qubits in the first layer. With the help of constant time protocol, we could clearly separate decoherence effects and obtained OTOC profiles exclusively characterizing scrambling effects. While we observed signatures of non-Markovian evolutions, it calls for further detailed investigation in this direction.

Although the brute-force simulation of the complete system was computationally too expensive, it was nevertheless easier to tune the external field, control the scrambling rate and measure the OTOCs in the NMR spectrometer. In a way, it is a demonstration of the supremacy of quan-

tum simulations over the classical analogs. Therefore, we expect to see more applications of such star-topology systems in studying many-body phenomena because of convenient manipulation allowed by higher symmetry.

5.8 Appendix A. OTOC for highly mixed single-qubit initial state

Eq. 5.4 can be derived as follows

$$\begin{aligned}\mathcal{O}(t) &= \mathrm{Re}[\langle B^\dagger(t)\rho^\dagger(0)B(t)\rho(0)\rangle_{\beta\to 0}] \\ &= \mathrm{Re}[\mathrm{Tr}\{B^\dagger(t)\rho^\dagger(0)B(t)(\rho(0))^2\}] \\ &= \mathrm{Re}\left[\mathrm{Tr}\left\{B^\dagger(t)\left(\mathbb{1}/2+\epsilon\rho_\Delta(0)\right)B(t)\left(\mathbb{1}/2+\epsilon\rho_\Delta(0)\right)^2\right\}\right]\end{aligned}$$

The right hand side produces following six terms

$$\begin{aligned}&\frac{1}{8}\mathrm{Re}[\mathrm{Tr}\{B^\dagger(t)B(t)\}] \to \frac{1}{4} \\ &\frac{\epsilon}{2}\mathrm{Re}[\mathrm{Tr}\{B^\dagger(t)B(t)\rho_\Delta(0)\}] \to 0 \\ &\frac{\epsilon^2}{2}\mathrm{Re}[\mathrm{Tr}\{B^\dagger(t)B(t)(\rho_\Delta(0))^2\}] \to \frac{\epsilon^2}{8}\mathrm{Tr}\{(\rho_\Delta(0))^2\} \\ &\frac{\epsilon}{4}\mathrm{Re}[\mathrm{Tr}\{B^\dagger(t)\rho_\Delta(0)B(t)\}] \to 0 \\ &\epsilon^2\mathrm{Re}[\mathrm{Tr}\{B^\dagger(t)\rho_\Delta(0)B(t)\rho_\Delta(0)\}] \to * \\ &\epsilon^3\mathrm{Re}[\mathrm{Tr}\{B^\dagger(t)\rho_\Delta(0)B(t)(\rho_\Delta(0))^2\}] \to \text{negligible for } \epsilon \ll 1\end{aligned}$$

As clear from the above, only the term indicated by * has information about the OTOC dynamics. Plugging these values back, we get

$$\begin{aligned}\mathcal{O}(t) = \frac{1}{4} &+ \frac{\epsilon^2}{8}\mathrm{Tr}\{(\rho_\Delta(0))^2\} \\ &+ \epsilon^2\mathrm{Re}[\mathrm{Tr}B^\dagger(t)\rho_\Delta(0)B(t)\rho_\Delta(0)],\end{aligned} \tag{5.20}$$

Hence

$$\mathcal{O}(t) \sim \mathrm{Re}[\mathrm{Tr}\{B^\dagger(t)\rho_\Delta(0)B(t)\rho_\Delta(0)\}], \tag{5.21}$$

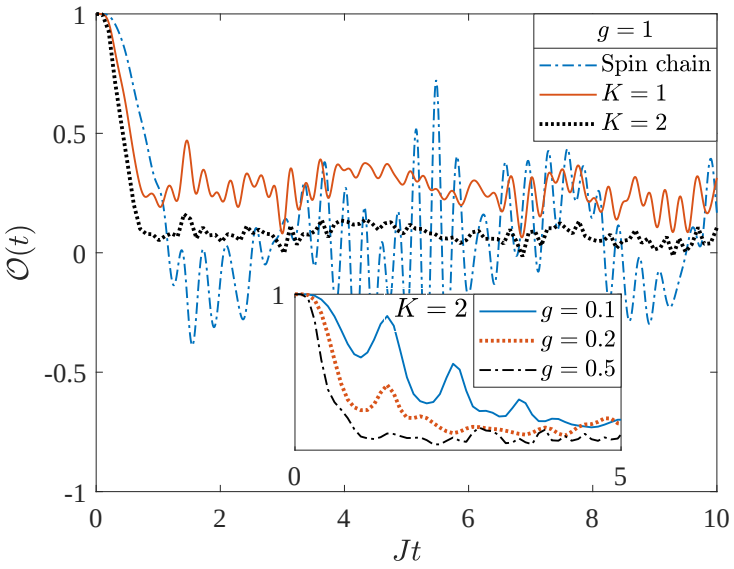

Figure 5.9: Dynamics of OTOC for the experimental system shown in Fig 5.2. Here $A(0) = \sigma_y^P$ and $B(0) = S_y^F$ with $[A(0), B(0)] = 0$. The OTOC measures scrambling of information from the central qubit to the third layer. Though evolution in the presence of both x and z field is shown, Hamiltonian gives rise to scrambling even in the absence of z field. In the inset, variation of OTOC with the nonintegrability parameter g is shown.

up to ϵ^2 factor and a constant background. It is interesting to note that, in NMR conditions, other measures of quantum correlations, such as Quantum Discord [238] and deviations in von Neumann entropy [239], are also measured in units of ϵ^2.

5.9 Appendix B. Impact of system size and decoherence

It is useful to have some idea on how the extent of scrambling scales with the size of HSTS. In this regard, we consider the scrambling of information initially localized on the central spin (Fig. 5.2) onto the N_2 spins in the second layer via N_1 spins in the first layer. To this end, we choose

$$A(0) = \sigma_y^P \quad \text{and} \quad B(t) = U^\dagger(t) S_y^F U(t).$$

Since simulating the exact dynamics of the entire system with three branches consisting of 16 spins in Fig. 5.2 is computationally expensive, we limit ourselves to partial system sizes. For the integrable regime, i.e., nonintegrability parameter $g = 0$, OTOC function remains uniformly unity since the commutator $C(t)$ vanishes at all times owing to the fact that $B(t)$ can only develop multi-spin orders with protons in the first layer with which it is directly interacting. Hence information

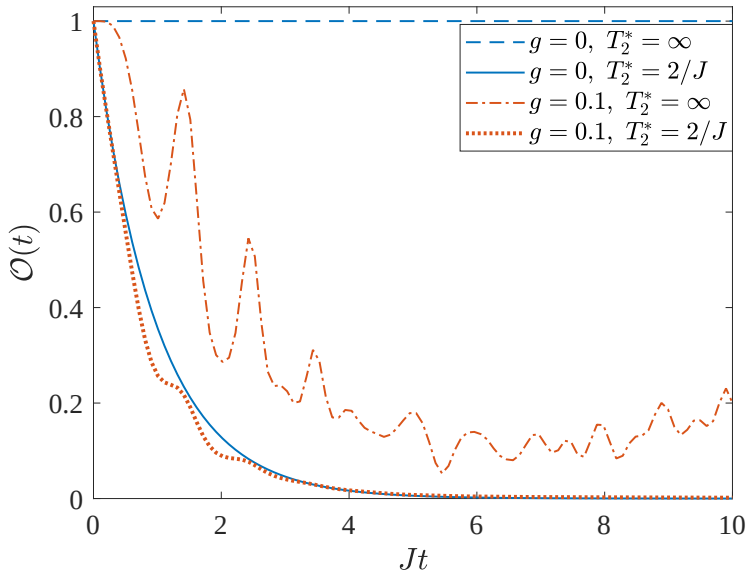

Figure 5.10: Ambiguity in the estimation of information scrambling due to the presence of decoherence simulated using two-branch HSTS.

remains localized within the first layer and never scrambled onto the second layer. Even for small values of g, OTOC function deviates from unity and starts oscillating (see the inset of Fig. 5.9). Now we set $g = 1$ and look at the dependence of scrambling on system size as shown in Fig. 5.9.

We use Lindblad based approach to simulate the combined effects of scrambling and decoherence with completely correlated dephasing model [233]. We introduce decoherence in the system by single-qubit dephasing modeled using the Lindblad equation

$$\frac{d\rho}{dt} = -i[H, \rho] + \gamma \sum_{i=1}^{N} \left(L_i \rho L_i^\dagger - \frac{1}{2}\{L_i^\dagger L_i, \rho\} \right), \tag{5.22}$$

where N is number of spins, $L_i = \sigma_z^i$ and $\gamma = 1/(2T_2^*)$ is transverse relaxation rate. To numerically simulate decoherence dynamics of OTOC, we update the density matrix in the following way

$$\begin{aligned} \rho(t) \rightarrow & \gamma dt \sum_i L_i U(dt) \rho(t) U^\dagger(dt) L_i^\dagger \\ & + L_0 U(dt) \rho(t) U^\dagger(dt) L_0^\dagger, \end{aligned} \tag{5.23}$$

where $L_0 = \sqrt{\mathcal{I} - \gamma dt \sum_i L_i L_i^\dagger}$ is no-jump operator. The above update can be interpreted as average over stochastic phase jump at each time step with probability γdt. As shown in Fig.

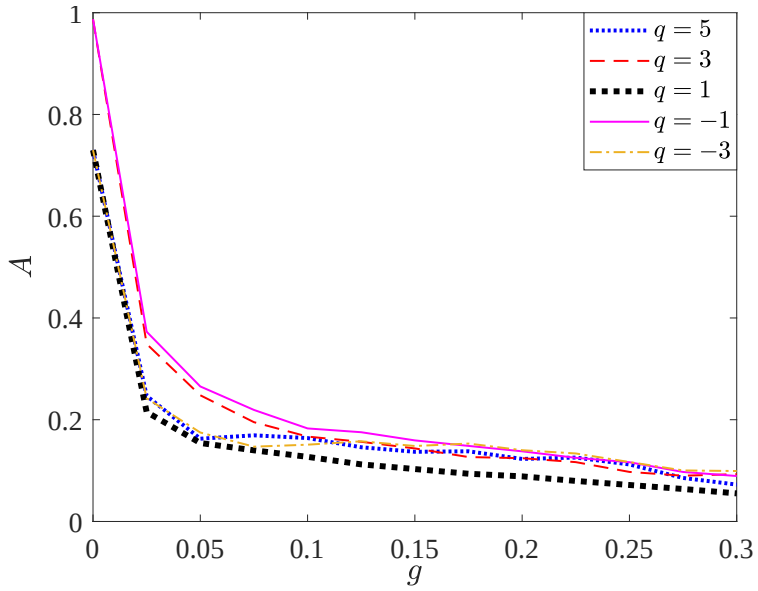

Figure 5.11: Long-time average of simulated OTOC functions vs. non-integrability parameter g for various coherence orders.

5.10, due to dephasing decay of OTOC in integrable regime almost overlaps with that of the non-integrable case for $T_2^* = 2/J$.

5.10 Appendix C. Information scrambling vs coherence order

In Fig. 5.11, we plot the long-time ($Jt = 20$) average of simulated OTOC given by

$$A = \frac{1}{t}\int_0^t |\mathcal{O}(t')|dt' \tag{5.24}$$

vs. non-integrability parameter g for various coherence orders. As described in subsection 5.6.1, $q = -3$ and $q = 5$ have same profile for $g = 0$. Same is the case for $g = 3$ and $g = -1$. However, these profile start to differ for $g > 0$ as indicated by long-time average in Fig. 5.11. The profiles get completely mixed up at higher value of g. This feature is in contrast to decoherence rate due to classical noise which shows quadratic behavior with coherence order [234]. Interestingly, coherence order $q = 1$ seems to have the most efficient scrambling.

Summary and Future Outlook

Despite holding the great promise to transform the technologies as we know today, the performance of current quantum devices is underwhelming because they are severely crippled by the presence of the environmental noise. The goal of realizing fault-tolerant devices can only be met after understanding and then suppressing the impact of the environmental noise. To this end, in this thesis, we have made an attempt to understand the information exchange between the quantum system and the surrounding environment from an experimental perspective using NMR methodologies.

In the first work, we described an optimal control method to enhance the information content inside subspaces, which are immune to major environmental noise, called long-lived singlet order (LLS) [71]. LLS is important not only from the quantum information perspective but also for spectroscopy purposes. Here we observe a considerable enhancement, and we also explore the possibility of iteratively repeating the process to increase the information content in LLS further. The iterative process did not produce any improvement due to the inability of LLS to hold information for long enough time between iteration in the NMR system considered in the work. Hence, it is a possible future direction to hunt for an appropriate NMR system where iterative enhancement can be facilitated.

The next experimental investigation was focused on the characterization of Gaussian noise affecting some special multi-qubit states, including LLS and various other multi-qubit coherences (MQCs), using quantum noise spectroscopy techniques [123, 124]. Using a two-qubit system, we observed the lowest noise profile for LLS as expected. Further, in a 10 qubit system, we could conclude that noise is predominantly correlated using noise profiles of various MQCs. However, due to no individual control over each qubit, we could only see the collective effect of all the noise sources. Hence, one future direction could be to use qubit systems with individual control on each qubit to filter out the impact of noise from each source as well as their correlations according to theoretical protocols given in Refs [127, 128]. Also, an extension to non-Gaussian noise was recently reported [134, 135] and it would be interesting to see these non-Gaussian effects of noise in NMR systems.

In the next work, we engineered non-Markovian environments [20] using stochastic control fields and experimentally quantified information backflow [23] associated with them. We also benchmarked the efficiency of protection strategies to tackle noise in the presence of information backflow. In this work, we have dealt with a single qubit case, and a natural extension would be to look at non-Markovian dynamics in a multi-qubit system where correlations among noise sources could bring about interesting features [170]. In this regard, we strongly believe that NMR could be an excellent platform for these kinds of studies as it offers stable qubits and the possibility of elaborate control over their dynamics.

In the last work, we investigated the phenomenon of information scrambling. It is a relatively new field with the potential to further our understanding of various fundamental issues related to many-body quantum systems, and only a few experimental investigations have been conducted thus far in this area. In our work, using a 16 qubit system, we analyzed scrambling of information stored in various MQC subspaces to other degrees of the freedom of the system. To conduct a verified measurement of information scrambling, we need to separate out the impact of environmental noise because both these processes lead to similar effects in the dynamics of the system [229]. To this end, we propose and experimentally demonstrate a protocol which filters out contribution only due to scrambling. One immediate future direction could be to remove the impact of experimental errors along with decoherence. Also, there is considerable theoretical progress to use information scrambling for practical purposes such as detecting entanglement [230], many-body localization [216–218] and quantum phase transition [219]. In this regard, NMR systems have already been utilized to experimentally study many-body localization [215], prethermalization [221] and open system dynamics [132] using information scrambling. Hence, it would be interesting to see more applications of the NMR systems in the experimental investigations of these many-body phenomena.

Bibliography

[1] John Preskill. Quantum computing in the nisq era and beyond. *Quantum*, 2:79, 2018.

[2] Jonathan P. Dowling and Gerard J. Milburn. Quantum technology: the second quantum revolution. *Philosophical Transactions of the Royal Society of London A: Mathematical, Physical and Engineering Sciences*, 361(1809):1655–1674, 2003.

[3] Thaddeus D. Ladd, Fedor Jelezko, Raymond Laflamme, Yasunobu Nakamura, Christopher Monroe, and J. L. O'Brien. Quantum computers. *Nature*, 464(7285):45, 2010.

[4] Christian L. Degen, Werner F. Reinhard, and Paola Cappellaro. Quantum sensing. *Reviews of modern physics*, 89(3):035002, 2017.

[5] Nicolas Gisin and Rob Thew. Quantum communication. *Nature photonics*, 1(3):165, 2007.

[6] Vittorio Giovannetti, Seth Lloyd, and Lorenzo Maccone. Advances in quantum metrology. *Nature photonics*, 5(4):222, 2011.

[7] Emanuel Knill, Raymond Laflamme, and Wojciech H. Zurek. Resilient quantum computation. *Science*, 279(5349):342–345, 1998.

[8] Heinz-Peter Breuer and Francesco Petruccione. *The theory of open quantum systems*. Oxford University Press on Demand, 2002.

[9] Michael A. Nielsen and Isaac L. Chuang. *Quantum computation and quantum information*. Cambridge university press, 2010.

[10] Richard R. Ernst, Geoffrey Bodenhausen, and Alexander Wokaun. Principles of nuclear magnetic resonance in one and two dimensions. 1987.

[11] Malcolm H. Levitt. *Spin dynamics: basics of nuclear magnetic resonance*. John Wiley & Sons, 2001.

[12] Adriano Barenco, Charles H. Bennett, Richard Cleve, David P. DiVincenzo, Norman Margolus, Peter Shor, Tycho Sleator, John A. Smolin, and Harald Weinfurter. Elementary gates for quantum computation. *Physical review A*, 52(5):3457, 1995.

[13] Robert Alicki and Karl Lendi. *Quantum dynamical semigroups and applications*, volume 717. Springer, 2007.

[14] Wojciech H. Zurek. Decoherence, einselection, and the quantum origins of the classical. *Reviews of modern physics*, 75(3):715, 2003.

[15] Thomas F. Jordan and Ennackal C. G. Sudarshan. Dynamical mappings of density operators in quantum mechanics. *Journal of Mathematical Physics*, 2(6):772–775, 1961.

[16] Ennackal C. G. Sudarshan, Piravonu M. Mathews, and Jayaseetha Rau. Stochastic dynamics of quantum-mechanical systems. *Physical Review*, 121(3):920, 1961.

[17] Man-Duen Choi. Completely positive linear maps on complex matrices. *Linear algebra and its applications*, 10(3):285–290, 1975.

[18] Robert Alicki, Daniel A. Lidar, and Paolo Zanardi. Internal consistency of fault-tolerant quantum error correction in light of rigorous derivations of the quantum markovian limit. *Physical Review A*, 73(5):052311, 2006.

[19] Karl Kraus. *States, effects and operations: fundamental notions of quantum theory*. Springer, 1983.

[20] Heinz-Peter Breuer, Elsi-Mari Laine, Jyrki Piilo, and Bassano Vacchini. Colloquium: Non-markovian dynamics in open quantum systems. *Reviews of Modern Physics*, 88(2):021002, 2016.

[21] Goran Lindblad. On the generators of quantum dynamical semigroups. *Communications in Mathematical Physics*, 48(2):119–130, 1976.

[22] Vittorio Gorini, Andrzej Kossakowski, and Ennackal C. G. Sudarshan. Completely positive dynamical semigroups of n-level systems. *Journal of Mathematical Physics*, 17(5):821–825, 1976.

[23] Heinz-Peter Breuer, Elsi-Mari Laine, and Jyrki Piilo. Measure for the degree of non-markovian behavior of quantum processes in open systems. *Physical review letters*, 103(21):210401, 2009.

[24] Fumiaki Shibata, Yoshinori Takahashi, and Natsuki Hashitsume. A generalized stochastic liouville equation. non-markovian versus memoryless master equations. *Journal of Statistical Physics*, 17(4):171–187, 1977.

[25] Subhash Chaturvedi and Fumiaki Shibata. Time-convolutionless projection operator formalism for elimination of fast variables. applications to brownian motion. *Zeitschrift für Physik B Condensed Matter*, 35(3):297–308, 1979.

[26] Michael M. Wolf and J. Ignacio Cirac. Dividing quantum channels. *Communications in Mathematical Physics*, 279(1):147–168, 2008.

[27] David P. DiVincenzo. The physical implementation of quantum computation. *Fortschritte der Physik: Progress of Physics*, 48(9-11):771–783, 2000.

[28] David G. Cory, Amr F. Fahmy, and Timothy F. Havel. Ensemble quantum computing by nmr spectroscopy. *Proceedings of the National Academy of Sciences*, 94(5):1634–1639, 1997.

[29] Lieven M. K. Vandersypen and Isaac L. Chuang. Nmr techniques for quantum control and computation. *Reviews of modern physics*, 76(4):1037, 2005.

[30] Lilian Childress and Ronald Hanson. Diamond nv centers for quantum computing and quantum networks. *MRS bulletin*, 38(2):134–138, 2013.

[31] John Clarke and Frank K. Wilhelm. Superconducting quantum bits. *Nature*, 453(7198):1031, 2008.

[32] A. Imamog, David D. Awschalom, Guido Burkard, David P. DiVincenzo, Daniel Loss, Mark Sherwin, and A. Small. Quantum information processing using quantum dot spins and cavity qed. *Physical review letters*, 83(20):4204, 1999.

[33] Leonid Fedichkin, Maxim Yanchenko, and Kamil´ A. Valiev. Novel coherent quantum bit using spatial quantization levels in semiconductor quantum dot. *arXiv preprint quant-ph/0006097*, 2000.

[34] David J. Wineland, M. Barrett, J. Britton, J. Chiaverini, B. DeMarco, Wayne M. Itano, B. Jelenković, Christopher Langer, D. Leibfried, V. Meyer, T. Rosenband, and T. Schätz. Quantum information processing with trapped ions. *Philosophical Transactions of the Royal Society of London. Series A: Mathematical, Physical and Engineering Sciences*, 361(1808):1349–1361, 2003.

[35] Walther Gerlach and Otto Stern. Das magnetische moment des silberatoms. *Zeitschrift für Physik A Hadrons and Nuclei*, 9(1):353–355, 1922.

[36] John Cavanagh, Wayne J. Fairbrother, Arthur G. Palmer III, and Nicholas J. Skelton. *Protein NMR spectroscopy: principles and practice*. Academic Press, 1995.

[37] Emanuel Knill and Raymond Laflamme. Power of one bit of quantum information. *Physical Review Letters*, 81(25):5672, 1998.

[38] David G. Cory, Mark D. Price, and Timothy F. Havel. Nuclear magnetic resonance spectroscopy: An experimentally accessible paradigm for quantum computing. *Physica D: Nonlinear Phenomena*, 120(1-2):82–101, 1998.

[39] Neil A. Gershenfeld and Isaac L. Chuang. Bulk spin-resonance quantum computation. *science*, 275(5298):350–356, 1997.

[40] Soumya S. Roy and T. S. Mahesh. Initialization of nmr quantum registers using long-lived singlet states. *Physical Review A*, 82(5):052302, 2010.

[41] Xinhua Peng, Xiwen Zhu, Ximing Fang, Mang Feng, Kelin Gao, Xiaodong Yang, and Maili Liu. Preparation of pseudo-pure states by line-selective pulses in nuclear magnetic resonance. *Chemical physics letters*, 340(5-6):509–516, 2001.

[42] Charles P. Slichter. *Principles of magnetic resonance*, volume 1. Springer Science & Business Media, 2013.

[43] Evan M. Fortunato, Marco A. Pravia, Nicolas Boulant, Grum Teklemariam, Timothy F. Havel, and David G. Cory. Design of strongly modulating pulses to implement precise effective hamiltonians for quantum information processing. *The Journal of chemical physics*, 116(17):7599–7606, 2002.

[44] Navin Khaneja, Timo Reiss, Cindie Kehlet, Thomas Schulte-Herbrüggen, and Steffen J. Glaser. Optimal control of coupled spin dynamics: design of nmr pulse sequences by gradient ascent algorithms. *Journal of magnetic resonance*, 172(2):296–305, 2005.

[45] Gaurav Bhole, V. S. Anjusha, and T. S. Mahesh. Steering quantum dynamics via bang-bang control: Implementing optimal fixed-point quantum search algorithm. *Physical Review A*, 93(4):042339, 2016.

[46] John J. L. Morton, Alexei M. Tyryshkin, Arzhang Ardavan, Simon C. Benjamin, Kyriakos Porfyrakis, S. A. Lyon, and G. Andrew D. Briggs. Bang–bang control of fullerene qubits using ultrafast phase gates. *Nature Physics*, 2(1):40–43, 2006.

[47] G. L. Long, H. Y. Yan, and Yang Sun. Analysis of density matrix reconstruction in nmr quantum computing. *Journal of Optics B: Quantum and Semiclassical Optics*, 3(6):376, 2001.

[48] Garett M. Leskowitz and Leonard J. Mueller. State interrogation in nuclear magnetic resonance quantum-information processing. *Physical Review A*, 69(5):052302, 2004.

[49] Felix Bloch. Nuclear induction. *Physical review*, 70(7-8):460, 1946.

[50] Malcolm H. Levitt. Composite pulses. *Progress in Nuclear Magnetic Resonance Spectroscopy*, 18(2):61–122, 1986.

[51] Alberto Tannús and Michael Garwood. Adiabatic pulses. *NMR in Biomedicine*, 10(8):423–434, 1997.

[52] Helen Geen and Ray Freeman. Band-selective radiofrequency pulses. *Journal of Magnetic Resonance (1969)*, 93(1):93–141, 1991.

[53] Stephen Wimperis. Broadband, narrowband, and passband composite pulses for use in advanced nmr experiments. *Journal of Magnetic Resonance, Series A*, 109(2):221–231, 1994.

[54] Thomas E. Skinner, Timo O. Reiss, Burkhard Luy, Navin Khaneja, and Steffen J. Glaser. Application of optimal control theory to the design of broadband excitation pulses for high-resolution nmr. *Journal of Magnetic Resonance*, 163(1):8–15, 2003.

[55] M. Feike, D. E. Demco, Robert Graf, J. Gottwald, S. Hafner, and Wolfgang H. Spiess. Broadband multiple-quantum nmr spectroscopy. *Journal of Magnetic Resonance, Series A*, 122(2):214–221, 1996.

[56] P. De Fouquieres, S. G. Schirmer, Steffen J. Glaser, and Ilya Kuprov. Second order gradient ascent pulse engineering. *Journal of Magnetic Resonance*, 212(2):412–417, 2011.

[57] David J. Tannor, Vladimir Kazakov, and Vladimir Orlov. Control of photochemical branching: Novel procedures for finding optimal pulses and global upper bounds. In J. Broeckhove and L. Lathouwers, editors, *Time-Dependent Quantum Molecular Dynamics*, pages 347–360. Plenum Press, New York, 1992.

[58] Wusheng Zhu and Herschel Rabitz. A rapid monotonically convergent iteration algorithm for quantum optimal control over the expectation value of a positive definite operator. *The Journal of Chemical Physics*, 109(2):385–391, 1998.

[59] Reuven Eitan, Michael Mundt, and David J. Tannor. Optimal control with accelerated convergence: Combining the krotov and quasi-newton methods. *Physical Review A*, 83(5):053426, 2011.

[60] Shlomo E. Sklarz and David J. Tannor. Loading a bose-einstein condensate onto an optical lattice: An application of optimal control theory to the nonlinear schrödinger equation. *Physical Review A*, 66(5):053619, 2002.

[61] Mads S. Vinding, Ivan I. Maximov, Zdeněk Tošner, and Niels Chr. Nielsen. Fast numerical design of spatial-selective rf pulses in mri using krotov and quasi-newton based optimal control methods. *The Journal of chemical physics*, 137(5):054203, 2012.

[62] Weiwei Zhou, S. G. Schirmer, Ming Zhang, and Hong-Yi Dai. Bang–bang control design for quantum state transfer based on hyperspherical coordinates and optimal time–energy control. *Journal of Physics A: Mathematical and Theoretical*, 44(10):105303, 2011.

[63] Luke J. Edwards, D. V. Savostyanov, Z. T. Welderufael, Donghan Lee, and Ilya Kuprov. Quantum mechanical nmr simulation algorithm for protein-size spin systems. *Journal of Magnetic Resonance*, 243:107–113, 2014.

[64] Ilya Kuprov. Spin system trajectory analysis under optimal control pulses. *Journal of Magnetic Resonance*, 233:107–112, 2013.

[65] D. L. Goodwin and Ilya Kuprov. Modified newton-raphson grape methods for optimal control of spin systems. *The Journal of chemical physics*, 144(20):204107, 2016.

[66] Marina Carravetta, Ole G. Johannessen, and Malcolm H. Levitt. Beyond the t 1 limit: singlet nuclear spin states in low magnetic fields. *Physical review letters*, 92(15):153003, 2004.

[67] Giuseppe Pileio, Marina Carravetta, and Malcolm H. Levitt. Storage of nuclear magnetization as long-lived singlet order in low magnetic field. *Proceedings of the National Academy of Sciences*, 107(40):17135–17139, 2010.

[68] Marina Carravetta and Malcolm H. Levitt. Long-lived nuclear spin states in high-field solution nmr. *Journal of the American Chemical Society*, 126(20):6228–6229, 2004.

[69] Marina Carravetta and Malcolm H. Levitt. Theory of long-lived nuclear spin states in solution nuclear magnetic resonance. i. singlet states in low magnetic field. *The Journal of chemical physics*, 122(21):214505, 2005.

[70] Giuseppe Pileio and Malcolm H. Levitt. Theory of long-lived nuclear spin states in solution nuclear magnetic resonance. ii. singlet spin locking. *The Journal of chemical physics*, 130(21):214501, 2009.

[71] Malcolm H. Levitt. Singlet nuclear magnetic resonance. *Annual review of physical chemistry*, 63:89–105, 2012.

[72] Giuseppe Pileio, Joseph T. Hill-Cousins, Sam Mitchell, Ilya Kuprov, Lynda J. Brown, Richard C. D. Brown, and Malcolm H. Levitt. Long-lived nuclear singlet order in near-equivalent 13c spin pairs. *Journal of the American Chemical Society*, 134(42):17494–17497, 2012.

[73] Giuseppe Pileio, Marina Carravetta, Eric Hughes, and Malcolm H. Levitt. The long-lived nuclear singlet state of 15n-nitrous oxide in solution. *Journal of the American Chemical Society*, 130(38):12582–12583, 2008.

[74] Meike Emondts, Micah P. Ledbetter, Szymon Pustelny, Thomas Theis, Brian Patton, John W. Blanchard, Mark C. Butler, Dmitry Budker, and Alexander Pines. Long-lived heteronuclear spin-singlet states in liquids at a zero magnetic field. *Physical review letters*, 112(7):077601, 2014.

[75] Yesu Feng, Ryan M. Davis, and Warren S. Warren. Accessing long-lived nuclear singlet states between chemically equivalent spins without breaking symmetry. *Nature physics*, 8(11):831, 2012.

[76] Puneet Ahuja, Riddhiman Sarkar, Paul R. Vasos, and Geoffrey Bodenhausen. Long-lived states in multiple-spin systems. *ChemPhysChem*, 10(13):2217–2220, 2009.

[77] Stephen J. DeVience, Ronald L. Walsworth, and Matthew S. Rosen. Preparation of nuclear spin singlet states using spin-lock induced crossing. *Physical review letters*, 111(17):173002, 2013.

[78] Giuseppe Pileio and Malcolm H. Levitt. J-stabilization of singlet states in the solution nmr of multiple-spin systems. *Journal of Magnetic Resonance*, 187(1):141–145, 2007.

[79] Michael C. D. Tayler and Malcolm H. Levitt. Singlet nuclear magnetic resonance of nearly-equivalent spins. *Physical Chemistry Chemical Physics*, 13(13):5556–5560, 2011.

[80] Jean-Nicolas Dumez, Joseph T. Hill-Cousins, Richard C. D. Brown, and Giuseppe Pileio. Long-lived localization in magnetic resonance imaging. *Journal of Magnetic Resonance*, 246:27–30, 2014.

[81] Aaron K. Grant and Elena Vinogradov. Long-lived states in solution nmr: Theoretical examples in three-and four-spin systems. *Journal of Magnetic Resonance*, 193(2):177–190, 2008.

[82] Yesu Feng, Thomas Theis, Tung-Lin Wu, Kevin Claytor, and Warren S. Warren. Long-lived polarization protected by symmetry. *The Journal of chemical physics*, 141(13):134307, 2014.

[83] Kevin Claytor, Thomas Theis, Yesu Feng, Jin Yu, David Gooden, and Warren S. Warren. Accessing long-lived disconnected spin-1/2 eigenstates through spins¿ 1/2. *Journal of the American Chemical Society*, 136(43):15118–15121, 2014.

[84] Stephen Kadlecek, Kiarash Emami, Masaru Ishii, and Rahim Rizi. Optimal transfer of spin-order between a singlet nuclear pair and a heteronucleus. *Journal of Magnetic Resonance*, 205(1):9–13, 2010.

[85] Riddhiman Sarkar, Paul R. Vasos, and Geoffrey Bodenhausen. Singlet-state exchange nmr spectroscopy for the study of very slow dynamic processes. *Journal of the American Chemical Society*, 129(2):328–334, 2007.

[86] Riddhiman Sarkar, Puneet Ahuja, Paul R. Vasos, and Geoffrey Bodenhausen. Measurement of slow diffusion coefficients of molecules with arbitrary scalar couplings via long-lived spin states. *ChemPhysChem*, 9(16):2414–2419, 2008.

[87] Simone Cavadini, Jens Dittmer, Sasa Antonijevic, and Geoffrey Bodenhausen. Slow diffusion by singlet state nmr spectroscopy. *Journal of the American Chemical Society*, 127(45):15744–15748, 2005.

[88] Giuseppe Pileio, Marina Carravetta, and Malcolm H. Levitt. Extremely low-frequency spectroscopy in low-field nuclear magnetic resonance. *Physical review letters*, 103(8):083002, 2009.

[89] Michael C. D. Tayler, Sabrina Marie, A. Ganesan, and Malcolm H. Levitt. Determination of molecular torsion angles using nuclear singlet relaxation. *Journal of the American Chemical Society*, 132(24):8225–8227, 2010.

[90] Paul R. Vasos, A. Comment, Riddhiman Sarkar, Puneet Ahuja, Sami Jannin, J-P Ansermet, J. A. Konter, P. Hautle, B. Van Den Brandt, and Geoffrey Bodenhausen. Long-lived states to sustain hyperpolarized magnetization. *Proceedings of the National Academy of Sciences*, 106(44):18469–18473, 2009.

[91] Warren S. Warren, Elizabeth Jenista, Rosa Tamara Branca, and Xin Chen. Increasing hyperpolarized spin lifetimes through true singlet eigenstates. *Science*, 323(5922):1711–1714, 2009.

[92] Giuseppe Pileio, Sean Bowen, Christoffer Laustsen, Michael C. D. Tayler, Joseph T. Hill-Cousins, Lynda J. Brown, Richard C. D. Brown, Jan H. Ardenkjaer-Larsen, and Malcolm H. Levitt. Recycling and imaging of nuclear singlet hyperpolarization. *Journal of the American Chemical Society*, 135(13):5084–5088, 2013.

[93] Puneet Ahuja, Riddhiman Sarkar, Sami Jannin, Paul R. Vasos, and Geoffrey Bodenhausen. Proton hyperpolarisation preserved in long-lived states. *Chemical Communications*, 46(43):8192–8194, 2010.

[94] Benno Meier, Jean-Nicolas Dumez, Gabriele Stevanato, Joseph T. Hill-Cousins, Soumya S. Roy, Par Hakansson, Salvatore Mamone, Richard C. D. Brown, Giuseppe Pileio, and Malcolm H. Levitt. Long-lived nuclear spin states in methyl groups and quantum-rotor-induced polarization. *Journal of the American Chemical Society*, 135(50):18746–18749, 2013.

[95] Jean-Nicolas Dumez, Pär Håkansson, Salvatore Mamone, Benno Meier, Gabriele Stevanato, Joseph T. Hill-Cousins, Soumya S. Roy, Richard C. D. Brown, Giuseppe Pileio, and Malcolm H. Levitt. Theory of long-lived nuclear spin states in methyl groups and quantum-rotor induced polarisation. *The Journal of chemical physics*, 142(4):044506, 2015.

[96] H. J. Hogben, P. J. Hore, and Ilya Kuprov. Multiple decoherence-free states in multi-spin systems. *Journal of Magnetic Resonance*, 211(2):217–220, 2011.

[97] Gabriele Stevanato, Joseph T. Hill-Cousins, Pär Håkansson, Soumya S. Roy, Lynda J. Brown, Richard C. D. Brown, Giuseppe Pileio, and Malcolm H. Levitt. A nuclear sin-

glet lifetime of more than one hour in room-temperature solution. *Angewandte Chemie International Edition*, 54(12):3740–3743, 2015.

[98] Yesu Feng, Thomas Theis, Xiaofei Liang, Qiu Wang, Pei Zhou, and Warren S. Warren. Storage of hydrogen spin polarization in long-lived 13c2 singlet order and implications for hyperpolarized magnetic resonance imaging. *Journal of the American Chemical Society*, 135(26):9632–9635, 2013.

[99] Kevin Claytor, Thomas Theis, Yesu Feng, and Warren S. Warren. Measuring long-lived 13 c 2 state lifetimes at natural abundance. *Journal of Magnetic Resonance*, 239:81–86, 2014.

[100] Gareth A. Morris and Ray Freeman. Enhancement of nuclear magnetic resonance signals by polarization transfer. *Journal of the American Chemical Society*, 101(3):760–762, 1979.

[101] Alexander Pines, M. G. Gibby, and J. S. Waugh. Proton-enhanced nuclear induction spectroscopy. a method for high resolution nmr of dilute spins in solids. *The Journal of Chemical Physics*, 56(4):1776–1777, 1972.

[102] Winneche O. Sørensen. Polarization transfer experiments in high-resolution nmr spectroscopy. *Progress in Nuclear Magnetic Resonance Spectroscopy*, 21(6):503–569, 1989.

[103] Leonard J. Schulman and Umesh V. Vazirani. Molecular scale heat engines and scalable quantum computation. In *Proceedings of the thirty-first annual ACM symposium on Theory of computing*, pages 322–329. ACM, 1999.

[104] Daniel K. Park, Nayeli A. Rodriguez-Briones, Guanru Feng, Robabeh Rahimi, Jonathan Baugh, and Raymond Laflamme. Heat bath algorithmic cooling with spins: review and prospects. In *Electron Spin Resonance (ESR) Based Quantum Computing*, pages 227–255. Springer, 2016.

[105] P. Oscar Boykin, Tal Mor, Vwani Roychowdhury, Farrokh Vatan, and Rutger Vrijen. Algorithmic cooling and scalable nmr quantum computers. *Proceedings of the National Academy of Sciences*, 99(6):3388–3393, 2002.

[106] Roger B. Sidje. Expokit: a software package for computing matrix exponentials. *ACM Transactions on Mathematical Software (TOMS)*, 24(1):130–156, 1998.

[107] Richard R. Ernst, Geoffrey Bodenhausen, and Alexander Wokaun. Principles of nuclear magnetic resonance in one and two dimensions. 1987.

[108] Varad R. Pande, Gaurav Bhole, Deepak Khurana, and T. S. Mahesh. Strong algorithmic cooling in large star-topology quantum registers. *arXiv preprint arXiv:1702.04992*, 2017.

[109] Navin Khaneja, Roger Brockett, and Steffen J. Glaser. Time optimal control in spin systems. *Physical Review A*, 63(3):032308, 2001.

[110] Haidong Yuan, Robert Zeier, Nikolas Pomplun, Steffen J. Glaser, and Navin Khaneja. Time-optimal polarization transfer from an electron spin to a nuclear spin. *Physical Review A*, 92(5):053414, 2015.

[111] Zdeněk Tošner, Thomas Vosegaard, Cindie Kehlet, Navin Khaneja, Steffen J. Glaser, and Niels Chr. Nielsen. Optimal control in nmr spectroscopy: Numerical implementation in simpson. *Journal of Magnetic Resonance*, 197(2):120–134, 2009.

[112] H. J. Hogben, M. Krzystyniak, G. T. P. Charnock, P. J. Hore, and Ilya Kuprov. Spinach–a software library for simulation of spin dynamics in large spin systems. *Journal of Magnetic Resonance*, 208(2):179–194, 2011.

[113] Steffen J. Glaser, Ugo Boscain, Tommaso Calarco, Christiane P. Koch, Walter Köckenberger, Ronnie Kosloff, Ilya Kuprov, Burkhard Luy, Sophie Schirmer, Thomas Schulte-Herbrüggen, Dominique Sugny, and Frank K. Wilhelm. Training schrodinger's cat: quantum optimal control. *The European Physical Journal D*, 69(12):279, 2015.

[114] Albert W. Overhauser. Paramagnetic relaxation in metals. *Physical Review*, 89(4):689, 1953.

[115] Jun Li, Dawei Lu, Zhihuang Luo, Raymond Laflamme, Xinhua Peng, and Jiangfeng Du. Approximation of reachable sets for coherently controlled open quantum systems: Application to quantum state engineering. *Physical Review A*, 94(1):012312, 2016.

[116] Nayeli A. Rodriguez-Briones, Jun Li, Xinhua Peng, Tal Mor, Yossi Weinstein, and Raymond Laflamme. Heat-bath algorithmic cooling with correlated qubit-environment interactions. *New Journal of Physics*, 19(11):113047, 2017.

[117] Leonard J. Schulman, Tal Mor, and Yossi Weinstein. Physical limits of heat-bath algorithmic cooling. *Physical review letters*, 94(12):120501, 2005.

[118] Daniel A. Lidar, Isaac L. Chuang, and K. Birgitta Whaley. Decoherence-free subspaces for quantum computation. *Physical Review Letters*, 81(12):2594, 1998.

[119] Daniel A. Lidar and K. Birgitta Whaley. Decoherence-free subspaces and subsystems. In *Irreversible quantum dynamics*, pages 83–120. Springer, 2003.

[120] Lorenza Viola, Emanuel Knill, and Seth Lloyd. Dynamical decoupling of open quantum systems. *Physical Review Letters*, 82(12):2417, 1999.

[121] David G. Cory, M. D. Price, W. Maas, Emanuel Knill, Raymond Laflamme, Wojciech H. Zurek, Timothy F. Havel, and S. S. Somaroo. Experimental quantum error correction. *Physical Review Letters*, 81(10):2152, 1998.

[122] John Preskill. Reliable quantum computers. *Proceedings of the Royal Society of London. Series A: Mathematical, Physical and Engineering Sciences*, 454(1969):385–410, 1998.

[123] Tatsuro Yuge, Susumu Sasaki, and Yoshiro Hirayama. Measurement of the noise spectrum using a multiple-pulse sequence. *Physical review letters*, 107(17):170504, 2011.

[124] Gonzalo A. Álvarez and Dieter Suter. Measuring the spectrum of colored noise by dynamical decoupling. *Physical review letters*, 107(23):230501, 2011.

[125] M. J. Biercuk, A. C. Doherty, and H. Uys. Dynamical decoupling sequence construction as a filter-design problem. *Journal of Physics B: Atomic, Molecular and Optical Physics*, 44(15):154002, 2011.

[126] Piotr Szańkowski, Guy Ramon, Jan Krzywda, Damian Kwiatkowski, and Łukasz Cywiński. Environmental noise spectroscopy with qubits subjected to dynamical decoupling. *Journal of Physics: Condensed Matter*, 29(33):333001, 2017.

[127] Piotr Szańkowski, Marek Trippenbach, and Łukasz Cywiński. Spectroscopy of cross correlations of environmental noises with two qubits. *Physical Review A*, 94(1):012109, 2016.

[128] Gerardo A. Paz-Silva, Leigh M. Norris, and Lorenza Viola. Multiqubit spectroscopy of gaussian quantum noise. *Physical Review A*, 95(2):022121, 2017.

[129] Riddhiman Sarkar, Puneet Ahuja, Paul R. Vasos, and Geoffrey Bodenhausen. Long-lived coherences for homogeneous line narrowing in spectroscopy. *Physical review letters*, 104(5):053001, 2010.

[130] Aurélien Bornet, Sami Jannin, J. A. Konter, Patrick Hautle, Ben Van Den Brandt, and Geoffrey Bodenhausen. Ultra high-resolution nmr: sustained induction decays of long-lived coherences. *Journal of the American Chemical Society*, 133(39):15644–15649, 2011.

[131] Jonathan A. Jones, Steven D. Karlen, Joseph Fitzsimons, Arzhang Ardavan, Simon C. Benjamin, G. Andrew D. Briggs, and John J. L. Morton. Magnetic field sensing beyond the standard quantum limit using 10-spin noon states. *Science*, 324(5931):1166–1168, 2009.

[132] Mohamad Niknam, Lea F. Santos, and David G. Cory. Sensitivity of quantum information to environment perturbations measured with the out-of-time-order correlation function. *arXiv preprint arXiv:1808.04375*, 2018.

[133] Martin Gärttner, Philipp Hauke, and Ana Maria Rey. Relating out-of-time-order correlations to entanglement via multiple-quantum coherences. *Physical review letters*, 120(4):040402, 2018.

[134] Leigh M. Norris, Gerardo A. Paz-Silva, and Lorenza Viola. Qubit noise spectroscopy for non-gaussian dephasing environments. *Phys. Rev. Lett.*, 116:150503, Apr 2016.

[135] Youngkyu Sung, Félix Beaudoin, Leigh M. Norris, Fei Yan, David K. Kim, Jack Y. Qiu, Uwe von Lüepke, Jonilyn L. Yoder, Terry P. Orlando, Lorenza Viola, Simon Gustavsson, and William D. Oliver. Non-gaussian noise spectroscopy with a superconducting qubit sensor. *arXiv preprint arXiv:1903.01043*, 2019.

[136] Anatole Abragam. *The principles of nuclear magnetism*. Number 32. Oxford university press, 1961.

[137] M. J. Biercuk, A. C. Doherty, and H. Uys. Dynamical decoupling sequence construction as a filter-design problem. *Journal of Physics B: Atomic, Molecular and Optical Physics*, 44(15):154002, 2011.

[138] A. G. Kofman and G. Kurizki. Universal dynamical control of quantum mechanical decay: Modulation of the coupling to the continuum. *Phys. Rev. Lett.*, 87:270405, Dec 2001.

[139] A. G. Kofman and G. Kurizki. Unified theory of dynamically suppressed qubit decoherence in thermal baths. *Phys. Rev. Lett.*, 93:130406, Sep 2004.

[140] Łukasz Cywiński, Roman M. Lutchyn, Cody P. Nave, and S. Das Sarma. How to enhance dephasing time in superconducting qubits. *Phys. Rev. B*, 77:174509, May 2008.

[141] H. Y. Carr and E. M. Purcell. Effects of diffusion on free precession in nuclear magnetic resonance experiments. *Phys. Rev.*, 94:630–638, May 1954.

[142] Saul Meiboom and David Gill. Modified spin-echo method for measuring nuclear relaxation times. *Review of scientific instruments*, 29(8):688–691, 1958.

[143] Swathi S. Hegde and T. S. Mahesh. Engineered decoherence: Characterization and suppression. *Physical Review A*, 89(6):062317, 2014.

[144] Mustafa Ahmed Ali Ahmed, Gonzalo A. Álvarez, and Dieter Suter. Robustness of dynamical decoupling sequences. *Physical Review A*, 87(4):042309, 2013.

[145] Giuseppe Pileio and Malcolm H. Levitt. Theory of long-lived nuclear spin states in solution nuclear magnetic resonance. ii. singlet spin locking. *The Journal of chemical physics*, 130(21):214501, 2009.

[146] Giuseppe Pileio and Malcolm H. Levitt. Theory of long-lived nuclear spin states in solution nuclear magnetic resonance. ii. singlet spin locking. *The Journal of chemical physics*, 130(21):214501, 2009.

[147] A.G. Redfield. The theory of relaxation processes. *Advances in Magnetic and Optical Resonance*, 1:1–32, 1965.

[148] J. Tang and Alexander Pines. Multiple quantum nmr and relaxation of an oriented ch3 group. *The Journal of Chemical Physics*, 72(5):3290–3297, 1980.

[149] Hans Georg Krojanski and Dieter Suter. Scaling of decoherence in wide nmr quantum registers. *Physical review letters*, 93(9):090501, 2004.

[150] Götz S. Uhrig. Keeping a quantum bit alive by optimized π-pulse sequences. *Phys. Rev. Lett.*, 98:100504, Mar 2007.

[151] Dave Bacon, Julia Kempe, Daniel A. Lidar, and KB Whaley. Universal fault-tolerant quantum computation on decoherence-free subspaces. *Physical Review Letters*, 85(8):1758, 2000.

[152] Bassano Vacchini, Andrea Smirne, Elsi-Mari Laine, Jyrki Piilo, and Heinz-Peter Breuer. Markovianity and non-markovianity in quantum and classical systems. *New Journal of Physics*, 13(9):093004, 2011.

[153] Inés de Vega and Daniel Alonso. Dynamics of non-markovian open quantum systems. *Reviews of Modern Physics*, 89(1):015001, 2017.

[154] Li Li, Michael J. W. Hall, and Howard M. Wiseman. Concepts of quantum non-markovianity: a hierarchy. *Physics Reports*, 2018.

[155] Angel Rivas, Susana F. Huelga, and Martin B. Plenio. Quantum non-markovianity: characterization, quantification and detection. *Reports on Progress in Physics*, 77(9):094001, 2014.

[156] Susana F. Huelga, Ángel Rivas, and Martin B. Plenio. Non-markovianity-assisted steady state entanglement. *Physical review letters*, 108(16):160402, 2012.

[157] Ruggero Vasile, Stefano Olivares, Matteo G. A. Paris, and Sabrina Maniscalco. Continuous-variable quantum key distribution in non-markovian channels. *Physical Review A*, 83(4):042321, 2011.

[158] B. Bylicka, D. Chruściński, and Sabrina Maniscalco. Non-markovianity and reservoir memory of quantum channels: a quantum information theory perspective. *Scientific reports*, 4:5720, 2014.

[159] Alex W. Chin, Susana F. Huelga, and Martin B. Plenio. Quantum metrology in non-markovian environments. *Physical review letters*, 109(23):233601, 2012.

[160] Yang Dong, Yu Zheng, Shen Li, Cong-Cong Li, Xiang-Dong Chen, Guang-Can Guo, and Fang-Wen Sun. Non-markovianity-assisted high-fidelity deutsch–jozsa algorithm in diamond. *npj Quantum Information*, 4(1):3, 2018.

[161] Elsi-Mari Laine, Heinz-Peter Breuer, and Jyrki Piilo. Nonlocal memory effects allow perfect teleportation with mixed states. *Scientific reports*, 4:4620, 2014.

[162] Ángel Rivas, Susana F. Huelga, and Martin B. Plenio. Entanglement and non-markovianity of quantum evolutions. *Physical Review Letters*, 105(5):050403, 2010.

[163] Dariusz Chruściński and Sabrina Maniscalco. Degree of non-markovianity of quantum evolution. *Physical review letters*, 112(12):120404, 2014.

[164] Gianpaolo Torre, Wojciech Roga, and Fabrizio Illuminati. Non-markovianity of gaussian channels. *Physical review letters*, 115(7):070401, 2015.

[165] Shunlong Luo, Shuangshuang Fu, and Hongting Song. Quantifying non-markovianity via correlations. *Physical Review A*, 86(4):044101, 2012.

[166] Xiao-Ming Lu, Xiaoguang Wang, and C. P. Sun. Quantum fisher information flow and non-markovian processes of open systems. *Physical Review A*, 82(4):042103, 2010.

[167] Salvatore Lorenzo, Francesco Plastina, and Mauro Paternostro. Geometrical characterization of non-markovianity. *Physical Review A*, 88(2):020102, 2013.

[168] Ruggero Vasile, Sabrina Maniscalco, Matteo G. A. Paris, Heinz-Peter Breuer, and Jyrki Piilo. Quantifying non-markovianity of continuous-variable gaussian dynamical maps. *Physical Review A*, 84(5):052118, 2011.

[169] John H. Reina, Luis Quiroga, and Neil F. Johnson. Decoherence of quantum registers. *Physical Review A*, 65(3):032326, 2002.

[170] Carole Addis, Bogna Bylicka, Dariusz Chruściński, and Sabrina Maniscalco. Comparative study of non-markovianity measures in exactly solvable one-and two-qubit models. *Physical Review A*, 90(5):052103, 2014.

[171] Giacomo Guarnieri, Andrea Smirne, and Bassano Vacchini. Quantum regression theorem and non-markovianity of quantum dynamics. *Physical Review A*, 90(2):022110, 2014.

[172] Hao-Sheng Zeng, Ning Tang, Yan-Ping Zheng, and Guo-You Wang. Equivalence of the measures of non-markovianity for open two-level systems. *Physical Review A*, 84(3):032118, 2011.

[173] Victor Mukherjee, Vittorio Giovannetti, Rosario Fazio, Susana F. Huelga, Tommaso Calarco, and Simone Montangero. Efficiency of quantum controlled non-markovian thermalization. *New Journal of Physics*, 17(6):063031, 2015.

[174] Carole Addis, Elsi-Mari Laine, Clemens Gneiting, and Sabrina Maniscalco. Problem of coherent control in non-markovian open quantum systems. *Physical Review A*, 94(5):052117, 2016.

[175] Etienne Mangaud, Raijumon Puthumpally-Joseph, Dominique Sugny, Christoph Meier, Osman Atabek, and Michèle Desouter-Lecomte. Non-markovianity in the optimal control of an open quantum system described by hierarchical equations of motion. *New Journal of Physics*, 20(4):043050, 2018.

[176] Jung-Shen Tai, Kuan-Ting Lin, and Hsi-Sheng Goan. Optimal control of quantum gates in an exactly solvable non-markovian open quantum bit system. *Physical Review A*, 89(6):062310, 2014.

[177] Carole Addis, Francesco Ciccarello, Michele Cascio, G. Massimo Palma, and Sabrina Maniscalco. Dynamical decoupling efficiency versus quantum non-markovianity. *New Journal of Physics*, 17(12):123004, 2015.

[178] Nicolás Mirkin, Pablo Poggi, and Diego Wisniacki. Entangling protocols due to non-markovian dynamics. *arXiv preprint arXiv:1711.10551v2*, 2018.

[179] Daniel M. Reich, Nadav Katz, and Christiane P. Koch. Exploiting non-markovianity for quantum control. *Scientific reports*, 5:12430, 2015.

[180] Lorenza Viola and Seth Lloyd. Dynamical suppression of decoherence in two-state quantum systems. *Physical Review A*, 58(4):2733, 1998.

[181] Kaveh Khodjasteh and Daniel A. Lidar. Fault-tolerant quantum dynamical decoupling. *Physical review letters*, 95(18):180501, 2005.

[182] Stefano Pasini and Götz S. Uhrig. Optimized dynamical decoupling for power-law noise spectra. *Physical Review A*, 81(1):012309, 2010.

[183] Götz S. Uhrig. Keeping a quantum bit alive by optimized π-pulse sequences. *Physical Review Letters*, 98(10):100504, 2007.

[184] Götz S. Uhrig and Daniel A. Lidar. Rigorous bounds for optimal dynamical decoupling. *Physical Review A*, 82(1):012301, 2010.

[185] Wen Yang and Ren-Bao Liu. Universality of uhrig dynamical decoupling for suppressing qubit pure dephasing and relaxation. *Physical review letters*, 101(18):180403, 2008.

[186] Wen Yang, Zhen-Yu Wang, and Ren-Bao Liu. Preserving qubit coherence by dynamical decoupling. *Frontiers of Physics in China*, 6(1):2–14, 2011.

[187] Łukasz Cywiński, Roman M. Lutchyn, Cody P. Nave, and S. Das Sarma. How to enhance dephasing time in superconducting qubits. *Physical Review B*, 77(17):174509, 2008.

[188] M. J. Biercuk, H. Uys, Aaron P. VanDevender, Nobuyasu Shiga, Wayne M. Itano, and John J. Bollinger. Optimized dynamical decoupling in a model quantum memory. *Nature*, 458(7241):996, 2009.

[189] Jiangfeng Du, Xing Rong, Nan Zhao, Ya Wang, Jiahui Yang, and R. B. Liu. Preserving electron spin coherence in solids by optimal dynamical decoupling. *Nature*, 461(7268):1265, 2009.

[190] Gonzalo A. Álvarez, Ashok Ajoy, Xinhua Peng, and Dieter Suter. Performance comparison of dynamical decoupling sequences for a qubit in a rapidly fluctuating spin bath. *Physical Review A*, 82(4):042306, 2010.

[191] Ashok Ajoy, Gonzalo A. Álvarez, and Dieter Suter. Optimal pulse spacing for dynamical decoupling in the presence of a purely dephasing spin bath. *Physical Review A*, 83(3):032303, 2011.

[192] Alexandre M. Souza, Gonzalo A. Álvarez, and Dieter Suter. Robust dynamical decoupling for quantum computing and quantum memory. *Physical review letters*, 106(24):240501, 2011.

[193] Bi-Heng Liu, Li Li, Yun-Feng Huang, Chuan-Feng Li, Guang-Can Guo, Elsi-Mari Laine, Heinz-Peter Breuer, and Jyrki Piilo. Experimental control of the transition from markovian to non-markovian dynamics of open quantum systems. *Nature Physics*, 7(12):931, 2011.

[194] A. Soare, H. Ball, D. Hayes, X. Zhen, M. C. Jarratt, J. Sastrawan, H. Uys, and M. J. Biercuk. Experimental bath engineering for quantitative studies of quantum control. *Physical Review A*, 89(4):042329, 2014.

[195] H. Ball, T. M. Stace, Steven T. Flammia, and M. J. Biercuk. Effect of noise correlations on randomized benchmarking. *Physical Review A*, 93(2):022303, 2016.

[196] A. Soare, H. Ball, D. Hayes, J. Sastrawan, M. C. Jarratt, J. J. McLoughlin, X. Zhen, T. J. Green, and M. J. Biercuk. Experimental noise filtering by quantum control. *Nature Physics*, 10(11):825, 2014.

[197] C. L. Edmunds, C. Hempel, R. Harris, H. Ball, V. Frey, T. M. Stace, and M. J. Biercuk. Measuring and suppressing error correlations in quantum circuits. *arXiv preprint arXiv:1712.04954*, 2017.

[198] S. Mavadia, C. L. Edmunds, C. Hempel, H. Ball, F. Roy, T. M. Stace, and M. J. Biercuk. Experimental quantum verification in the presence of temporally correlated noise. *npj Quantum Information*, 4(1):7, 2018.

[199] Xing-Long Zhen, Fei-Hao Zhang, Guanru Feng, Hang Li, and Gui-Lu Long. Optimal experimental dynamical decoupling of both longitudinal and transverse relaxations. *Physical Review A*, 93(2):022304, 2016.

[200] H. Y. Carr and E. M. Purcell. Effects of diffusion on free precession in nuclear magnetic resonance experiments. *Physical review*, 94(3):630, 1954.

[201] Steffen Wißmann, Antti Karlsson, Elsi-Mari Laine, Jyrki Piilo, and Heinz-Peter Breuer. Optimal state pairs for non-markovian quantum dynamics. *Physical Review A*, 86(6):062108, 2012.

[202] Alexandre M. Souza, Gonzalo A. Álvarez, and Dieter Suter. Robust dynamical decoupling. *Phil. Trans. R. Soc. A*, 370(1976):4748–4769, 2012.

[203] Sai Vinjanampathy and Janet Anders. Quantum thermodynamics. *Contemporary Physics*, 57(4):545–579, 2016.

[204] Christopher Jarzynski. Stochastic and macroscopic thermodynamics of strongly coupled systems. *Physical Review X*, 7(1):011008, 2017.

[205] Philipp Strasberg, Gernot Schaller, Neill Lambert, and Tobias Brandes. Nonequilibrium thermodynamics in the strong coupling and non-markovian regime based on a reaction coordinate mapping. *New Journal of Physics*, 18(7):073007, 2016.

[206] Gil Katz and Ronnie Kosloff. Quantum thermodynamics in strong coupling: heat transport and refrigeration. *Entropy*, 18(5):186, 2016.

[207] Hava Meira Friedman, Bijay Kumar Agarwalla, and Dvira Segal. Quantum thermodynamics from weak to strong system-bath coupling. *New Journal of Physics*, 20:083026, 2018.

[208] Götz S. Uhrig. Exact results on dynamical decoupling by π pulses in quantum information processes. *New Journal of Physics*, 10(8):083024, 2008.

[209] Goren Gordon, Gershon Kurizki, and Daniel A. Lidar. Optimal dynamical decoherence control of a qubit. *Physical review letters*, 101(1):010403, 2008.

[210] H. Uys, M. J. Biercuk, and J. J. Bollinger. Optimized noise filtration through dynamical decoupling. *Physical Review Letters*, 103(4):040501, 2009.

[211] Jens Clausen, Guy Bensky, and Gershon Kurizki. Bath-optimized minimal-energy protection of quantum operations from decoherence. *Physical review letters*, 104(4):040401, 2010.

[212] Stephen H. Shenker and Douglas Stanford. Black holes and the butterfly effect. *Journal of High Energy Physics*, 2014(3):67, 2014.

[213] Juan Maldacena, Stephen H. Shenker, and Douglas Stanford. A bound on chaos. *Journal of High Energy Physics*, 2016(8):106, 2016.

[214] Pavan Hosur, Xiao-Liang Qi, Daniel A. Roberts, and Beni Yoshida. Chaos in quantum channels. *Journal of High Energy Physics*, 2016(2):4, 2016.

[215] Ken Xuan Wei, Chandrasekhar Ramanathan, and Paola Cappellaro. Exploring localization in nuclear spin chains. *Physical review letters*, 120(7):070501, 2018.

[216] Yichen Huang, Yong-Liang Zhang, and Xie Chen. Out-of-time-ordered correlators in many-body localized systems. *Annalen der Physik*, 529(7):1600318, 2017.

[217] Ruihua Fan, Pengfei Zhang, Huitao Shen, and Hui Zhai. Out-of-time-order correlation for many-body localization. *Science bulletin*, 62(10):707–711, 2017.

[218] Yu Chen. Universal logarithmic scrambling in many body localization. *arXiv preprint arXiv:1608.02765*, 2016.

[219] Markus Heyl, Frank Pollmann, and Balázs Dóra. Detecting equilibrium and dynamical quantum phase transitions in ising chains via out-of-time-ordered correlators. *Physical review letters*, 121(1):016801, 2018.

[220] Sumilan Banerjee and Ehud Altman. Solvable model for a dynamical quantum phase transition from fast to slow scrambling. *Physical Review B*, 95(13):134302, 2017.

[221] Ken Xuan Wei, Pai Peng, Oles Shtanko, Iman Marvian, Seth Lloyd, Chandrasekhar Ramanathan, and Paola Cappellaro. Emergent prethermalization signatures in out-of-time ordered correlations. *arXiv preprint arXiv:1812.04776*, 2018.

[222] AI Larkin and Yu N Ovchinnikov. Quasiclassical method in the theory of superconductivity. *Sov Phys JETP*, 28(6):1200–1205, 1969.

[223] Daniel A. Roberts, Douglas Stanford, and Leonard Susskind. Localized shocks. *Journal of High Energy Physics*, 2015(3):51, 2015.

[224] Brian Swingle, Gregory Bentsen, Monika Schleier-Smith, and Patrick Hayden. Measuring the scrambling of quantum information. *Physical Review A*, 94(4):040302, 2016.

[225] Norman Y. Yao, Fabian Grusdt, Brian Swingle, Mikhail D. Lukin, Dan M. Stamper-Kurn, Joel E. Moore, and Eugene A. Demler. Interferometric approach to probing fast scrambling. *arXiv preprint arXiv:1607.01801*, 2016.

[226] Guanyu Zhu, Mohammad Hafezi, and Tarun Grover. Measurement of many-body chaos using a quantum clock. *Physical Review A*, 94(6):062329, 2016.

[227] Nicole Yunger Halpern, Brian Swingle, and Justin Dressel. Quasiprobability behind the out-of-time-ordered correlator. *Physical Review A*, 97(4):042105, 2018.

[228] Jun Li, Ruihua Fan, Hengyan Wang, Bingtian Ye, Bei Zeng, Hui Zhai, Xinhua Peng, and Jiangfeng Du. Measuring out-of-time-order correlators on a nuclear magnetic resonance quantum simulator. *Physical Review X*, 7(3):031011, 2017.

[229] Kevin A. Landsman, Caroline Figgatt, Thomas Schuster, Norbert M. Linke, Beni Yoshida, Norm Y. Yao, and Christopher Monroe. Verified quantum information scrambling. *Nature*, 567(7746):61, 2019.

[230] Martin Gärttner, Justin G. Bohnet, Arghavan Safavi-Naini, Michael L. Wall, John J. Bollinger, and Ana Maria Rey. Measuring out-of-time-order correlations and multiple quantum spectra in a trapped-ion quantum magnet. *Nature Physics*, 13(8):781, 2017.

[231] Brian Swingle and Nicole Yunger Halpern. Resilience of scrambling measurements. *Physical Review A*, 97(6):062113, 2018.

[232] Beni Yoshida and Norman Y. Yao. Disentangling scrambling and decoherence via quantum teleportation. *Physical Review X*, 9(1):011006, 2019.

[233] José Raúl González Alonso, Nicole Yunger Halpern, and Justin Dressel. Out-of-time-ordered-correlator quasiprobabilities robustly witness scrambling. *Physical review letters*, 122(4):040404, 2019.

[234] Deepak Khurana, Govind Unnikrishnan, and T. S. Mahesh. Spectral investigation of the noise influencing multiqubit states. *Physical Review A*, 94(6):062334, 2016.

[235] Abhishek Shukla, Manvendra Sharma, and T. S. Mahesh. Noon states in star-topology spin-systems: Applications in diffusion studies and rf inhomogeneity mapping. *Chemical Physics Letters*, 592:227–231, 2014.

[236] R. Hanson, V. V. Dobrovitski, A. E. Feiguin, O. Gywat, and D. D. Awschalom. Coherent dynamics of a single spin interacting with an adjustable spin bath. *Science*, 320(5874):352–355, 2008.

[237] John Cavanagh, Wayne J. Fairbrother, Arthur G. Palmer III, and Nicholas J. Skelton. *Protein NMR spectroscopy: principles and practice*. Elsevier, 1995.

[238] Hemant Katiyar, Soumya S. Roy, T. S. Mahesh, and Apoorva Patel. Evolution of quantum discord and its stability in two-qubit nmr systems. *Physical Review A*, 86(1):012309, 2012.

[239] V. R. Krithika, V . S. Anjusha, Udaysinh T Bhosale, and T. S. Mahesh. Nmr studies of quantum chaos in a two-qubit kicked top. *Physical Review E*, 99(3):032219, 2019.